

Electronically Induced Diffusion of Oxygen on Pt(111)



Dissertation

zur

Erlangung des Doktorgrades
der Naturwissenschaften
(Dr. rer. nat.)

dem

Fachbereich Physik
der Philipps-Universität Marburg

vorgelegt von

Krisztina Stépan

aus

Miskolc, Ungarn

Marburg/Lahn, 2006

Vom Fachbereich Physik der Philipps-Universität Marburg als Dissertation am 13.03.2006 angenommen.

Erstgutachter: Prof. Dr. Ulrich Höfer
Zweitgutachter: Prof. Dr. Peter Thomas
Tag der mündlichen Prüfung: 20.03.2006

”A work as this is never finished,
one must simply declare it finished when one has,
within limits of time and circumstances,
done what is possible.”
(Goethe, 1787)

Contents

Zusammenfassung	5
1. Introduction	7
2. Fundamentals	11
2.1 Electronically Induced Surface Processes	11
2.2 Detection of Diffusion	16
2.2.1 Optical Second-Harmonic Generation (SHG)	18
2.3 Oxygen on Pt(111) Surfaces	26
2.3.1 Pt(111) Surface	26
2.3.2 Adsorption of Oxygen on Stepped Pt(111)	29
3. Experimental Setup	33
3.1 Ultra-High Vacuum System	33
3.2 Platinum Surface Preparation	36
3.3 Optical Setup	37
4. Characterization of O₂ Adsorption	41
4.1 Temperature Programmed Desorption	41
4.2 Step sensitivity of the SHG	43
4.3 Polarization Dependence	43
4.4 Step Selectivity of the SH Detection	47
4.4.1 LEED Patterns of the Dosed Platinum Surfaces	48
4.5 Frequency Domain SHG Interferometry	49
5. Time-Resolved Detection of Surface Diffusion	55
5.1 Observation of Laser-Induced Diffusion	55
5.2 Thermally Induced Diffusion	59
5.3 Dependence of the Diffusion-Rate on the Repetition Rate of the Pump Laser	61
5.4 Kinetics of Step-Terrace Diffusion	62

5.5	Fluence Dependence	66
5.6	Two-Pulse Correlation Measurement	68
6.	Modeling of the Diffusion	71
6.1	Two-Temperature Model	72
6.2	Electronic Friction Models	74
6.3	Model calculation with Constant Friction	78
6.4	Model calculation with Temperature Dependent Friction	81
7.	Discussion and Perspectives	85
7.1	Position of the Unoccupied Adsorbate Level	85
7.2	Indirect Excitation	86
7.3	Perspectives	90
	Summary	93
A.	Details of the Two-Temperature Model	95
A.1	Thermalization of Hot Electrons	95
A.2	Electron-Phonon Scattering	96
A.3	Optical Excitation and Penetration Depth	97
	Bibliography	101
	List of Publications	109
	Curriculum Vitae	111
	Acknowledgments	113

Zusammenfassung

Die laserinduzierte Diffusion von atomarem Sauerstoff auf einer gestuften Pt(111) Oberfläche wurde untersucht, wobei ultrakurze Laserimpulse mit Photonenenergien im nahen Infrarot eingesetzt wurden. Die Arbeit stellt die erste zeitaufgelöste Untersuchung eines Diffusionsprozesses an einer Einkristalloberfläche dar. Sie demonstriert darüberhinaus die Möglichkeit, die Diffusion eines stark chemisorbierten Adsorbats auf einer Metalloberfläche bei tiefen Temperaturen durch elektronische Anregung auszulösen.

Für das Experiment wurde die Selektivität der dissoziativen Adsorption von molekularem Sauerstoff für die Stufen der Pt(111) Oberfläche ausgenutzt, um zunächst eine Nichtgleichgewichtsverteilung des Adsorbates zu erzeugen. Die Bedeckung der Stufenkanten mit chemisorbiertem Sauerstoff wurde während der Adsorption und der laserinduzierten Diffusion in-situ mit Hilfe der optischen Frequenzverdopplung (SHG) an Oberflächen verfolgt. Dabei wurde ausgenutzt, dass die Erzeugung der zweiten Harmonischen in Dipolnäherung einen Symmetriebruch erfordert, wie er durch die regelmäßigen Stufen entsteht. Die hohe Empfindlichkeit dieser Detektionsmethode machte es möglich, Hüpfraten für die Bewegung von den Stufenkanten auf die anfangs leeren Terrassenplätze bis herunter zu 10^{-7} pro Laserimpuls zu messen. Zur Durchführung dieser optischen Experimente sowie zur Präparation und Charakterisierung der Platinoberfläche wurde eine Ultrahochvakuumapparatur aufgebaut.

Um Aufschluss über die Dynamik des Energietransfers von der optischen Anregung in die frustrierte Translationen des Adsorbats zu gewinnen, wurde die Diffusionsrate als Funktion der eingestrahnten Laserleistung und, in einem Korrelationsexperiment, als Funktion der Verzögerung zwischen zwei Pump-Impulsen gemessen. Die Experimente zeigen eine sehr stark nichtlineare Abhängigkeit der Diffusionsrate von der Energiedichte der Laserimpulse ($\propto F^{15}$) sowie eine schnelle elektronische Kopplung zwischen der anfänglichen Anregung und der Adsorbatbewegung mit einer Zeitkonstanten von 1.5 ps. Beide Ergebnisse legen es nahe, dass der prinzipielle Anregungsmechanismus der gleiche ist wie im Fall der bereits intensiv untersuchten, laserinduzierten Desorption: Die kurzen, intensiven Laserimpulse erzeugen eine heiße Elektronenverteilung an der Oberfläche, ohne dass das Substratgitter zunächst nen-

nenswert aufgeheizt wird. Die heißen Elektronen regen auf der Zeitskala von 1.5 ps mehrfach die Adsorbat-Substratbindung und damit eine Adsorbatbewegung an.

Die extrem nichtlineare Abhängigkeit der Hüpftrate von der Energiedichte der Laserimpulse deutet aber darauf hin, dass der Energietransfermechanismus hier komplizierter ist, als im Fall der Desorption. Bei der quantitativen Beschreibung im Rahmen eines elektronischen Reibungsmodells für die nichtadiabatische Kopplung der Adsorbatbewegung an das Elektronensystem des Substrats wird die Einführung eines temperaturabhängigen elektronischen Reibungskoeffizienten notwendig. Als Erklärung wird vorgeschlagen, dass die frustrierten Translationen, die schließlich zur Diffusion führen, hauptsächlich indirekt angeregt werden. Durch die elektronische Reibung werden zunächst primär O-Pt-Streckschwingungen angeregt und diese koppeln dann anharmonisch an die frustrierten O-Pt-Translationen. In diesem Modell entsteht die scheinbare Abhängigkeit des Reibungskoeffizienten von der Elektronentemperatur bzw. der Anregungsdichte durch die Zunahme der anharmonischen Kopplung mit der Besetzung höherer Schwingungsniveaus.

Chapter 1

Introduction

Diffusion of adsorbates is an important elementary step in many surface processes such as epitaxial growth or catalytic reactions. Usually, surface diffusion is a thermally activated process that is initiated by heating the substrate. At sufficiently high temperatures the thermal population of frustrated translations enables a small fraction of the adsorbates to overcome the barrier E_{diff} for lateral motion and to hop to the next adsorption site. This process requires a minimum temperature of the order of $kT \approx E_{\text{diff}}/20$, and in general it strongly favors the diffusion pathway with the lowest barrier height over any other one. In some cases it would be desirable to have more control over migration pathways or to enable diffusion of a particular species at a lower temperature where competing surface reactions have not yet set in. For these and other purposes one would like to induce diffusion by electronic instead of thermal excitation of the adsorbate-substrate system.

In the past forty years electronically induced adsorbate reactions have become a subject of great interest and importance in the surface science community. However, to a large extent the research has focused on desorption phenomena. This statement holds for classical desorption processes induced by electronic transitions (DIET) which can be described within the framework of the Menzel-Gomer-Redhead (MGR) model [1, 2] as well as for the regime of desorption induced by multiple electronic transitions (DIMET) which has been discovered by exciting metal surfaces with intense femtosecond laser pulses [3, 4, 5, 6, 7, 8, 9, 10, 11, 12, 13, 14, 15, 16, 17]. The high density of electron hole pairs created in the metal causes repetitive electronic transitions between the ground and excited states of the adsorbate-metal system on the timescale of nuclear motion. This leads to reaction yields that are typically orders of magnitude higher than in conventional photochemical reactions at metal surfaces [18, 19, 20]. In many cases a basic understanding of the complicated electronic excitation kinetics and its coupling to nuclear motion could be achieved by introducing an electronic friction between adsorbate modes and electronic degrees of freedom [21, 22, 23, 24].

In the case of metal surfaces, lateral variations of the adsorbate-substrate bonds

are generally much weaker than total bond strengths. For this reason, barriers for thermally activated diffusion processes are generally smaller than those for desorption. Similarly one can expect that the amount of electronic excitation required to initiate diffusion should be less than the amount required for desorption. In fact, the concept of electronic friction to describe the electronic coupling of an adsorbate with a metal surface was first discussed in the context of diffusion [25, 26]. Experimentally, however, the observation of lateral motion following electronic excitation is more difficult to detect compared to desorbing atoms or molecules, which can be accomplished efficiently in the gas phase. For this reason, systematic studies of electronically induced diffusion processes are scarce and the coupling of electronic excitations of adsorbates to frustrated translation is not well understood.

Early reports of electron-stimulated diffusion or migration of adsorbates were based on the changes of low-energy electron diffraction (LEED) patterns and changes of angular distributions of desorbing species as a function of electron irradiation [27, 28]. Direct spectroscopic evidence could be obtained for CO/Pt(335) where the migration of CO molecules from terrace to step sites induced by an electron gun was detected with the help of infrared spectroscopy [29]. Recently, scanning tunneling microscopy (STM) and the possibility to manipulate adsorbates on surfaces has led to a growing interest in electron-stimulated rearrangement processes of adsorbates. Several groups have shown that inelastic tunneling of electrons from an STM tip can lead to rotational and diffusive motion of adsorbed molecules [30, 31, 32, 33]. Also the first study of laser-induced diffusion used the STM to detect adsorbate motion. Bartels and co-workers [34] were able to show for the system CO/Cu(110) that electronic excitation of the substrate induced by absorption of short laser pulses gives rise to diffusion of CO parallel and perpendicular to the close-packed rows with similar efficiency as CO desorption [34].

Whereas STM methods allow the observation of microscopic diffusion pathways, the determination of quantitative diffusion rates as a function of the parameters of an external excitation source such as a laser can be quite time consuming. For this reason we make use of a different experimental approach to detect laser-induced diffusion. The method is similar to the one used previously to study thermally activated diffusion of hydrogen on a vicinal Si(001) surface [35]. It has a similar sensitivity as STM but averages over many microscopic events. The principle of this method is sketched in Fig. 1.1.

First, a non-equilibrium distribution of adsorbate atoms is produced by decorating step edges of a vicinal surface selectively by dissociative adsorption. Then, diffusion from the step edges onto the terraces is induced by ultrashort laser pulses. The

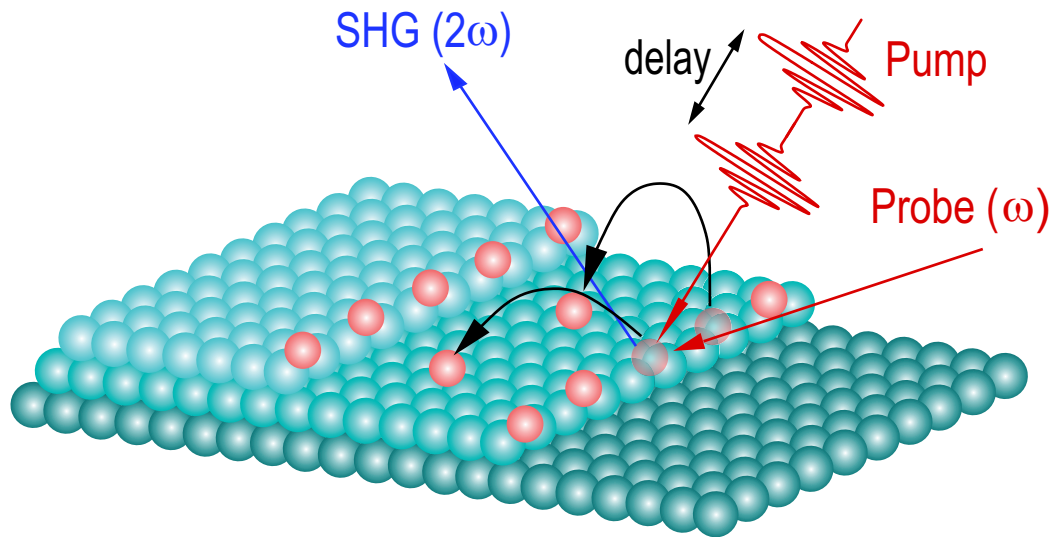


Fig. 1.1: Scheme of the experiment. Step sites are decorated selectively by dissociative adsorption. Intensive ultrashort laser pulses induce diffusion onto the terraces, which is monitored by second-harmonic generation of a probe beam.

depopulation of the step sites is monitored by optical second-harmonic generation (SHG). SHG is an optical probe of electronic, structural, and magnetic properties of surfaces and interfaces that owes part of its sensitivity to the occurrence of a symmetry break at surfaces [36,37,38,39]. Since the presence of regular steps on a vicinal surface breaks the symmetry parallel to the surface, step sites can be a very efficient source of SHG [40,41]. The capability of SHG to monitor step coverage *in situ* and in real time [35,41] makes it possible to determine diffusion rates as a function of laser fluence and delay between two pump pulses [42].

Our choice of atomic oxygen on a vicinal Pt(111) surface for the study of laser-induced diffusion is motivated by its model character for diffusion of a strongly chemisorbed atomic adsorbate and for experimental reasons. Due to the importance of Pt as a catalyst in oxidation reactions the dissociative adsorption of O_2 on Pt has been extensively studied, which gave us a good starting point for our investigations.

The composition of this thesis is the following: after the introduction, the physical fundamentals of the investigated systems and methods are presented in Chap. 2. As mentioned above our diffusion experiments were motivated by experiments that studied desorption induced by electronic transitions. Therefore, we will give an overview of these processes as a starting point. SHG is a purely optical nonlinear method which can provide a genuine surface sensitive signal, because the inversion symmetry of centrosymmetric media like Pt is broken at the surface. After discussing SHG as a surface and symmetry sensitive method, we will present the known facts about the

adsorption of oxygen on flat and stepped Pt(111) surfaces.

The description of the experimental setup used for our investigations is the topic of Chap. 3. It starts with the presentation of the ultra-high vacuum (UHV) system which was built for this study by myself. Then, the preparation procedure of the Pt surface and finally, the laser and optical setup is described.

Chapt. 4 is devoted to the preparative characterization of the dissociative adsorption of O₂ on the vicinal Pt surface by temperature programmed desorption (TPD), low-energy electron diffraction (LEED) and the above mentioned SHG technique.

The laser-induced diffusion experiments are presented in Chapt. 5. First, we show how diffusion from step sites onto initially empty terraces can be detected by SHG (Sect. 5.1). Thermally induced diffusion experiments have been performed to estimate the corresponding diffusion barrier (Sect. 5.2). Laser-induced diffusion experiments at different repetition rates demonstrate that the diffusion is not driven by an average heating of the sample by the laser pulses (Sect. 5.3). Hopping-rates for step-terrace diffusion are extracted from the experimental data by applying a one-dimensional rate-equation model which is described in Sect. 5.4. The hopping-rate is observed to increase in an extremely nonlinear fashion with laser fluence (Sect. 5.5), which made it possible to apply a two-pulse correlation technique for the investigation of energy transfer dynamics from the optical excitation to lateral motion (Sect. 5.6).

Chapt. 6 describes the modeling of the experimental data with different variants of the electronic friction model for an approximate description of the coupling between adsorbate and substrate degrees of freedom. It will be shown that, in contrast to laser-induced desorption experiments, a consistent description of the experimental data can be only achieved by introducing an electronic friction coefficient that increases with the electron temperature of the substrate. This result is not expected from the electronic structure of O/Pt.

In the final Chapt. 7 these results are interpreted in terms of an indirect excitation mechanism. It is proposed that the hot substrate electrons predominantly excite the O-Pt stretch vibration which then couples anharmonically to the frustrated translation mode required to overcome the barrier for lateral motion. This model introduces a coupling that depends on excitation density and would therefore explain the observed effective dependence of the electronic friction on electron temperature.

Chapter 2

Fundamentals

This chapter gives an overview about the fundamentals of this work. First, electronically induced surface processes are discussed for the example of desorption within the framework of the DIET model and its extension DIMET which we would like to adapt to the process of diffusion. Then, we describe how optical second-harmonic generation (SHG) at surfaces can be used to detect diffusion of adsorbates on vicinal surfaces. Finally, we discuss how atomic oxygen adsorbs at steps of different geometries on vicinal Pt(111) surfaces.

2.1 Electronically Induced Surface Processes

In contrast to the gas phase, the dynamics of surface processes, such as forming chemical bonds or breaking them, are much less known. The presence of a substrate opens new channels for energy and charge transfer between the adsorbate and the surface. Therefore, the reaction mechanism for an adsorbate-substrate system is much more complex compared to the gas phase. For a microscopic understanding of surface reactions we have to comprehend the dynamics of the energy transfer between different degrees of freedom of the adsorbate motion (rotation, vibration and translation) and the electronic and phononic system of the substrate.

The so-called adiabatic approximation is often used to discuss the kinetics of chemical reactions. It assumes that the different reaction partners are always in equilibrium, which makes the macroscopic temperature T of the system the central parameter that determines the reaction. One key prerequisite for its validity is the Born-Oppenheimer approximation, postulating that the atomic cores are static on the timescales of electronic movement and therewith leading to a decoupling of electron and nuclear motion. Only on this basis it becomes possible to describe chemical reactions in such a manner that it depends only on the core coordinates and that it takes place on the potential energy surface of the system in its electronic ground state.

The adiabatic approximation is used to describe surface reactions as well. The

most basic view of such adsorbate-substrate bindings, imagining for example transition metal substrates, is quite close to the picture for a two-atomic molecule. In analogy to simple molecular bonding, this bonding is characterized with a bonding ("highest occupied molecular orbit", HOMO) and an anti-bonding ("lowest unoccupied molecular orbit", LUMO) state. The bonding strength depends on the position of the Fermi level which also determines the occupancy of bonding and anti-bonding state.

In this case the adsorbate motion can be also excited by electronic transitions due to the coupling of electronic and nuclear degrees of freedom. Since these processes are usually neglected in the common adiabatic or Born-Oppenheimer approximation, the initiation of adsorbate motion by electron-hole pair creation or vice versa is called a non-adiabatic or diabatic process.

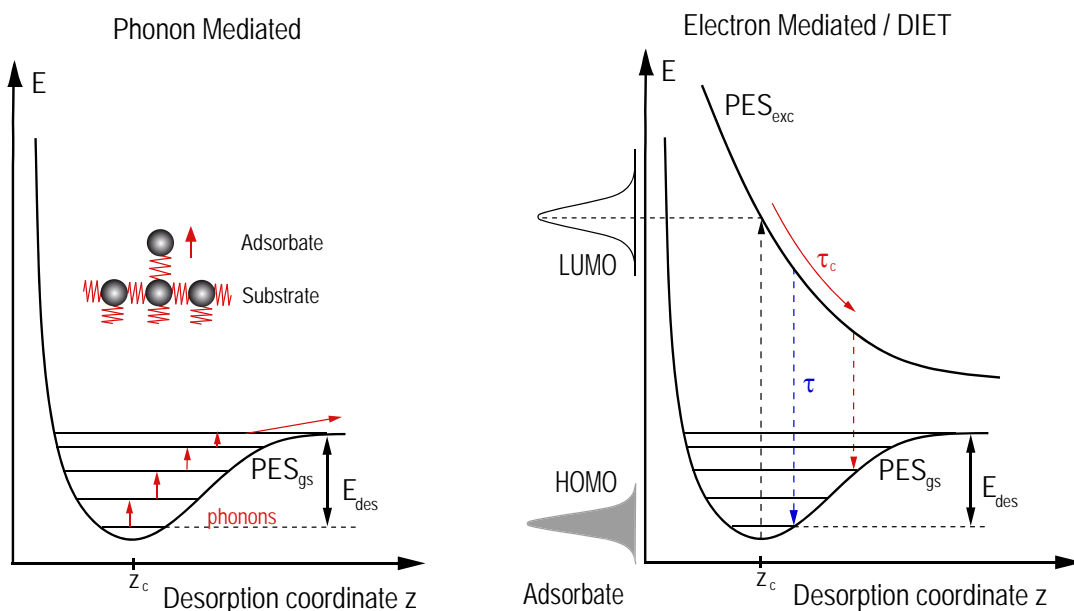


Fig. 2.1: Electron- vs. phonon-mediated desorption: Whereas phonon-mediated desorption involves 'vibrational ladder-climbing' out of the vibrational ground state (left), an electronic mechanism involves an electronically excited state of the adsorbate (right).

That such non-adiabatic processes take place in surface reactions was demonstrated for example for adsorption processes. Three possible energy dissipation processes have been found in case of adsorption: exoelectron emission, surface chemiluminescence, and electron-hole pair creation [43]. Excited electrons with sufficient energy, larger than the metal work function, may overcome the surface barrier, leading to the emission of so-called chemically induced exoelectrons into vacuum, which were observed during chemisorption of halogen- or oxygen molecules on alkali metals.

Excited electron-hole pairs may recombine under emission of photons, which is called surface chemiluminescence. Chemically created hot electrons and holes have been directly detected as chemicurrents in thin films.

Desorption Induced by Electronic Transitions - DIET

Desorption of adsorbates from metal surfaces can be induced adiabatically (phonon mediated) or non-adiabatically (electron mediated). Thermal activation of the substrate is transferred through surface phonons that couple vibrational energy to the reaction coordinates and cause desorption of the adsorbate (see left side of Fig. 2.1). In case of electronically induced desorption an electron is usually excited from the metal substrate to an unoccupied adsorbate level (LUMO) or a hole is created in an occupied adsorbate level (HOMO). Moving on the excited potential energy surface, potential energy can be transferred to kinetic energy to overcome the diffusion barrier (see right side of Fig. 2.1). This process is known as desorption induced by electronic transition (DIET). Since we would like to apply a similar model to describe electronically induced diffusion processes, we present here an overview of this excitation process.

Excitation of a metal surface by irradiation with electrons, with laser pulses or with an STM tip can excite the electronic system of the metal substrate, which can lead to desorption. This desorption process can be described by using the so-called MGR-model introduced by Menzel, Gomer, and Redhead [1,2]. In this model the electronic system of the adsorbate-substrate complex is characterized with two potential energy surfaces (PES). The potential energy surface PES_{gs} on the right side of Fig. 2.1 denotes the electronic ground state of the metal-adsorbate system. The excited state potential PES_{exc} is created by a vertical shift of the ground state with some excitation energy transferred into the substrate. For a metallic substrate continuous vertical displacements are allowed because of the continuum of electron-hole excitations. The initial step in this process is a so-called "Frank-Condon" transition from the ground potential energy surface (PES_{gs}) to an excited PES of the adsorbate complex [44, 19].

The ground state PES (PES_{gs} in Fig. 2.1) is often taken as an attractive Morse-potential where the characteristic parameters, the desorption well depth, the vibrational frequency, and the bonding geometry are inferred from independent experiments [45]. For the excited PES_{exc} , the expression of a conventional antibonding state is usually adopted to describe the desorption process. (In case of desorption of molecules on metals, as for example NO on Pd(111) [46], the excited PES is described as a negative ion applied by Gadzuk *et al.* [47, 45].) While moving on the excited PES_{exc} , the adsorbate converts potential energy to kinetic energy and can desorb if

it stays for a time which is longer than a certain critical time τ_c on this excited PES.

The efficiency of this process depends on the critical time τ_c which is needed to attain positive total energy before the adsorbate returns to the ground state. The desorption probability P can be estimated by the probability that the adsorbate remains on the excited PES for a time longer than τ_c . For $\tau \ll \tau_c$ it can be expressed as:

$$P \sim \exp(-\tau_c/\tau), \quad (2.1)$$

where τ is the lifetime of the excited state.

The MGR-model is a semi-classical model: the excitation-deexcitation processes are modeled quantum-mechanically, while the adsorbate motion is described classically [19]. Usually, the effect of the damping of the adsorbate-surface system is neglected [46].

A characteristic feature of a DIET mechanism is a linear dependence of the desorption yield on the excitation density, since the process is driven by single excitation events.

Desorption Induced by Multiple Electronic Transitions - DIMET

The DIET mechanism is usually not very efficient due to the short lifetime of excited adsorbate states on metal surfaces, which can be as short as some hundred attoseconds [48]. However, the desorption probability can be enlarged by several orders of magnitude if the density of excited electrons is high enough to enable multiple excitations of the adsorbate. A repetitive series of excitation and deexcitation cycles enlarged the effective resident time on the excited PES even if the lifetime is short (see Fig. 2.2.b). This regime, which has been consequently called DIMET [46], has been discovered by the application of intensive femtosecond laser pulses which can create a high density of hot electrons in the metal substrate (Fig. 2.2.a).

Initially, the optical excitation creates a highly non-equilibrium distribution of excited electrons with energies in the range $\epsilon_F \leq \epsilon \leq \epsilon_F + h\nu$, where ϵ_F is the Fermi energy, and $h\nu$ the photon energy [47]. Electron-electron scattering transforms this non-equilibrium distribution into a hot Fermi-Dirac distribution within a few hundred femtoseconds [49, 50, 51]. Although this process leads to a reduction of the average energy of the excited electrons, it creates also electrons with much higher energies, which can populate even high-lying unoccupied adsorbate levels.

In most observed cases desorption has been induced by this indirect excitation process. However, the excitation of the adsorbate can also be initiated by a direct optical transition from the HOMO or a metal bulk state into the LUMO of the adsorbate.

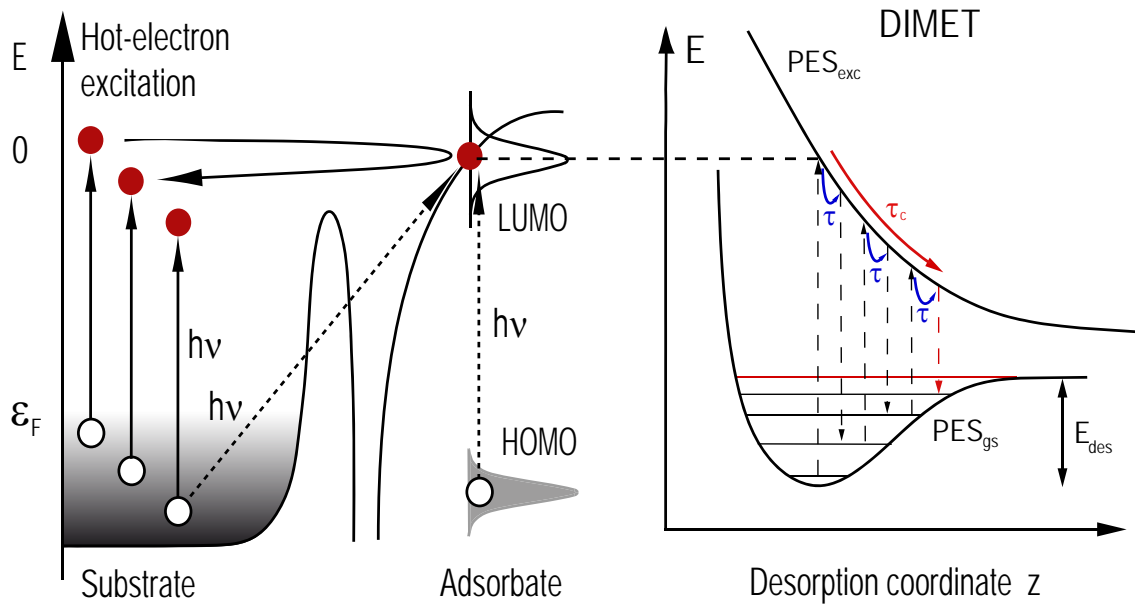


Fig. 2.2: Electronic excitation of the unoccupied state (LUMO) of the adsorbate occurs either indirectly by hot electron generation in the bulk followed by inelastic scattering with adsorbate, or directly by optical excitation from the occupied states of adsorbate (HOMO) or the substrate.

It is often difficult to distinguish a direct from an indirect excitation mechanism, since the electronic structure of the adsorbate is strongly perturbed by the metal substrate [52]. Polarization dependent measurements or better two-photon photoemission can unambiguously identify the underlying mechanism [53, 54, 55].

In the frame work of the DIMET model one needs information about the involved potential energy surfaces for quantitative conclusions about the desorption mechanism. However, these potentials are mostly not known precisely enough to perform complex trajectory-calculations.

Characteristics of DIMET Process

From the detailed study of ultrafast laser induced surface processes, such as the desorption of molecules like CO, NO or O₂ [3, 4, 46, 5, 6, 7, 10, 9], or the oxidation of CO molecules with pre-adsorbed oxygen [56, 8, 9, 12, 13], we can conclude the following main characteristics of electronically mediated processes:

- (a) Strong nonlinear dependence of the reaction probability on the absorbed laser

fluence ($P_{des} \propto F^n$, with $3 \leq n \leq 8$).

- (b) Information about the mechanism of the energy transfer between the substrate and the adsorbate can be gained from the so-called two-pulse correlation measurements. In these measurements the desorption yield is measured as a function of delay between two pump pulses that are used to induce desorption (for more information see Chap. 5.6). The two-pulse correlation of electronically induced surface processes shows a width which is typically in the range of 0.3 to 2 ps [4, 8, 10].
- (c) Strong excitation of the internal vibration of the desorbing molecules [3, 10].
- (d) Strong difference in the reaction pathways between thermal and femtosecond laser excitation [13, 56, 57].

2.2 Detection of Diffusion

Diffusion of adsorbates on surfaces has been studied by a variety of different techniques like methods based on work function changes (electron retardation technique, vibrating capacitor technique, field emission shadowing method, electron beam scanning methods (scanning Auger microscopy (SAM), laser induced desorption-refilling (LID)), fast scanning infrared interferometry (for example FIRAS), field ion microscopy (FIM), fluctuation autocorrelation methods (as field emission spectroscopy (FEM), nuclear magnetic resonance (NMR) techniques [58], scanning tunneling microscopy (STM)) and second-harmonic generation (SHG) measurements combined with a concentration grating [59].

In this work we have studied electronically induced diffusion. The different surface processes can be investigated with a technique which is capable to obtain information in real-time (picosecond time-resolution) and real-space (sub-nanometer temporal resolution) at the same time. The application of femtosecond laser-pulses gives an excellent tool to study diffusion with sub-picosecond time resolution. Highest spatial resolution of the surface processes can be in principle obtained by scanning tunneling microscopy (STM) [34, 31, 60].

As it was mentioned earlier, STM methods provide a real-space view of the individual atoms or molecules and the atomic landscape of their environment. The drawback of this technique is that it does not give direct information about the mechanism of the surface processes. Bartels and co-workers [34] have developed an experimental technique that combines the STM with short laser pulses, but temporal and spatial resolution cannot be obtained simultaneously. The surface cannot be irradiated

when the STM tip is in its tunneling position, because of the thermal expansion. By mapping the surface before and after the laser irradiation at the exactly same place, information about the final product of the adsorbate migration could be obtained [34].

Purely optical techniques have, in principle, not the spatial resolution to investigate individual atoms on a surface. Nevertheless, it is possible to obtain microscopic information about different binding sites if the optical response of these sites is distinguishable. In the following we will discuss two different techniques which can obtain information about surface diffusion on a microscopic scale by exploiting the different optical response of adsorbates at step and terrace sites on a vicinal surface.

The first technique is the infrared reflection spectroscopy (IRAS), which can be used only for molecular adsorbates, and it requires a relatively large difference between the vibrational resonance if the molecule binds at the step or terrace sites. The IRAS technique was used to study thermal activated diffusion of CO on vicinal Pt(111) surfaces by Reutt-Robey *et al.* [61] and migration of CO molecules from terrace to step sites on CO/Pt(335) induced by an electron gun [29]. These measurement were based on the fact that step sites act as a trap for the migrating CO molecules, and that the vibrational frequency of the CO stretch mode is $\approx 20 \text{ cm}^{-1}$ higher on terrace sites than on step sites. This allows to clearly distinguish between CO molecules chemisorbed on step and terrace sites. Using the technique of IRAS, it is possible to follow the evolution of the step and terrace site occupation at the same time. The spectra show that the signal of the terrace sites is decreasing and at the same time the signal of the step sites is increasing, which clearly indicates migration of the CO molecules from the terrace onto the step sites. In that way the spatial resolution of the migration is solved, but the time-resolution is missing because the migration was induced by continuous electron bombardment instead of short laser pulses.

The other is the second-harmonic generation (SHG), which is more general and which exploits the symmetry break at steps. The SHG technique was used to detect thermally induced diffusion of hydrogen on vicinal Si(001) surfaces by Raschke *et al.* [35]. The dissociative adsorption of hydrogen on vicinal Si(001) surface is highly site selective with a strong preference for double-height D_B steps. Raschke *et al.* have investigated the lateral motion and binding energy differences of different binding sites for atomic hydrogen on Si(001) surfaces. They monitored the time evolution of step and terrace hydrogen population with SHG.

In this work also the pure optical method, second harmonic generation is combined with a stepped surface, motivated by the work of Raschke *et al.* mentioned above. The measurements are based on the fact that under given conditions the SHG signal can be exclusively sensitive to the coverage at step sites of the surface. By inducing

diffusion with an intense femtosecond laser from the step sites onto terraces, the evolution of the step coverages can be followed with the SH signal. This technique will be introduced in the next paragraph.

2.2.1 Optical Second-Harmonic Generation (SHG)

In the present work, a purely optical technique is used to detect diffusion, namely the so-called optical second-harmonic generation (SHG). SHG is a special realization of the sum-frequency generation process (SFG) mentioned before, where both incoming beams have the same frequency. In the last decades SHG has been demonstrated to be sensitive to the structural properties of vicinal surfaces of cubic, centrosymmetric crystals and, what is particularly important here, to the presence of regular monoatomic steps [62]. The aim of this section is to describe the SHG response of systems with similar symmetry like the one that has been studied in the present work.

Phenomenological Model

At sufficiently high intensities the irradiation of the sample by laser pulses with frequencies $\omega_1 = \omega_2 = \omega$ induce a second-order nonlinear polarization. Within the electric-dipole approximation this second order nonlinear polarization can be expressed as:

$$\vec{P}^{(2)}(2\omega) = \chi^{(2)}(2\omega, \omega, \omega) : \vec{E}(\omega)\vec{E}(\omega) \quad (2.2)$$

or in components:

$$P_i^{(2)} = \sum_{j,k} \chi_{ijk}^{(2)} E_j E_k, \quad (2.3)$$

$\chi^{(2)}(2\omega)$ is the second-order nonlinear susceptibility, reflecting the nonlinear properties and symmetries of the excited medium, and E is the local electric field.

In general, bulk and surface of the sample will contribute to the irradiated signal. The surface sensitivity of this technique is based on the fact that the second-order nonlinear susceptibility is vanishing in the bulk of centrosymmetric materials. This can be easily understood from the behavior of $\chi^{(2)}$ under inversion operations. $\chi^{(2)}$ is a third-rank tensor, which means that it changes its sign under spatial inversion:

$$\chi^{(2)}(\vec{r}) = -\chi^{(2)}(-\vec{r}). \quad (2.4)$$

In centrosymmetric materials, the material inversion symmetry requires

$$\chi^{(2)}(\vec{r}) = \chi^{(2)}(-\vec{r}). \quad (2.5)$$

Eq. 2.4 and 2.5 can be just fulfilled with:

$$\chi^{(2)}(\vec{r}) \equiv 0. \quad (2.6)$$

On the other hand, a centrosymmetric bulk material has no inversion symmetry at the surface. Thus, $\chi^{(2)}$ does not vanish at the surfaces. This makes the dipole contribution to the second-order nonlinear process inherent surface sensitive for centrosymmetric materials. Higher-order terms can also lead to a nonlinear polarization that oscillates with 2ω , but often they can be neglected compared to the second-order response of the surface [63].

In general, the second-order nonlinear susceptibility $\chi_{ijk}^{(2)}$ is a third-rank tensor with 27 elements. For the case of SHG the number of independent tensor elements is reduced to 18 because the incoming photons are identical and therefore the last 2 indices can be exchanged.

After this reduction we can write the nonlinear polarization with its components in the following form [64]:

$$\begin{pmatrix} P_x^{(2)} \\ P_y^{(2)} \\ P_z^{(2)} \end{pmatrix} = \begin{pmatrix} \chi_{xxx}^{(2)} & \chi_{xyy}^{(2)} & \chi_{xzz}^{(2)} & \chi_{xzy}^{(2)} & \chi_{xzx}^{(2)} & \chi_{xxy}^{(2)} \\ \chi_{yxx}^{(2)} & \chi_{yyy}^{(2)} & \chi_{yzz}^{(2)} & \chi_{yzy}^{(2)} & \chi_{yzx}^{(2)} & \chi_{yyx}^{(2)} \\ \chi_{zxx}^{(2)} & \chi_{zyy}^{(2)} & \chi_{zzz}^{(2)} & \chi_{zzy}^{(2)} & \chi_{zzx}^{(2)} & \chi_{zxy}^{(2)} \end{pmatrix} \begin{pmatrix} E_x^2 \\ E_y^2 \\ E_z^2 \\ 2E_y E_z \\ 2E_x E_z \\ 2E_x E_y \end{pmatrix}. \quad (2.7)$$

So far, only the response of the sample in form of the nonlinear polarization was discussed. The quantity that was detected in the experiment is the intensity of the emitted second harmonic radiation. The radiation field $E(2\omega)$ generated by $P^{(2)}(2\omega)$ is obtained from the solution of the wave equation. In the electric-dipole approximation the second harmonic output intensity in the reflected direction is [65]:

$$I(2\omega) = \frac{8\pi^3 \sec^2 \theta_{2\omega}}{\hbar c^3 \epsilon_1(\omega) \sqrt{\epsilon_1(2\omega)}} \left| \vec{e}(2\omega) \cdot \chi_s^{(2)} : \vec{e}(\omega) \vec{e}(\omega) \right|^2 I_1^2(\omega). \quad (2.8)$$

$\theta_{2\omega}$ is the angle of reflexion and $\epsilon_1(2\omega)$ is the dielectric constant for the second harmonic frequency in the medium in which it will be radiated. For a sample in vacuum $\theta_1(2\omega)$ is equal to the fundamental incoming angle and $\epsilon_1(2\omega) = 1$. $\vec{e}(2\omega)$ and $\vec{e}(\omega)$ correspond to the unit polarization vectors $\hat{e}(2\omega)$ and $\hat{e}(\omega)$ after the appropriate Fresnel transformation, e.g. $\vec{e}(\omega) = F_{1 \rightarrow 2}(\omega) \hat{e}(\omega)$.

The actual numerical values of the Fresnel factors depend on the phenomenological model that is used. Different approaches have been worked out, depending on the studied physical system.

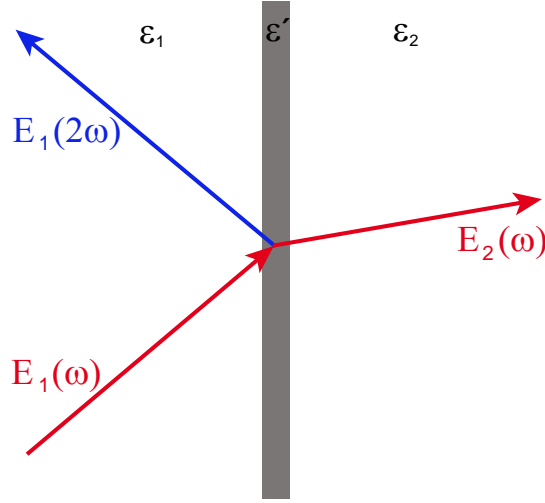


Fig. 2.3: Geometry of second-harmonic generation (SHG) from an interface in the reflected direction of specular reflection. A polarization sheet with dielectric constant ϵ' is imbedded between two media with inversion symmetry and dielectric constants ϵ_1 and ϵ_2

The first phenomenological, macroscopic model was suggested by Heinz [66]. He assumed an interface between two materials (Fig. 2.3) with dielectric constants ϵ_1 and ϵ_2 , that are separated with a finite sheet with dielectric constant ϵ' where the nonlinear response take place. This considers that also the linear optical properties at the surface differ compared to the bulk, what is particularly important for semiconductor surfaces with their characteristic localized dangling bonds.

For this geometry the fields are calculated by applying the boundary conditions at the interface for a sheet with finite thickness. Afterwards an infinite thin sheet is considered. The explicit form of the Fresnel factors here is the following [37]:

$$F_{i \rightarrow j} = F_{i \rightarrow j}^{xx} \hat{x}\hat{x} + F_{i \rightarrow j}^{yy} \hat{y}\hat{y} + F_{i \rightarrow j}^{zz} \hat{z}\hat{z} \quad (2.9)$$

with

$$F_{i \rightarrow j}^{xx} = \frac{2\epsilon_i q_j}{\epsilon_j q_i + \epsilon_i q_j}, \quad (2.10)$$

$$F_{i \rightarrow j}^{yy} = \frac{2q_i}{q_i + q_j}, \quad (2.11)$$

$$F_{i \rightarrow j}^{zz} = \frac{2\epsilon_i \epsilon_j}{\epsilon'} \frac{q_i}{\epsilon_j q_i + \epsilon_i q_j}. \quad (2.12)$$

The indices $i \rightarrow j$ indicate between which media the wave is propagating: $1 \rightarrow 2$ or $2 \rightarrow 1$.

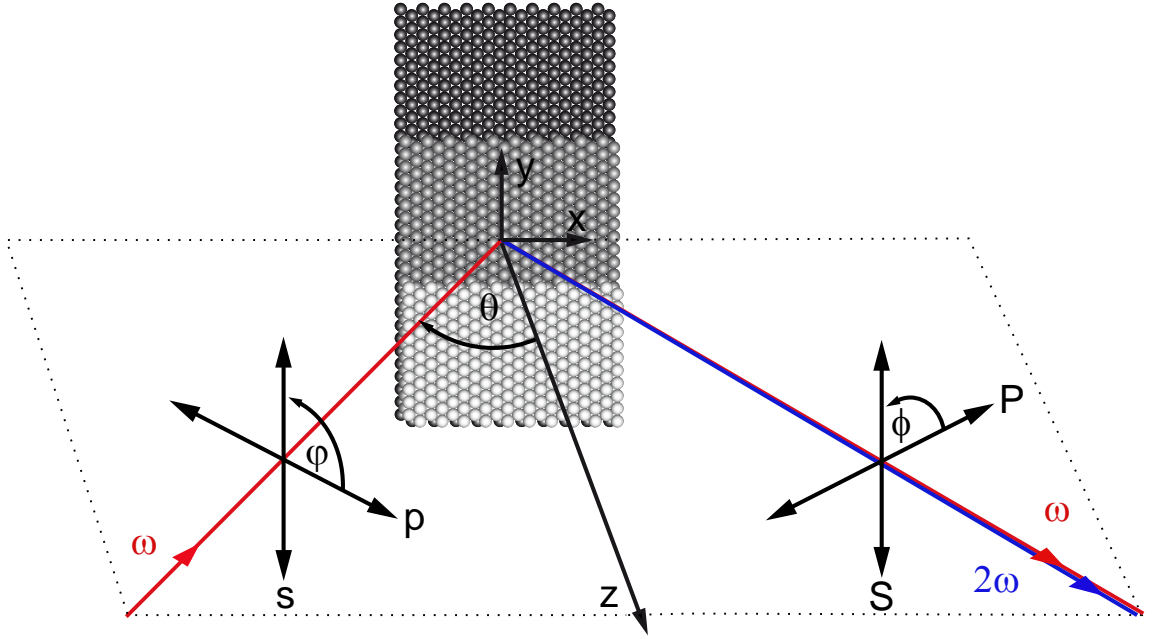


Fig. 2.4: Experimental geometry for the SHG experiments on vicinal surfaces

Assuming that the magnetic properties of the media can be neglected ($\mu = 1$), q_i and q_j are projections of wavevectors onto the surface normal and can be calculated together with the propagation directions of the incoming and emitted beams:

$$\vec{k}_1(2\omega) = p\hat{x} - q_1\hat{z} \quad ; \quad q_1 = \sqrt{\epsilon_1 K^2 - p^2} \quad (2.13)$$

$$\vec{k}_2(2\omega) = p\hat{x} + q_2\hat{z} \quad ; \quad q_2 = \sqrt{\epsilon_2 K^2 - p^2} \quad (2.14)$$

$$K = \frac{2\omega}{c}. \quad (2.15)$$

The benefit of this method is that it assigns not only a nonlinear susceptibility to the interface, but also describes the influence of the linear dielectric properties. This allows a better separation between the linear and nonlinear response. The explicit expressions for the second harmonic field as a function of the angle of incidence given by Sipe *et al.* can be obtained by setting $\epsilon'(\omega) = \epsilon_2$ and $\epsilon'(2\omega) = 1$. They are frequently used to describe SHG for metal surfaces, i.e. assuming an incident field in medium 2 and radiating 2ω -polarization in vacuum.

SHG Sensitivity to the Surface Symmetry

The polarization dependence of the Fresnel factors presented on the last pages determines which components of the nonlinear susceptibility contribute to the generated

second harmonic radiation for different linear polarization combinations of incoming and reflected beams. This reduces the number of probed tensor elements already significantly without considering further restrictions due to surface symmetries. To illustrate this statement, it is useful to visualize these contributing elements of the χ^2 tensor for different polarization combinations:

$$\begin{array}{ccc}
 p \rightarrow P & s \rightarrow P & 45^\circ \rightarrow P \\
 \left(\begin{array}{cccccc} \bullet & \circ & \bullet & \circ & \bullet & \circ \\ \circ & \circ & \circ & \circ & \circ & \circ \\ \bullet & \circ & \bullet & \circ & \bullet & \circ \end{array} \right) & \left(\begin{array}{cccccc} \circ & \bullet & \circ & \circ & \circ & \circ \\ \circ & \circ & \circ & \circ & \circ & \circ \\ \circ & \bullet & \circ & \circ & \circ & \circ \end{array} \right) & \left(\begin{array}{cccccc} \circ & \circ & \circ & \circ & \circ & \circ \\ \bullet & \bullet & \bullet & \bullet & \bullet & \bullet \\ \circ & \circ & \circ & \circ & \circ & \circ \end{array} \right) \\
 \\
 p \rightarrow S & s \rightarrow S & 45^\circ \rightarrow S \\
 \left(\begin{array}{cccccc} \circ & \circ & \circ & \circ & \circ & \circ \\ \bullet & \circ & \bullet & \circ & \bullet & \circ \\ \circ & \circ & \circ & \circ & \circ & \circ \end{array} \right) & \left(\begin{array}{cccccc} \circ & \circ & \circ & \circ & \circ & \circ \\ \circ & \bullet & \circ & \circ & \circ & \circ \\ \circ & \circ & \circ & \circ & \circ & \circ \end{array} \right) & \left(\begin{array}{cccccc} \bullet & \bullet & \bullet & \bullet & \bullet & \bullet \\ \circ & \circ & \circ & \circ & \circ & \circ \\ \bullet & \bullet & \bullet & \bullet & \bullet & \bullet \end{array} \right)
 \end{array} \tag{2.16}$$

The polarization 45° addresses a linear polarization between s and p and the filled dots highlight the contributing tensor elements. The illustration shows clearly that different tensor elements can be addressed by choosing a certain polarization combination.

Consideration of the symmetry of the surface that is studied will lead to further restrictions. For the bulk of centrosymmetric materials we showed already that $\chi^2 = 0$. For a (111) surface of a cubic, centrosymmetric crystal with C_{3v} symmetry χ^2 has the following non-vanishing elements (considering the case that the \mathbf{y} -axis is perpendicular to the plane of symmetry and the \mathbf{z} -axis is normal to the surface) [37]:

$$\chi_{(111)}^{(2)} = \begin{pmatrix} \bullet & \bullet & \circ & \circ & \bullet & \circ \\ \circ & \circ & \circ & \bullet & \circ & \bullet \\ \bullet & \bullet & \bullet & \circ & \circ & \circ \end{pmatrix} \tag{2.17}$$

Furthermore, there are only four independent parameters, because the tensor elements have to fulfill the following relations:

$$\chi_{xxx}^{(2)} = -\chi_{xyy}^{(2)} = -\chi_{yxy}^{(2)} \tag{2.18}$$

$$\chi_{xzx}^{(2)} = \chi_{yzy}^{(2)} \tag{2.19}$$

$$\chi_{zxx}^{(2)} = \chi_{zyy}^{(2)} \tag{2.20}$$

$$\chi_{zzz}^{(2)} \tag{2.21}$$

SHG from Vicinal (111) Surfaces

Whereas the description of the flat, low-index (111) surface presented so far seemed to be quite straightforward, vicinal surfaces are in general difficult to handle since the terraces are not perpendicular to the surface any more. Lüpke *et al.* extended the model for the second- and third-harmonic generation from cubic centrosymmetric crystals with vicinal faces [40] using the convention of Sipe.

In a first order approximation, regular steps can be described by an additional C_{1v} symmetry with the mirror plane perpendicular to the steps. For small miscut angles the electronic structure of the terraces will be very little affected by the steps. The total nonlinear response can then be approximated as the sum of independent contributions from the steps and the terraces:

$$\chi_{vicinal}^{(2)} = (1 - a) \chi_{terrace}^{\prime(2)} + a \chi_{step}^{(2)}. \quad (2.22)$$

a is the fraction of step edge atoms with respect to the number of terrace atoms.

It is important to recognize that the nonlinear susceptibility of the terrace is different from that of the flat surface, because the terrace is tilted with respect to the surface plane. We have to transform $\chi_{ijk}^{\prime(2)}$ from the coordinate system of the vicinal surface to the laboratory system [40]:

$$\chi_{ijk}^{\prime(2)} = \sum_{\ell, m, n} R_{i\ell} R_{jm} R_{kn} \chi_{\ell mn}^{(2)}. \quad (2.23)$$

$\{R_{ij}(\alpha_1)\}$ is the matrix for the transformation between the cubic crystal coordinate system and the coordinate system for the C_{1v} symmetry face. In the case of a (001) face miscut toward [011] with misorientation angle α_1 , $\{R_{ij}(\alpha_1)\}$ takes the form

$$\{R_{ij}(\alpha_1)\} = \begin{pmatrix} \cos \alpha_1 & 0 & \sin \alpha_1 \\ 0 & 1 & 0 \\ -\sin \alpha_1 & 0 & \cos \alpha_1 \end{pmatrix} \quad (2.24)$$

The indices i, j and k are the x, y and z coordinates of the laboratory system and l, m , and n are the x, y and z coordinates of the crystal [40]. For a vicinal surface with the mirror-plane perpendicular to the x -axis (and therewith perpendicular to the mirror plane of the flat surface discussed before!) the nonlinear susceptibility has the following form:

$$\chi_{step}^{(2)} = \begin{pmatrix} \circ & \circ & \circ & \circ & \bullet & \bullet \\ \bullet & \bullet & \bullet & \bullet & \circ & \circ \\ \bullet & \bullet & \bullet & \bullet & \circ & \circ \end{pmatrix} \quad (2.25)$$

If the mirror-plane is perpendicular to the y-axis, $\chi^{(2)}$ looks like:

$$\chi_{step}^{(2)} = \begin{pmatrix} \bullet & \bullet & \bullet & \circ & \bullet & \circ \\ \circ & \circ & \circ & \bullet & \circ & \bullet \\ \bullet & \bullet & \bullet & \circ & \bullet & \circ \end{pmatrix} \quad (2.26)$$

(compare Fig. 2.7 for the orientation of surface and different step types.)

Again, the positions with filled circles indicate non-vanishing elements. In contrast to the (111) surface discussed before, the C_{1v} symmetry causes no further restrictions for the actual numerical values of the tensor elements: they are all independent. Although the exact values of the tensor elements are in general not known, we can get some information about the second-harmonic signal generated at our sample already just from the form of the tensor presented so far.

Azimuthal Rotation of the Crystal

Different surface symmetries may be distinguished by measuring the dependence of the SH yield as a function of azimuthal angle ψ of the sample, i.e. the rotational anisotropy [67].

For rotating the sample with ψ around the surface normal (\hat{z}) the transformation matrix has the form:

$$\begin{pmatrix} \cos \psi & -\sin \psi & 0 \\ \sin \psi & \cos \psi & 0 \\ 0 & 0 & 1 \end{pmatrix} \quad (2.27)$$

The SH signal dependence on azimuthal angle gives a possible technique to distinguish between different surfaces. Figure 2.5 shows simulations of this azimuthal angle dependence of the generated second harmonic field on the sample orientation for fixed, linear polarizations of the fundamental and second harmonic beams for (111), (100), and (110) surfaces. For this illustration on figure 2.5 the following nonlinear susceptibilities $\chi^{(2)}$ have been chosen:

$$\chi_{terrace,(111)}^{(2)} = \begin{pmatrix} 1 & -1 & 0 & 0 & 1 & 0 \\ 0 & 0 & 0 & 1 & 0 & -1 \\ 0.2 & 0.2 & 10 & 0 & 0 & 0 \end{pmatrix} \quad (2.28)$$

$$\chi_{terrace,(100)}^{(2)} = \begin{pmatrix} 0 & 0 & 0 & 0 & 1 & 0 \\ 0 & 0 & 0 & 1 & 0 & 0 \\ 0.2 & 0.2 & 10 & 0 & 0 & 0 \end{pmatrix} \quad (2.29)$$

$$\chi_{terrace,(110)}^{(2)} = \begin{pmatrix} 0 & 0 & 0 & 0 & 0.8 & 0 \\ 0 & 0 & 0 & 0.5 & 0 & 0 \\ 0.2 & 1 & 10 & 0 & 0 & 0 \end{pmatrix} \quad (2.30)$$

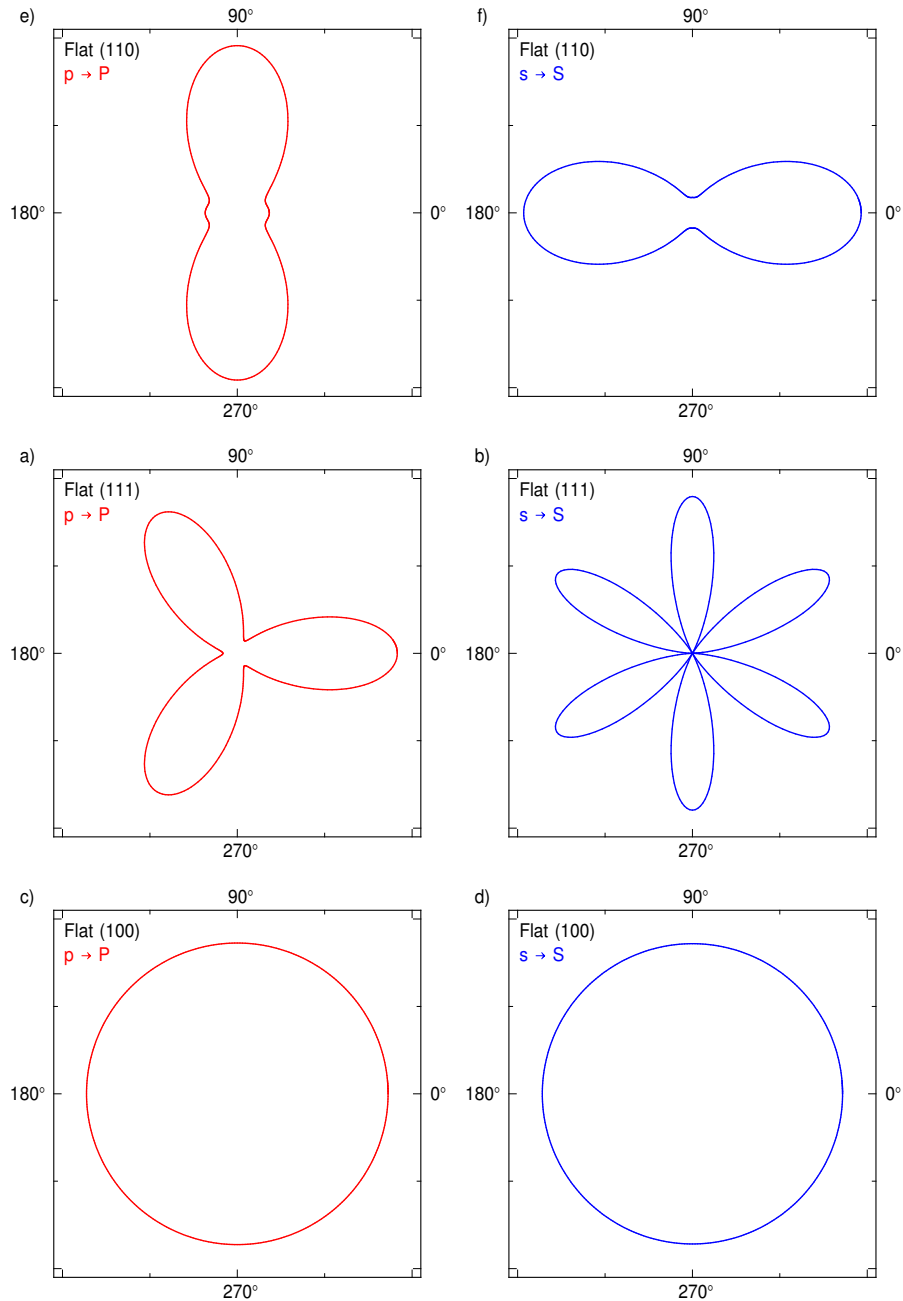


Fig. 2.5: Simulation of the azimuthal dependence of the SHG from the flat a and b (110), c and d (111), and e and f (100) clean surfaces. See Eq. 4.1, 2.29, and 2.30 for the assumed nonlinear susceptibilities for these surfaces. (All figures are normalized.)

A rule of thumb has been applied for the choice of the magnitude of the tensor elements of these flat surfaces. For a metallic surface the nonlinearity will be particularly large for a polarization in the direction perpendicular to the surface (z). Therefore, it can be expected that $\chi_{zzz}^{(2)}$ may be the largest element. For the jellium model $\chi_{xxx}^{(2)} = \chi_{yyy}^{(2)} = \chi_{zzz}^{(2)} = \chi_{zyy}^{(2)}$. The other tensor elements were chosen in a way that for the (111) surface the simulation agrees qualitatively with the experimental data obtained with our sample (shown later in Fig. 4.4). For our (111) vicinal surface it will be demonstrated that the SHG measurements don't show phase shifts (see Sect. 4.5), therefore the tensor elements can be chosen as real numbers although in general they are complex quantities.

For the (100) and (110) surfaces $\chi_{zzz}^{(2)}$ was chosen to have the largest magnitude, all other elements are arbitrary. The plots show the two- and threefold symmetry of the (110) and (111) surfaces. Since $\chi^{(2)}$ is a third-rank tensor, fourfold and higher symmetries can not be distinguished. Therefore the azimuthal dependence of the SH yield for the (100) surface is isotropic (see Fig. 2.5).

2.3 Oxygen on Pt(111) Surfaces

As a model system we have chosen the dissociative adsorption of oxygen on a vicinal Pt(111) surface. It is well studied by a variety of methods like thermal desorption spectroscopy (TDS), high-resolution electron-energy loss spectroscopy (HREELS), scanning tunnel microscopy (STM), molecular beam experiments, and core level spectroscopy methods (see Ref. [68,69] and references therein).

The aim of this section is to give a general overview of the platinum (111) single crystal surface and the possible adsorption sites of oxygen atoms on it.

2.3.1 Pt(111) Surface

Many metals crystallize in the face-centered cubic (fcc) structure like for example the catalytically important precious metals as platinum, ruthenium, and palladium.

The (111) surface can be obtained by cutting the fcc metal in such a way that the surface plane intersects the x-, y- and z- axes at the same value. This exposes a surface with an atomic arrangement of sixfold (hexagonal) symmetry.

This layer of surface atoms actually corresponds to one of the close-packed layers on which the fcc structure is based. Each surface atom has six nearest neighbors in the first layer, and another three in the layer immediately below. Altogether the coordination number of a surface atom is 9.

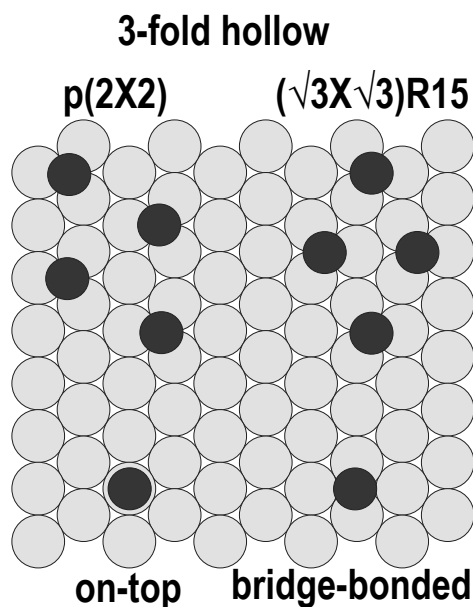


Fig. 2.6: The 111 surface offers the following adsorption sites : on-top sites, bridging sites (between two atoms) and hollow sites (between three atoms).

If we expose this surface to adsorbates it offers three adsorption sites: on-top sites, bridge bonding sites (between two atoms), and threefold hollow sites (between three atoms) (see Fig 2.6). There are two different threefold hollow sites: the hcp (hexagonal close-packed) and the fcc (face centered cubic) three-fold hollow sites (see Fig. 2.7). The difference between these two bonding places is that in case of hcp-hollow a Pt atom is situated in the under-laying terrace while in the case of fcc-hollow not.

Vicinal Pt(111)

Platinum crystals cut in different crystallographic zones at small angles from (111) planes result in surfaces with regular arrays of steps. The ideal surfaces can be considered to consist of terraces which have an atomic arrangement identical to the corresponding low index surface, separated by a single atom height (so called monoatomic) steps.

Real vicinal surfaces do not exhibit a completely regular array of steps and kinks illustrated for the ideal surface structures, but they do exhibit a certain type of step and terrace morphology. The special adsorption sites at steps are widely recognized to have remarkably different adsorption characteristics compared to those available on the terraces and may thus play an important role in surface reactions.

In the case of Pt(111) three different types of monoatomic step exist for three

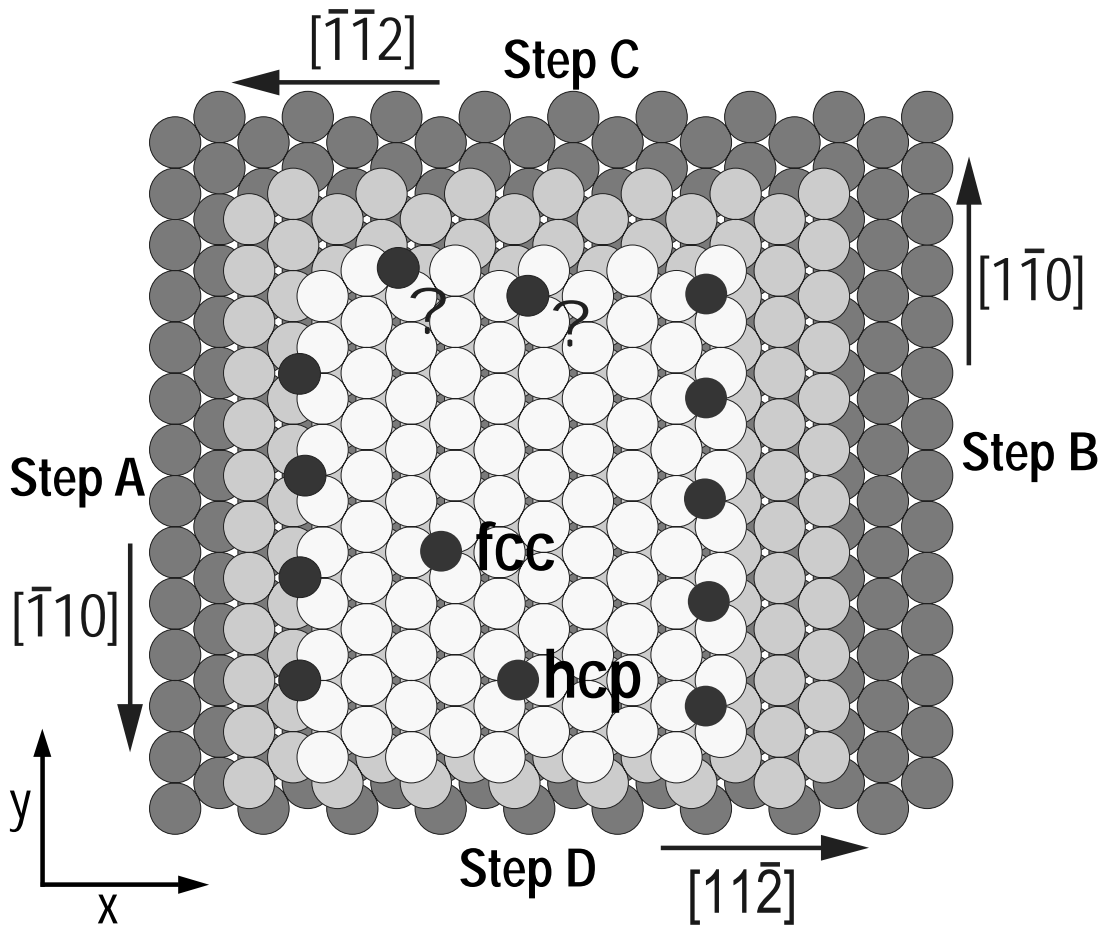


Fig. 2.7: The three (A, B, C=D) different step morphologies of the vicinal Pt(111) and the possible bonding sites of the atomic oxygen at them. The two adatoms on the highest terrace are for notation of the hcp (hexagonal close-packed) and the fcc (face centered cubic) three-fold hollow sites.

different surface facets, depending on the cut direction (see Fig 2.7). If the [111] direction is tilted into the direction of $[11\bar{2}]$, $[112]$ (see three dimensional sketch on Fig. 5.11) and $[1\bar{1}0]$, the steps have facets of (111), (100) and $(1\bar{1}0)$ orientation respectively. Each step atom of the (111) and (100) facets has 7 neighbors. 4 nearest neighbors in the surface layer of terrace atoms which terminates at the step, and another 3 in the layer immediately below. But the cut in the $[1\bar{1}0]$ direction exhibits not only steps but also contains kinks in the steps. The lowest coordination number is exhibited by atoms "on the outside" of the kinks in the steps. Such atoms have only 3 nearest neighbors in the surface layer of terrace atoms which terminates at the step, and another 3 in the layer immediately below - a total of 6.

There are two notations of the vicinal surfaces. One possibility is to describe the

vicinal surface with the generally used Miller indices. These indices for the different steps shown in Fig. 2.7 are the following: step A is Pt(114), step B is Pt(441), step C is Pt(310), and step D is Pt(021). Alternative designation for the surfaces are for A steps Pt(2(111)+(112)), for B steps Pt(3(111)+(112)), for C steps Pt(2(111)+(110)), and for D steps Pt(1(111)+(110)). Here the first numbers denote the (111) terrace length of the crystal and the the second brackets show the step directions. Applying these notations on our sample the appropriate Miller indices are Pt(10,12,11), while the other one is Pt(11(111)+(110)). This means that the crystal has (111) terraces with a width of 11 unit cells and the step staircase drops down from the 110 direction.

2.3.2 Adsorption of Oxygen on Stepped Pt(111)

In the literature the following picture has been established for the oxygen adsorption on platinum: Below 40 K, molecular oxygen physisorbs on the surface. Three chemisorbed molecular states have been found, which were assigned to fcc- and bridge-bonded terrace and step-bonded species with peak desorption temperatures between 125 and 220 K. Two much more strongly bound atomic oxygen states have been observed, corresponding to terrace- and step-bonded species, which are desorbing recombinatively and give rise to broad desorption peaks between 700 and 900 K.

Both, molecular precursor-mediated and quasi-direct dissociation can be observed, depending on the initial conditions [70]. For temperatures $T > 150$ K, only atomic oxygen is stable on the surface forming a $p(2 \times 2)$ superstructure on the terraces at the saturation coverage of 0.25 ML by occupying the fcc sites which are preferred by 0.4 eV compared to hcp sites [71, 72, 73]. For initial energies in the thermal range, oxygen sticks as molecular species on terraces at $T < 150$ K with a saturation coverage of 0.44 ML building a $(3/2 \times 3/2)R15^\circ$ structure [74], where it partially desorbs and partially dissociates when the temperature is increased above 150 K.

Steps increase the reactivity dramatically [69, 75, 76]. STM investigations at temperatures lower than 160 K, where atomic oxygen is immobile, have shown that the dissociative adsorption takes place directly at the step edges [77].

Adsorption on Different Step Facets

Since on the Pt(111) surface 3 different types of monoatomic step exist there are also different adsorbate sites for the oxygen (see Fig. 2.7).

STM studies of Feibelman *et al.* [71] gave clear evidence that the atomic oxygen binds differently on the (111) (steps point into direction [112] on Fig. 2.7, called A-type step) and on the (100) (steps point into direction [112] on Fig. 2.7, called B-type

step) facets. They have also attained local density approximation (LDA) calculations that have supported their observation made by STM images [71, 78].

These studies reveal that an oxygen adatom gains binding energy roughly proportional to the number of its nearest neighbors that are step-edge atoms. The gain is 0.25 eV if the oxygen atom has only one step-edge neighbor, 0.4 eV if the oxygen atom nearest neighbors are one terrace and two step-edge atoms, and 0.6 eV if the ad-oxygen hangs off the step edge, coordinated only to two step-edge Pt atoms.

Step-edge atoms, on both A and B steps, have 7 neighbors, compared to 9 for terrace atoms and 10 (A) or 11 (B) for step-bottom atoms. Thus, the total energy of the system is mostly lowered when oxygen adatoms decrease the need of the edge Pt atoms for neighbors [71].

A-type Steps

In the case of an A-type step the oxygen adatom shows up right at the step. It is bonded between two edge atoms where no Pt atom is directly below the oxygen adatom on the lower terrace in front of the step (see Fig. 2.7).

In the edge-bridging site, the oxygen passivates two edge neighbors and it is a “quasi-fcc” site. It is not a threefold site, since there is a step present and with it a Pt neighbor is missing. Although there is an adjacent threefold over-terrace site which also allows passivation of two step-edge Pt atoms, but it is a hcp hollow, and the fcc site is preferred to hcp by ~ 0.4 eV. The extra binding accrued by passivating two edge Pt atoms and it is decisive and makes the edge-bridging site optimal [71].

There is a fcc-hollow at an A step that allows an oxygen adatom to have only one Pt edge neighbor. But it provides only 0.25 eV advantage of passivating only one step edge Pt, plus the fcc hollow advantage of 0.4 eV [71].

B-type Steps

At the B-type step (see Fig. 2.7) the hcp binding is extended to edge bridging, where a Pt atom is on the lower terrace in front of the step below the adsorbed oxygen atom. Here an oxygen adatom prefers the threefold, over-terrace site because it is an fcc hollow, adjacent to two step-edge Pt atoms, occurring a passivation energy gain of 0.4 eV. This is 0.2 eV better than the quasi-hcp edge bridge, where 0.6 eV passivation energy gain is counteracted by a 0.4 eV hcp penalty [71].

C- and D-type Steps

The other two possibilities actually are the same. The $[111]$ direction is tilted into the $[1\bar{1}0]$ or the $[110]$ direction and the steps edges are parallel to the $[11\bar{2}]$ direction. The step staircase drops down from the $[1\bar{1}0]$ or the $[110]$ direction, respectively (see Fig. 2.7). Here in the both cases, the steps are not straight but they contain kinks (Sec. 2.3.1). For our study we have used a Pt sample with C-type steps.

There is no information about the oxygen adsorption for this type of steps in the literature, but we can assume from the discussion above that the outside atoms of the kinks possibly play important roles (see Fig. 2.7), because they have the lowest coordination number (6). From our SHG experiments we can only deduce that oxygen sticks at the steps, but cannot assign the correct position.

Chapter 3

Experimental Setup

This chapter provides a description of the experimental setup that was employed in the present work. The first section gives an overview of the ultra-high vacuum (UHV) system (Sect. 3.1) which was built up within the framework of this PhD work and optimized for the diffusion measurements. The second section (Sect. 3.2) describes the preparation of the platinum sample, and the last section describes the optical setup and the laser system (Sect. 3.3).

3.1 Ultra-High Vacuum System

The creation and maintenance of UHV conditions is the prerequisite for every investigation of atomically clean surfaces. The detailed characterization of the vacuum conditions and the inspection of the sample required the presence of several measurement instruments within the UHV chamber. The sample manipulator needed to provide a large number of translation and rotation degrees of freedom, while allowing for a large range of sample temperature.

The scheme of the UHV chamber is depicted in the Fig 3.1. The vacuum-system is separated into two subsystems, the measuring chamber and the dosing system. Both systems have the same fore-vacuum system which contains a rotary pump (RP, Leybold Trivac D25B) and a fore-line trap (FT, Balzers URB 025). The latter prevent oil-contaminations of the main system. The measuring chamber and the dosing-system can be separated via an electro-pneumatic protection valve (EPV, Balzers EVA 040PC).

Measuring Chamber

The chamber can be separated from the pumping unit located underneath via a 200 mm gate valve (GV, VAT 200). A turbo-molecular pump (TP1, Balzers TMU 260), an ion-getter pump (IGP, Varian Star Cell 230 l/s) and a Ti-sublimation pump (TSP) are attached to a four-way crossing. The system pressure is recorded with a

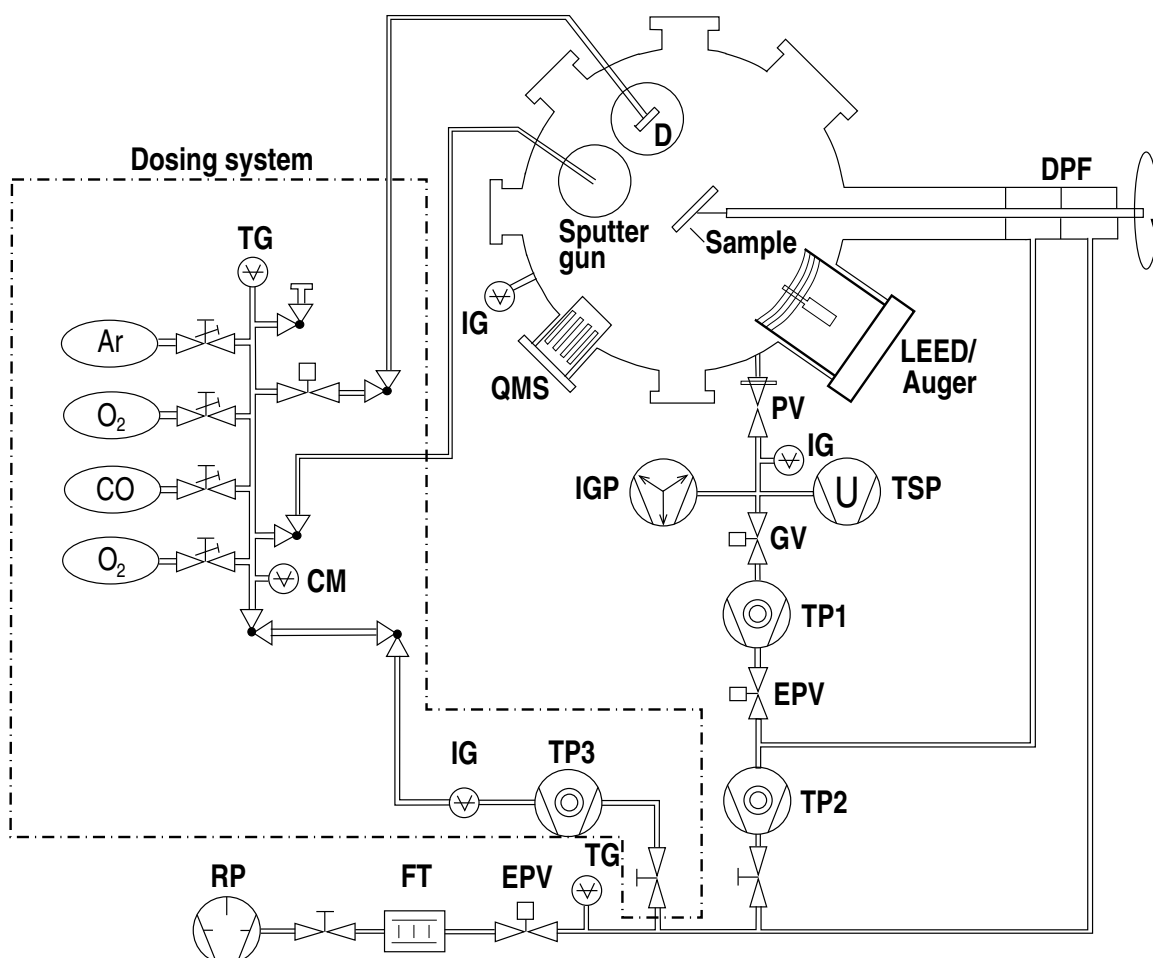


Fig. 3.1: Schematic representation of the UHV system consisting of a separately pumped gas dosing system (left side) and the UHV chamber. The abbreviations are:

P1, TP2, TP3	Turbomolecular pumps (Balzers), 270l/s, 60l/s, 60l/s
TSP	Titanium sublimation pump
IGP	Ion getter pump, Star Cell (Varian), 220l/s
RP, FT	Rotary pump, Foreline trap
DPF	Differentially pumped feedthrough
IG, TG	Ionization gauge, Thermocouple gauge
CM	Capacitance manometer
GV, PV	Gate valve CF200, Plate valve CF200
EPV	Electro-pneumatic protection valve
D	Doser with capillary array plate, $\phi = 25\text{mm}$, $\phi_{\text{porous}} = 5\mu\text{m}$

Bayard-Alpert gauge (IG, Balzers IMR 132). A smaller turbo-molecular pump (TP2, Balzers TMU 065) has been attached between the TP1 and the fore-vacuum system.

The sample preparation and measuring chamber is equipped with a combined

retarding-field LEED/Auger instrument (Omicron, Spectaleed), a quadrupole mass spectrometer (Balzers, QMS 125) and a sputter gun (VSW AS10). The LEED/Auger equipment is used for the characterization of the sample surface. The QMS is used for temperature programmed desorption (TPD) and for rest gas analysis. The QMS is equipped with a molybdenum "Feulner cap" [79, 80] around the ionizer and is mounted on a translation stage. It can be reproducibly positioned in front of the sample (typical distance 3 mm). With application of the Feulner cap atoms and ions desorbing exclusively from the surface of the sample can be collected. The exclusion of atoms desorbing from the backside of the sample or from the sample holder is crucial for high-quality TPD-spectra. The sputter gun is used for cleaning the sample surface (see in Sect. 3.2).

The whole chamber was baked out at a temperature of 430K to get rid of the water contamination. This temperature is limited by the maximal allowable temperature of the rotary manipulator feed-rough. After typically two days of bake out a base pressure $\leq 1 \times 10^{-10}$ mbar is obtained for the main chamber. For the dosing system a pressure in the lower 10^{-9} mbar range is reached.

Dosing System

The dosing system contains four glass bulbs for various gases, a Bayard-Alpert gauge (IG, Leybold Ionivac IE211) recording pressures below 10^{-3} mbar, a thermocouple manometer (TG, Leybold-Hereaus) for pressures above 10^{-3} mbar and a calibrated capacitance manometer (MKS, Baratron, Model 615A), which was used for recording the gas flow from the dosing system to the chamber. The dosing-system which is pumped independently from the main system with a turbo-molecular pump (TP3, Balzers TPU 062), is attached to the chamber via two angle valves. One is attached to the sputter gun to let in argon for the sample preparation and the other is attached to a motorized leak-valve which allows the dosage of oxygen or CO through a micro-capillary array. The latter permits a uniform and directed gas flow onto the sample.

Sample Holder

The optical measurements require the accurate positioning of the sample in space. The sample manipulator can be freely translated in x-, y- and z-direction with an accuracy in the μm range. Rotation around the vertical axis is possible over the entire 360° . This can be achieved with the help of a rotary feed-through which was differentially pumped.

The round platinum sample is clamped between a bended tungsten wire. The tungsten wire is clamped to a copper block which is attached to a liquid-nitrogen

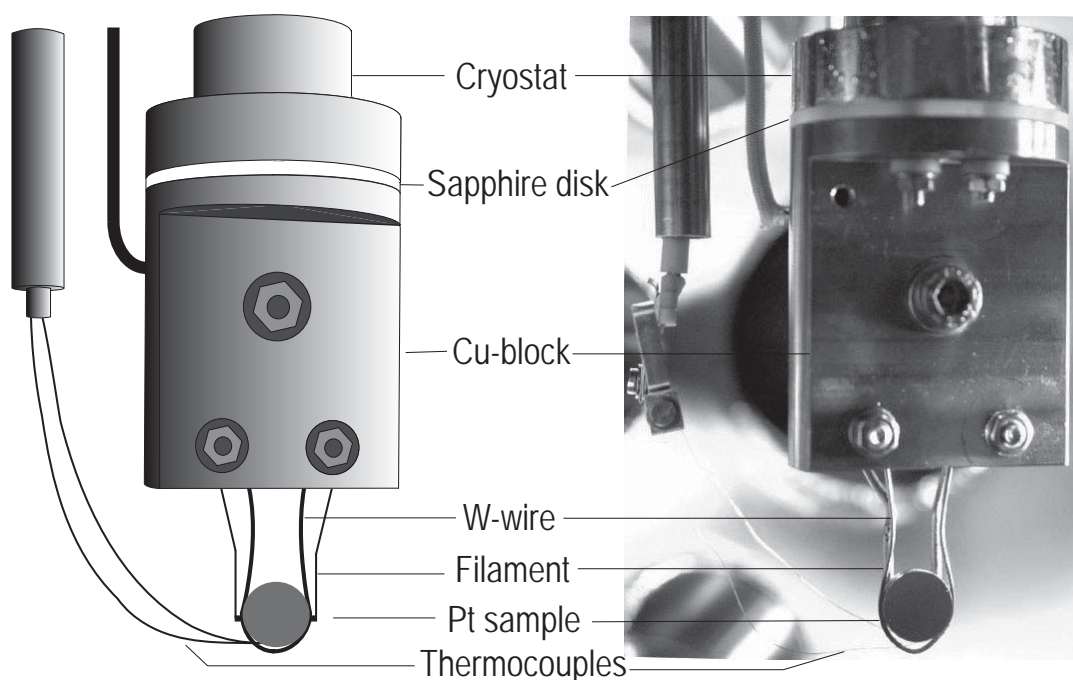


Fig. 3.2: Schematic structure of the sample holder.

cooled cryostat separated by an insulating sapphire disk. The sample could be cooled down to 80 K and heated up to 1100 K by radiation and electron-beam heating. The temperature was monitored by means of a chrome-alumel thermocouple (type K) that is spot welded to the back side of the platinum sample.

3.2 Platinum Surface Preparation

Besides clean UHV conditions, the sample preparation procedure is very important to obtain clean and ordered surfaces.

The Pt(10,12,11) crystal with a diameter of 12 mm and thickness of 2 mm was supplied by MaTeck. It has a circular groove with a width of 0.3 mm and depth of 0.8-1 mm for fixing. The sample was oriented 4° off the (111) direction in the $[\bar{1}\bar{1}0]$ direction and polished down to a roughness of $0.03 \mu\text{m}$. With this miscut it has a terraces width of 11 unit cells length (see in Ref. [61]) that are separated by monoatomic steps. Steps were chosen to be parallel to the plane of incidence of the laser beams and parallel to the $[11\bar{2}]$ direction.

The sample was cleaned by repeated sputtering cycles. First the sample was sputtered with Ar^+ ions for 10 minutes at 1keV and $2.5 \mu\text{A}$. After that it was annealed at 1050 K for 10 minutes. During this high temperature annealing carbon contami-

nations can come up from the platinum bulk. This residual carbon contaminations can be removed by oxidation of the sample. During oxidation the sample was hold at 720 K in an atmosphere of 5×10^{-8} mbar O_2 for 30 minutes. Finally, oxygen was removed by flashing the sample to 1100 K. This procedure was repeated at least 30 times.

After the preparation procedure the quality of the surface was inspected by LEED and Auger electron spectroscopy (AES). The LEED pattern in Fig. 3.3 shows sharp diffraction spots of the Pt(111) surface. Every second pattern is splitted being a clear sign of regularly stepped surface. The cleanness of the sample was further analyzed with repeated TPD and SHG measurements.

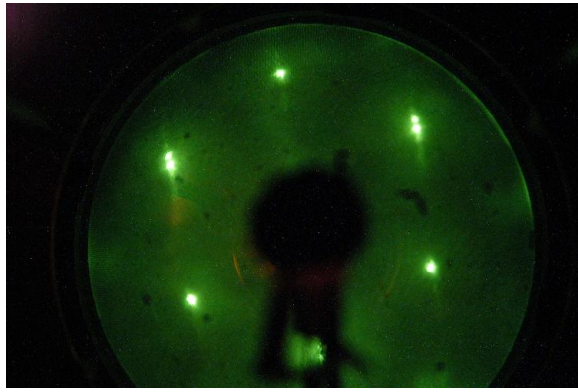


Fig. 3.3: LEED pattern of a clean stepped Pt(111) surface at 80 K. It shows sharp diffraction spots. Every second spot is splitted, which is sign of the stepped surface.

In routine operation the sample was cleaned once per week with a full sputtering cycle. After every measuring day the sample was oxidized ($T=720$ K, $p_{O_2} = 5 \times 10^{-8}$ mbar) for half an hour and left covered with oxygen for the night. In the morning of the next measuring day the sample was flashed to 1100K.

3.3 Optical Setup

The optical setup of the second-harmonic diffraction pump and probe experiment is shown in Fig 3.4.

Laser pulses of 50-fs duration at 800 nm were produced by a Ti:sapphire amplifier system with 1kHz repetition rate. The original beam was separated into two parts, a weak probe beam and a strong pump beam with the help of a 5%/95% beam splitter.

The spatial overlap of the combined pump and probe beams was adjusted under observation of the sample through an UHV-viewport with an near IR-sensitive CCD-camera (CSB-465C, Pacific Corp.) equipped with a large-working distance macro

objective (Macro Video Zoom Lense, 18-108 F/2.5, OPTEM). The temporal overlap of the two pump beams was set when the two pump beams were both p polarized. The temporal and spatial overlap of the two beams can be controlled by the observation of interference fringes.

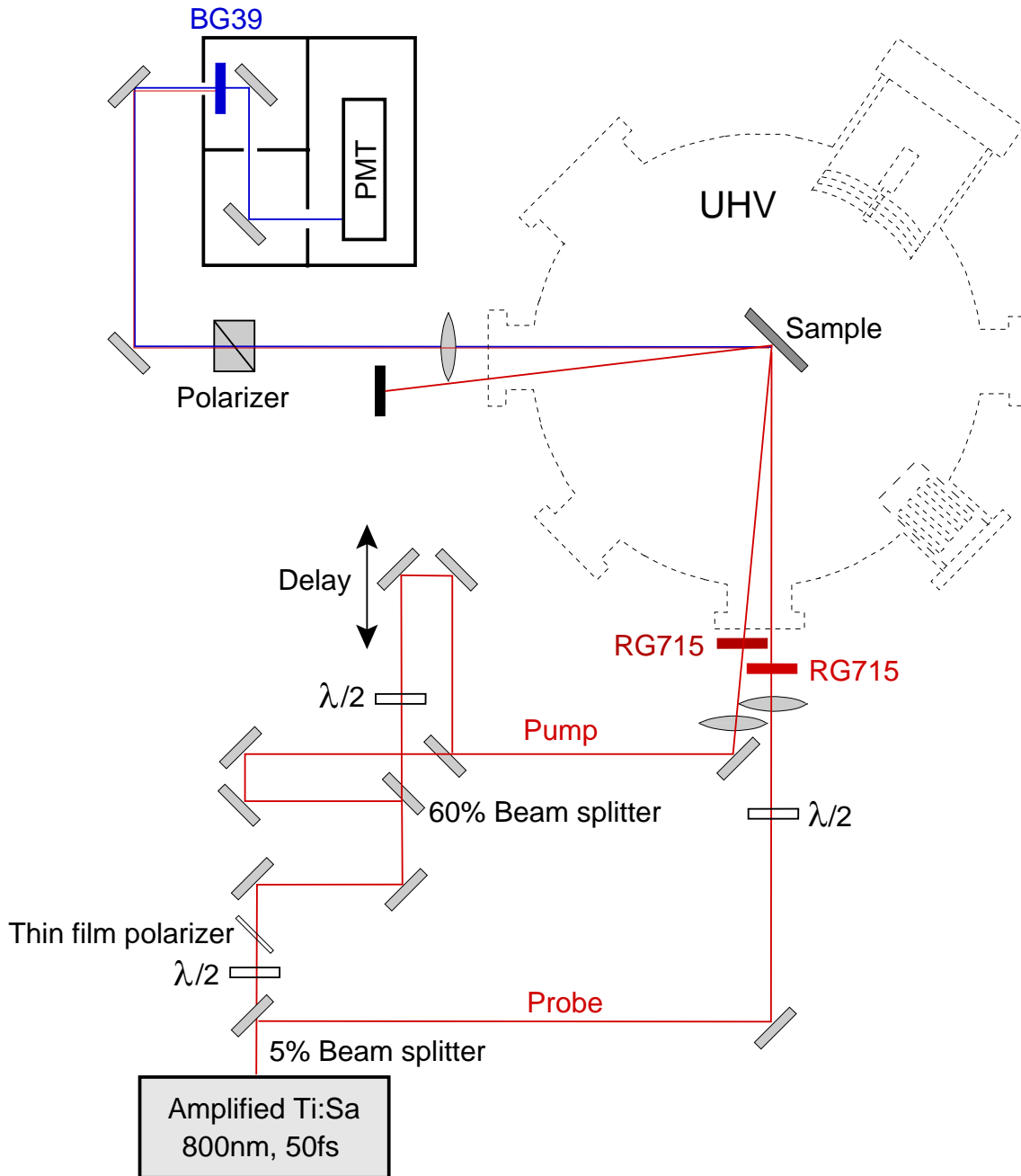


Fig. 3.4: Schematic representation of the optical setup for the second-harmonic diffraction experiment.

Probe Beam

The weak p-polarized probe beam was focused on the sample at an angle of incidence of 45° by a $f=250$ mm fused silica lens down to $90\ \mu\text{m}$ in diameter resulting in an absorbed fluence of about $0.5\ \text{mJ}/\text{cm}^2$. The polarization of the reflected second-harmonic (SH) light was analyzed by a Glan-Taylor prism. The p-polarized SH radiation was separated from the reflected fundamental beam by a combination of 400-nm dielectric bending-mirrors and a Schott BG39 color filter. A photomultiplier (Hamamatsu R4220) was combined with a 300 MHz Preamplifier (Stanford Research System, SR 445A) and with a boxcar averager (Stanford Research System, SR200) for detection.

Pump Beam

The p-polarized pump beam was incident on the surface at 40° off the normal and slightly focused to produce a Gaussian spot with 0.94 mm diameter (FWHM). The intensity was varied by a combination of a half-wave plate and a thin-film polarizer and was measured by a power meter. The spot size of the beam was determined by the knife-edge method, where a razor was fixed on a linear positioning stage (Aerotech, Accudex Zeta-drive) which was moved by a motion controller (Aerotech Unidex 1).

For two-pulse correlation measurements, the pump beam was split into two beams with the help of a Michelson interferometer. The two beams were orthogonally polarized using a zero order half-wave plate in one arm of the interferometer. The intensity of the two pump beams were chosen in a way that the adsorbed fluence of the s and p polarized beams on the platinum sample were nearly equal.

Between the two "splitted" pump pulses a variable time delay could be set: the length of one arm of the interferometer can be changed with two mirrors fixed on a linear positioning stage (Aerotech, Accudex Zeta-drive). The stage was driven by a motion controller (also Aerotech Unidex 1). Behind the interferometer the two pump beams were combined collinearly.

A Schott RG715 filter was used to block possible contributions at short wavelengths in order to exclude any direct induced photoreactions, which were observed for molecular oxygen [81]. The absorbed fluence was calculated using the optical constants of platinum [82] and assuming a constant absorption, which has been verified by Her *et al.* [12] for absorbed fluences up to several mJ/cm^2 . We estimate that the absolute values of our fluence data are accurate within 30%. Relative changes of the fluence can be determined better than 2%.

Chapter 4

Characterization of O₂ Adsorption

The detailed characterization of the applied system is very important to understand and model the measurements. The aim of this chapter is to present our measurements which were used to analyze the adsorption of oxygen on our stepped platinum sample. In the first two sections we discuss our TPD and LEED measurements. These are the typical techniques to characterize adsorption on metal and semiconductor surfaces. In Sect. 4.3 we demonstrate how SHG can be used to interpret the adsorption of oxygen. In Sect. 4.3 and Sect. 4.5 we show how the step sensitivity of the SHG signal can be maximized by using different polarization combination.

4.1 Temperature Programmed Desorption

Molecular oxygen can chemisorb directly as a molecule on a Pt(111) surface or it can dissociate and form strongly bound atomic oxygen. These two species can be distinguished by temperature programmed desorption (TPD) due to their difference in binding energy.

Technically, the TPDs were recorded in this work in two steps. For temperatures up to 300 K the sample was heated by radiation of a tungsten spiral placed behind the sample (see sect. 3.1). In this way the sample temperature could be continuously increased from 80 K to 300 K, with a heating rate of 1.7 K/s.

For temperatures above 300 K the sample was heated by electron-beam heating applying 300 V between filament and sample. In this second step the sample temperature was continuously increased from 140 K to 1050 K with a heating rate of 5.8 K/s.

Figure 4.1 shows a series of combined TPD spectra for different coverages of oxygen dosed at a sample temperature of 80 K. Note the different scaling for the low and high temperature regime. At low temperatures two peaks can be resolved. They can both be assigned to the desorption of molecularly adsorbed oxygen. Around 140 K the direct desorption of molecular oxygen from terrace sites can be observed, which are

not saturated even at the highest coverage used here. At a temperature of about 220 K direct desorption of a small amount of step-bound molecular oxygen can be observed [68, 75, 76].

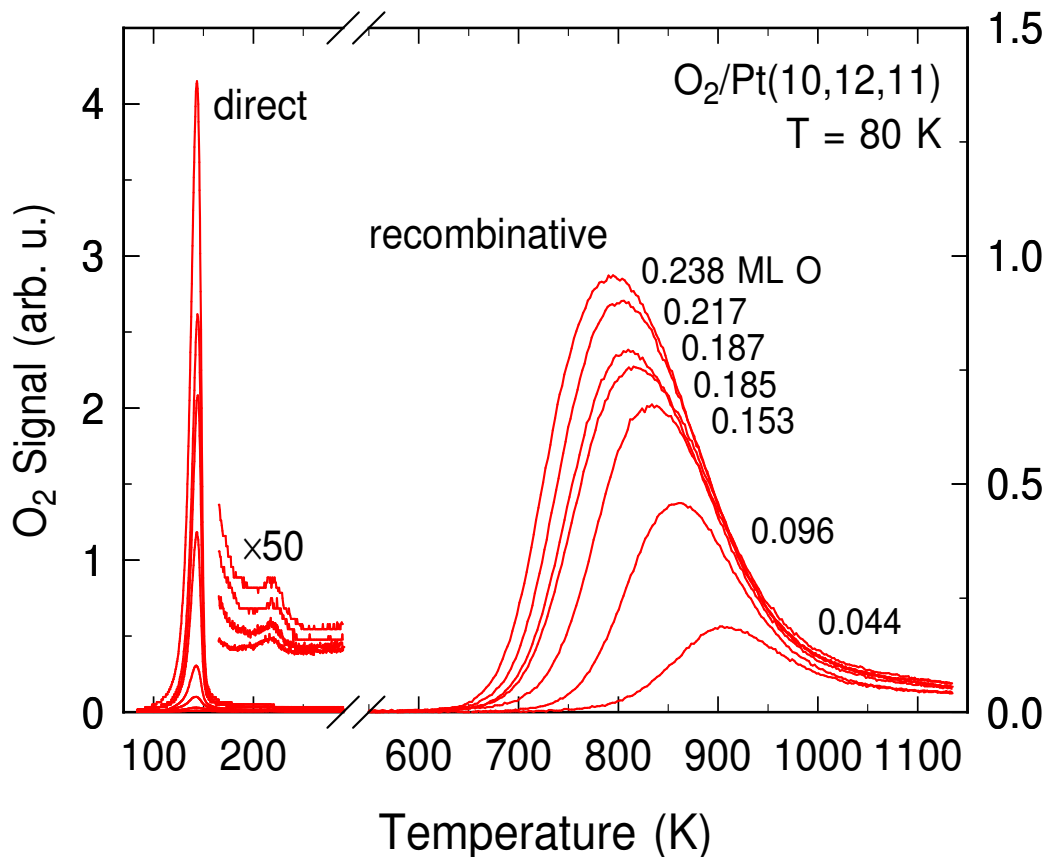


Fig. 4.1: Thermal desorption spectra of O_2 from the Pt(10,12,11) surface for different oxygen coverages dosed at 80 K. Note the different scaling for the low and high temperature regime.

The broad maxima around 800 K correspond to the recombinative desorption of atomic oxygen. Here, no distinct signal for terrace- and step-bound species can be observed due to the large peak width and the small step densities compared to crystals with a larger miscut [68,69,76]. For an adsorption temperature of 80 K atomic oxygen can descend from molecules which adsorbed dissociatively at step edges or from molecules which dissociated due to the temperature rise during recording of the TPD spectra. A pronounced shift of the desorption peak to lower temperatures can be observed with increasing oxygen coverages (see Fig. 4.1) due to the second-order desorption kinetics [76]. For an adsorption temperature $T > 150$ K molecular oxygen is not stable on the surface, and the TPD spectra show only recombinative desorption of atomic oxygen which was dissociated during adsorption. Here, a more than four times higher dosage is required to reach the saturation coverage.

4.2 Step sensitivity of the SHG

This section demonstrates how the adsorption of oxygen on a stepped platinum sample was detected with the SHG technique and points at the high sensitivity of the SH signal on step contribution.

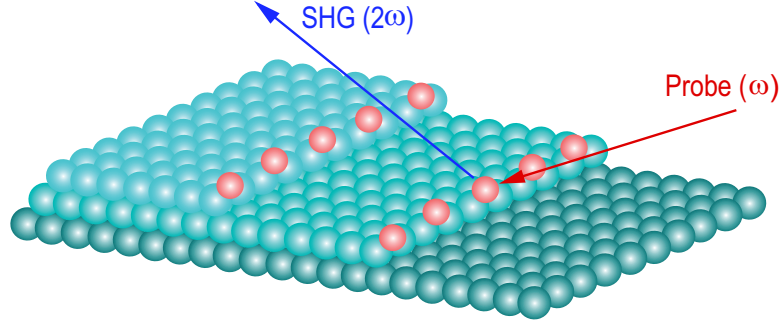


Fig. 4.2: Scheme of the experiment: step sites are decorated selectively by dissociative adsorption. The adsorption of the oxygen on the step sites is monitored by second-harmonic generation of a probe beam.

The idea of the SHG measurement is displayed on Fig. 4.2. The initial oxygen distribution has been prepared by saturating selectively the step edges with atomic oxygen. This has been done by adsorbing molecular oxygen at a substrate temperature of $T > 160$ K as it was discussed in the previous section. The saturation of the step sites was followed by the SH signal, which is generated at the step sites. The optical setup is described in Fig. 3.4.

4.3 Polarization Dependence

Polarization dependent measurements have been done to optimize the optical setup with respect to maximum step sensitivity. During these measurements the polarization of the incident probe beam was changed (5° steps), while the intensity of the generated SH radiation was detected for P and S polarization.

The polarization dependence of the second-harmonic generation yield shows a characteristic curve shape (see Fig. 4.3). The non-vanishing elements of $\chi^{(2)}$ and the Fresnel factors contributing to SHG (Sect. 2.2.1) are determined by sample symmetry and the polarization of the fundamental and second-harmonic light. The tensor components of $\chi^{(2)}$ that contribute to the SHG on the most common surfaces for different polarization combinations were discussed in section 2.2.1.

Fig. 4.3 shows polar plots of the second harmonic intensity (distance to the center) as a function of the input polarization for vicinal (111) surfaces and different detected

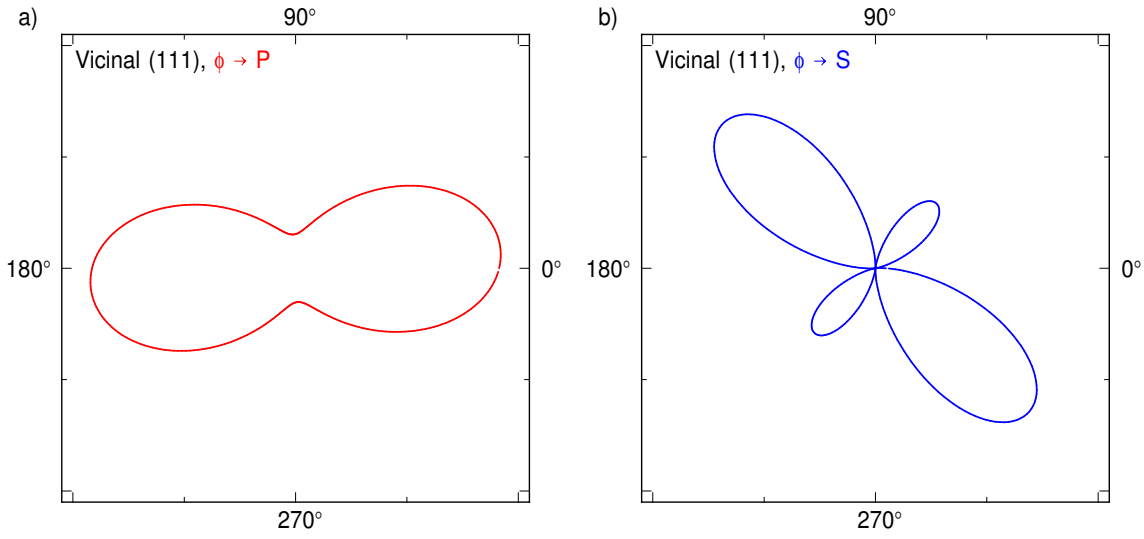


Fig. 4.3: Polarization dependence of the SHG from a clean stepped (111) surface, based just on symmetry considerations. The nonlinear susceptibilities assumed here shown in Eq. 4.1 and 4.2, and Fig.4.2 shows the definition of the angle.

polarizations.

For this figure and the following simulations (Fig. 4.3) the nonlinear susceptibilities $\chi^{(2)}$ have been chosen as:

$$\chi_{terrace,(111)}^{(2)} = \begin{pmatrix} 1 & -1 & 0 & 0 & 0.3 & 0 \\ 0 & 0 & 0 & 0.3 & 0 & -1 \\ 0.3 & 0.3 & 10 & 0 & 0 & 0 \end{pmatrix} \quad (4.1)$$

$$\chi_{step}^{(2)} = \begin{pmatrix} 0 & 0 & 0 & 0 & 0.2 & 0.2 \\ 0.2 & 0.2 & 0.2 & 0.2 & 0 & 0 \\ 0.2 & 0.2 & 0.2 & 0.2 & 0 & 0 \end{pmatrix} \quad (4.2)$$

As in the simulations shown in chapter 2, a rule of thumb has been applied for the choice of the magnitude of the tensor elements of $\chi_{terrace}^{(2)}$ as before (see Sect. 2.2.1). The tensor elements of $\chi_{step}^{(2)}$ were chosen in a way that they fulfill the conditions required due to the symmetry of the surface and that the simulation agrees qualitatively with the experimental data obtained with our sample (shown in Fig. 4.4). Note that the p-polarized response is approximately one order of magnitude stronger than the s-polarized one. This is caused by different anharmonicities in the electron motion in and out of the surface plane.

From the form of the $\chi^{(2)}$ tensor in Eq. 2.16 and in Eq. 2.25 we would expect

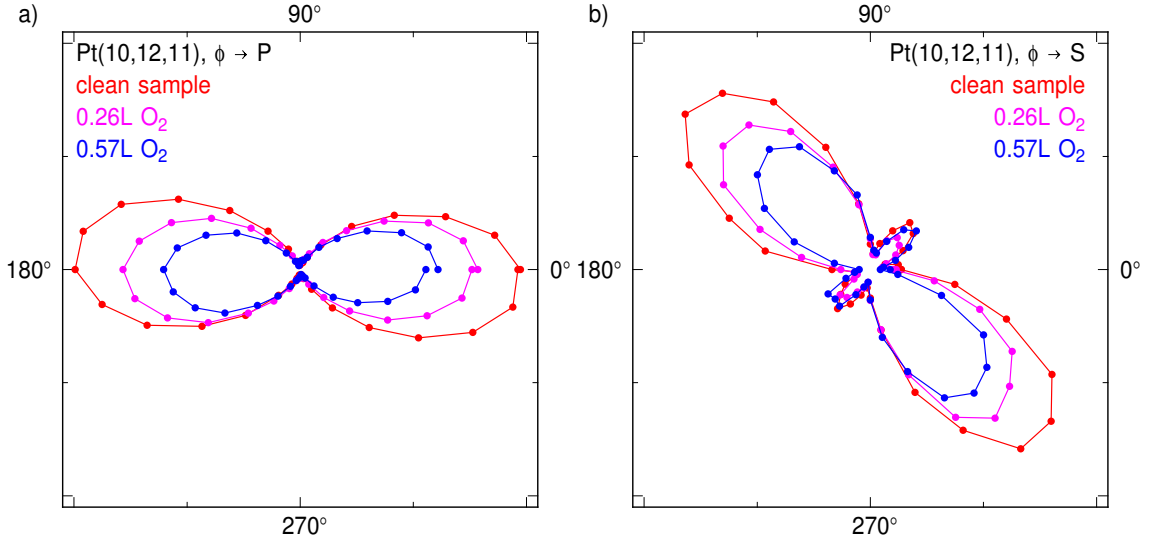


Fig. 4.4: Polarization dependence of the second harmonic generated at the clean sample and after dosage of 0,26 and 0,57 L oxygen. The polarization of the detection is P in plot a) and S in b), while the input polarization is changed ($\Phi=180^\circ$ stands for p-polarized light) in both graphs.

the highest step sensitivity for the s \rightarrow S (s-polarized fundamental and analyzing S-polarized second-harmonic) polarization combination. However, varying the polarization of the fundamental and the analyzer for the second-harmonic we have found that the polarization combination p \rightarrow P (p-polarized fundamental and analyzing P-polarized second-harmonic) gives the highest sensitivity to oxygen absorption in our case. With the step edges parallel to the plane of incidence (Fig. 2.4) we are sensitive to the contributions perpendicular to the step edges to the nonlinear susceptibility. They dominate the total yield when the threefold rotational response of the in-plane components of the (111)-terraces has its minimum.

SHG Dependence on the Azimuthal Angle

The variation of the second-harmonic intensity when the sample is rotated around its surface normal is governed by the symmetry of the crystal and its surface [83,67]. In our optical and vacuum setup it is not possible to carry out a full study of the SH intensity as function of the azimuthal angle. The sample is fixed on the manipulator and therefore cannot be easily rotated without opening the vacuum chamber.

In the present work we show the intensity dependence only for two measurements where the incidence of the probe beam was changed with 180° which coincides with a rotation of the sample with 180° (Fig. 4.5).

These measurements show that the SH signal is significantly stronger at the angle of incidence $\Phi = 0$ than at $\Phi = 180^\circ$. But at the same time it is much less sensitive

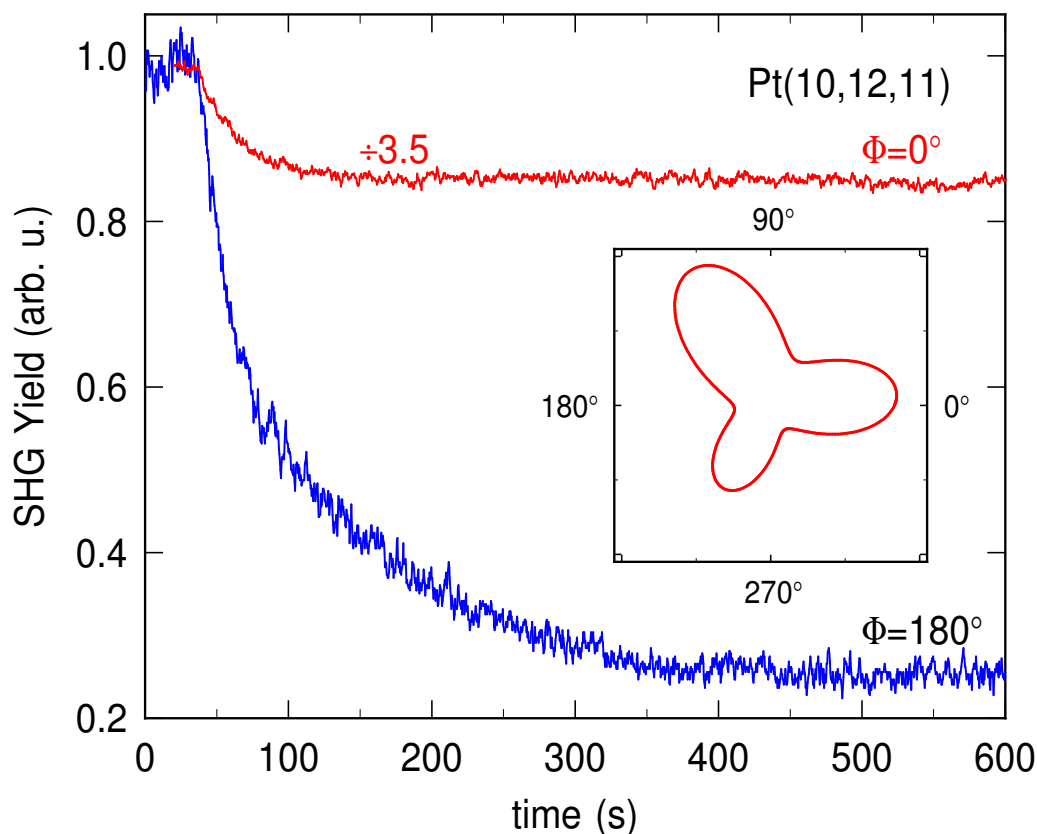


Fig. 4.5: The second-harmonic signal dependence on the azimuthal angle. These two curves show the change of the SH intensity during dosage with oxygen at the azimuthal angles 0° and 180° . Although the SH intensity at $\Phi=0^\circ$ is 3,5 times larger than at $\Phi=180^\circ$, the step sensitivity (contrast) is much stronger in the second case. The inset shows the model calculation of the azimuthal dependence of the SH-signal for a vicinal (111) surface with polarization combination $p \Rightarrow P$. Eq. 4.1 and 4.2 show the assumed nonlinear susceptibilities for this simulation.

to the step contribution, and the relative change of the SH signal is much smaller during the decoration of the step edges with oxygen. This behavior is expected from the model-calculation that can be seen in the inset of Fig. 4.5, where the amplitude of the SH-signal was calculated for an azimuthal rotation of the crystal. In this inset the polarization combination $p \rightarrow P$ is represented. From the threefold symmetry it is expected that the SH-signal is the strongest if the incident laser beam comes from $\Phi = 0^\circ$ and the weakest for $\Phi = 180^\circ$, which is in agreement with SH measurements shown here.

4.4 Step Selectivity of the SH Detection

For low adsorption temperatures ($T < 160$ K) molecular oxygen sticks not only on the steps but also on the terraces, where it partly dissociates when the temperature is increased. In order to verify that SHG selectively probes the oxygen coverage at the step edges in our geometry, we have measured the SH signal *in-situ* during the coverage for two different adsorption temperatures (80 K and 160 K respectively). The same was done in the LEED measurements presented on the next page (Sect. 4.4.1). The result is shown in Fig 4.6.

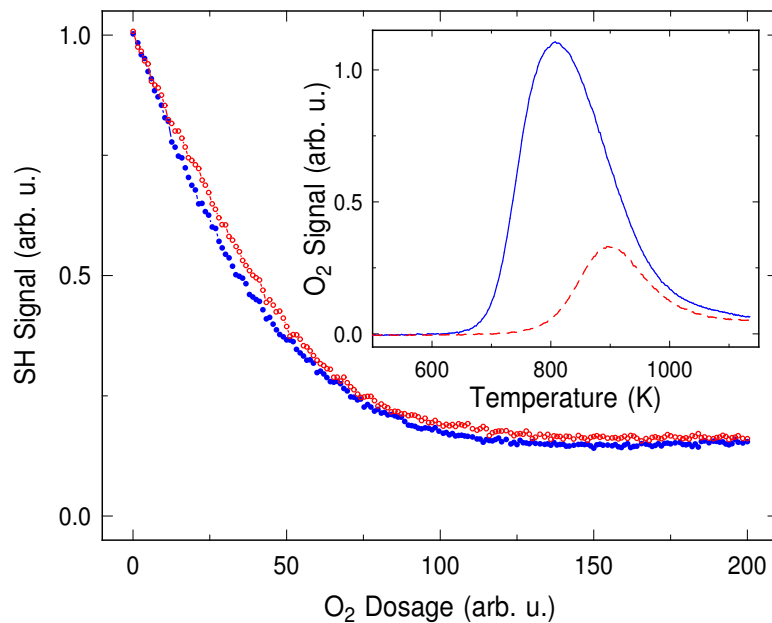


Fig. 4.6: Second harmonic signal as a function of oxygen dosage at a sample temperature of 80 K (closed symbols) and 160 K (open symbols) up to the same maximum dosage. The inset shows the corresponding TPD spectra for 80 K (solid line) and 160 K (dashed line) of the adsorbed atomic oxygen detected after recombinative desorption. The TPD spectrum taken at 80 K is already saturated.

The same monotonous decrease of the SH-signal followed by a saturation can be observed in both cases in contrast to the total oxygen coverage which is different by a factor of four, as can be seen in the inset which shows the corresponding TPD spectra. The higher amount of oxygen at 80 K dosing temperature can be easily understood at this temperature oxygen adsorbs not only on the step edges but on the terraces (see Sect. 4.4.1). If the sample is exposed at 160 K temperature the oxygen adsorbs only at the step edges and with that the total amount of the adsorbed oxygen is much lower.

Flashing the sample to 300 K and cooling back to 80 K does not change the SH-signal in both cases. For 80 K adsorption temperature, a $p(2 \times 2)$ oxygen over-structure as has been observed by LEED (see Fig 4.7), which points to oxygen on the terraces.

The remarkable equality of progression and saturation level of the SH-signal independent of sample temperatures and of annealing shows clearly that in our geometry SHG is exclusively sensitive on the dissociative adsorption of oxygen at the step edges. The strong decrease of the SH-signal with oxygen coverage demonstrates the high sensitivity of the SHG detection even for a low step density (< 0.09 ML).

4.4.1 LEED Patterns of the Dosed Platinum Surfaces

For the diffusion measurements we would like to selectively decorate the step edges of the platinum sample with oxygen atoms as starting point. It is known from earlier studies that both molecular precursor-mediated or quasi-direct dissociation can be observed, depending on the initial conditions [70].

After dosing the sample at two different substrate temperatures at 80 K and 160 K with the same amount of oxygen and annealing it at 300 K two different LEED patterns can be observed (see Fig. 4.7).

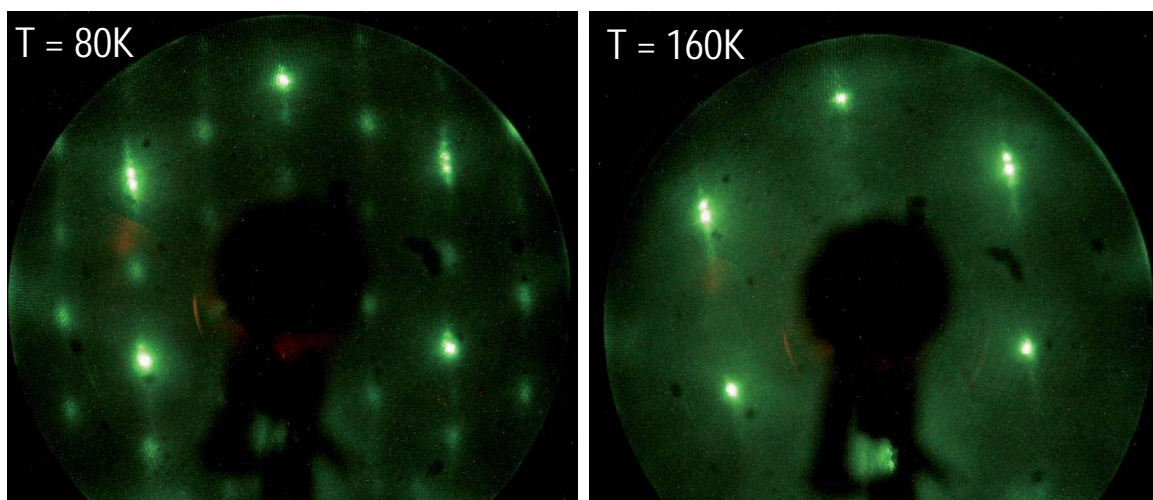


Fig. 4.7: LEED patterns of the oxygen saturated stepped Pt(111) surface for different adsorption temperatures. If the sample was exposed to oxygen at 80 K (left side), after annealing the sample at 300 K the $p(2 \times 2)$ over-layer structure can be seen which is a clear sign of oxygen atoms on the terraces. If the exposure took place at 160K (right side), this over-structure cannot be observed because no oxygen atoms are on the terraces, all are adsorbed on the step sites.

At a dosing temperature of 80 K molecular oxygen adsorbs on the whole surface

and some part of it dissociates to atoms along the steps. After annealing the sample to 300 K all of the oxygen molecules dissociate and some part desorb. Because the atomic oxygen is mobile above 150 K they are arranging to the well know $p(2 \times 2)$ superstructure on the terraces (see left side of Fig. 4.7).

At 160 K dosing temperature molecular oxygen is not stable on the surface. The molecules directly dissociate to oxygen atoms preferentially at the step edges [77]. If the amount of dosed oxygen is not beyond the possible free step sites, we can decorate selectively the step sites without having atomic oxygen on the terraces. This situation can be seen on the right side of the Fig. 4.7. The atomic oxygen is "sitting" stable at the step edges, and because there is no oxygen on the terraces no over-structure pattern can be observed on the LEED picture.

4.5 Frequency Domain SHG Interferometry

In order to relate the second-harmonic signal to the step coverage we can express the nonlinear susceptibility in first approximation as a sum of a coverage-dependent step contribution $\chi_s^{(2)}$ proportional to the relative number of free step sites $(1 - \theta_s)$ and a coverage independent (or only weakly coverage-dependent) background $\chi_{bg}^{(2)}$ [84]. This includes a remaining response of the terraces and possible bulk quadrupole contributions.

$$\chi^{(2)}(\theta_s) = \chi_s^{(2)}(1 - \theta_s) + \chi_{bg}^{(2)} \quad (4.3)$$

The detected second-harmonic intensity $I(2\omega)$ is proportional to the square of the induced nonlinear polarization and thus to the square of the nonlinear susceptibility, which is in general a complex quantity. If there is no phase shift between $\chi_s^{(2)}$ and $\chi_{bg}^{(2)}$, the relative step coverage θ_s for the whole coverage range can be extracted simply by taking the square-root of the measured SH-signal and by applying Eq. (4.3) with real quantities $\chi_s^{(2)}$ and $\chi_{bg}^{(2)}$, measuring the total phase of the generated SH field as a function of oxygen coverages.

In most of the surface SHG experiments only the intensity of the generated harmonic field is measured, although the phase of the SH contains often valuable information which is directly related to the phase of the components of the surface second-order susceptibility $\chi^{(2)}$.

The phase of the SH field can be measured by an interference technique which was introduced by Chang et al. [85]. They used a linear polarized laser beam to generate SH radiation in a crystal and in a reference plate that were placed in an evacuated box. Both fields interfered and the intensity of the total field was recorded. By venting the box with air, the dispersion of the air changed the relative phases between the

fundamental and second harmonic field, leading to oscillations in the detected second harmonic intensity. This enabled them to quantify the phase shift.

Since this method bases on the direct interference of the two nonlinear fields, it is not compatible with UHV experiment if ultrashort laser pulses are used: the dispersion of typical optical viewports in UHV chambers leads to a large time delay (typ. 1 ps) between fundamental and SH pulses which destroys the interference.

Instead of compensating this delay in a complicated optical setup, Veenstra *et al.* [86] developed another approach and used the time delay to obtain the phase information from the spectrum of the generated second-harmonic light.

A sketch of the experimental setup used in the present work is shown in Fig. 4.8. The explanation of the technique presented in the following lines follows the argumentation given by Veenstra *et al.* [86] and shows that it is specially suitable to detect possible phase shifts as for example during our oxygen adsorption process.

When a SH (2ω) and a fundamental (ω) pulse (described by their amplitudes E_{SH} and E_f) propagate through air, the relative phase Φ between E_{SH} and E_f^2 gradually changes:

$$\Phi(d) = \Phi_0 + \delta\Phi = \Phi_0 + \frac{4\pi\Delta n_{air}}{\lambda}d. \quad (4.4)$$

$\Delta n_{air} = n(2\omega) - n(\omega) \sim 10^{-5}$ is the dispersion of the ambient air, d is the distance that the two pulses travel through air, and λ is the wavelength of the fundamental pulse. By using an additional SHG source (reference) at position d in the path of the beam, interference can be observed in the detected total SH signal

$$I_{2\omega,tot}(d) = I_{2\omega,s} + I_{2\omega,r} + 2\alpha\sqrt{I_{2\omega,s}I_{2\omega,r}}\cos[\delta\Phi(d) + \Phi_0], \quad (4.5)$$

where $I_{2\omega,s}$ and $I_{2\omega,r}$ are the SH signals generated by the sample and the reference, respectively. The spatial coherence is described by the coherence parameter α . If the reference SH pulse and the SH pulse generated at the sample do not overlap in time, this interference disappears. As we already mentioned, this is the case in our experiments where the optical viewport of our chamber introduces a delay that exceeds the pulse durations by far.

In the time domain, the optical field at the detector of two SH pulses with delay τ can be described by the function

$$E_{SH}(t) = E_1g(t)e^{-i2\omega_0t} + E_2g(t - \tau)e^{-i2\omega_0t+i\Phi} + c.c., \quad (4.6)$$

where $E_i g(t)$ is a slowly varying envelope with amplitude E_i ($i=1,2$). The fast oscillating part of the pulses and their relative phase Φ are contained in the exponentials. From this, the spectrum measured with the detector can be calculated by Fourier

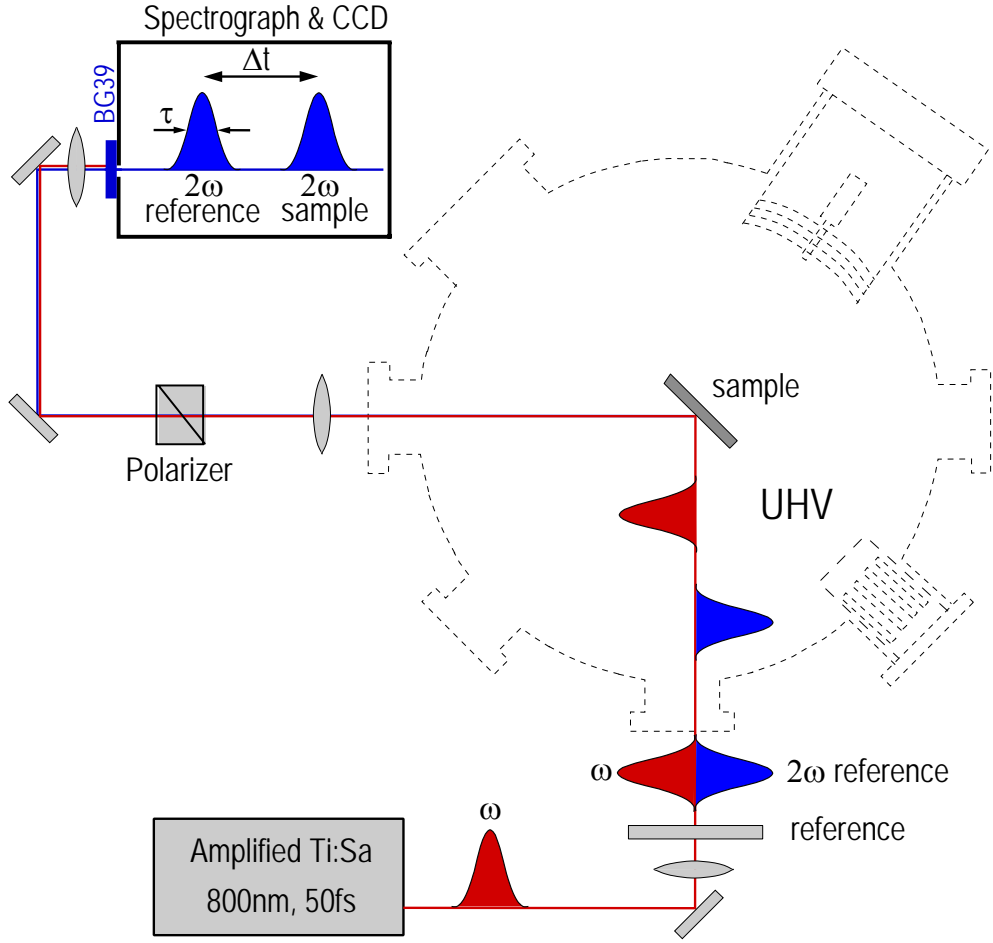


Fig. 4.8: Principal scheme of the frequency-domain interferometry to determine the phase shift as a function of oxygen coverages. The phase of the modulations, depending on the relative phase between sample and reference pulses, can then be measured with a monochromator without the need of moving optical elements [87].

transformation of Eq. 4.6 [86]:

$$I(2\omega_0 + \Omega) \propto |G(\Omega)|^2 [E_1^2 + E_2^2 + 2\alpha E_1 E_2 \cos(2\omega_0\tau + \Omega\tau + \Phi)], \quad (4.7)$$

Ω denotes the deviation of the frequency from the central frequency $2\omega_0$ within the spectrum of the SH pulse. The first term in the cosine, $2\omega_0\tau$, is a fixed number whereas the second, $\Omega\tau$, leads to beating with a period 2π in the spectrum of the SH light. The phase of the beatings is directly related to the phase Φ of the response from the sample. Therefore phase shifts in the nonlinear susceptibility of our sample (for instance during oxygen adsorption) would lead to phase shifts of the beatings.

The upper part of Fig. 4.9 shows such a spectrum measured at our clean Pt(111)

sample.

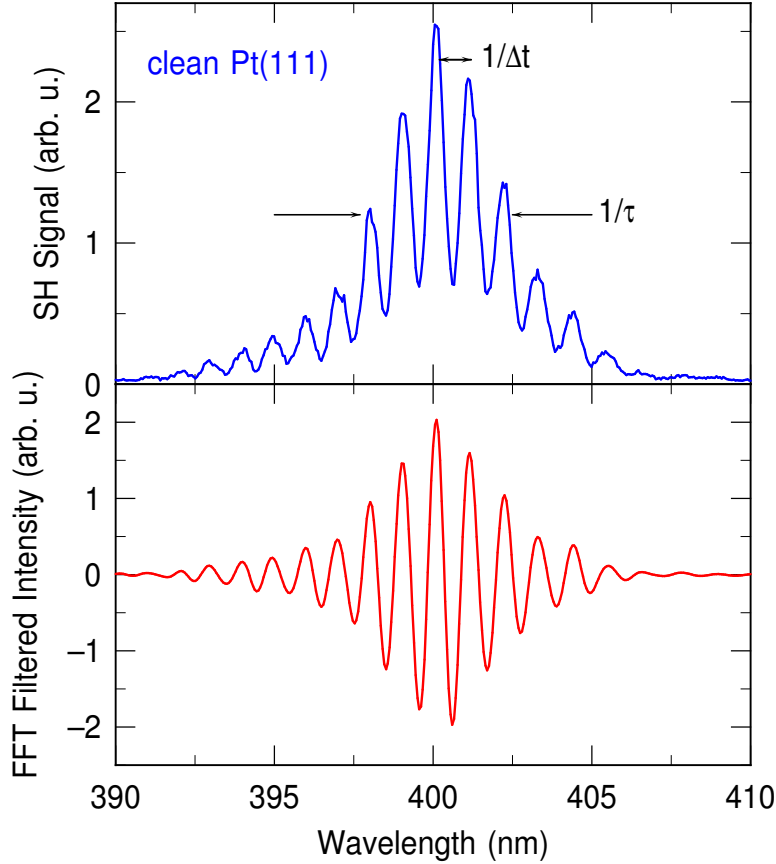


Fig. 4.9: Illustration of the Fourier filtering for an interferogram recorded with $p \rightarrow P$ polarization at the clean Pt(111) sample. The upper plot shows a typical interference pattern in the frequency domain where the temporal separation Δt gives rise to a modulation frequency $1/\Delta t$ spread over a spectral range of $1/\tau$. The lower plot shows the Fourier filtered interferogram.

The measurements were carried out by using a z-cut quartz crystal, with a thickness of $240 \mu\text{m}$ as reference. It was placed between the focusing lens and the UHV window outside the UHV chamber (see Fig. 4.8). The SH pulses which were generated on the sample and the reference are separated through their group velocities after passing the fused silica window. To analyze the interference pattern caused by the separation of the pulses we used a dual grating spectrograph (MS260iTM, Thermo Oriel), combined with a CCD camera (iStar 720, Andor). The resolution of the spectrometer is 0.15 nm , the sampling time was 0.75 s .

To optimize the interference pattern it was possible to rotate the quartz crystal about its surface normal to vary the intensity of the reference SH.

First, the Fourier transformed $f(t)$ of the shifted SH spectrum $F(\Omega) = I(2\omega_0 + \Omega)$

is calculated, where $2\omega_0$ is a certain frequency close to the center of the spectrum. $f(t)$ is proportional to the autocorrelation function

$$f(t) \propto \int_{-\infty}^{+\infty} \varepsilon(t') \varepsilon^*(t' - t) dt' \quad (4.8)$$

of the overall envelop $\varepsilon(t) = E_1 g(t) + E_2 g(t - \tau) e^{i\Phi}$ at the entrance of the spectrometer. The autocorrelation function Eq. 4.8 possesses a central peak close to $t=0$ and two satellites at $t = \pm\tau$. These satellites contain the information on the oscillatory part in the raw data. An inverse Fourier transform is then exclusively applied to those parts of the autocorrelation function that contain the two satellites. The result of this Fourier filtering is shown in the lower part of Fig. 4.9 and enables us to determine the relative phase Φ , which is defined as the phase of the oscillating, Fourier filtered part relative at $2\omega_0$ [86].

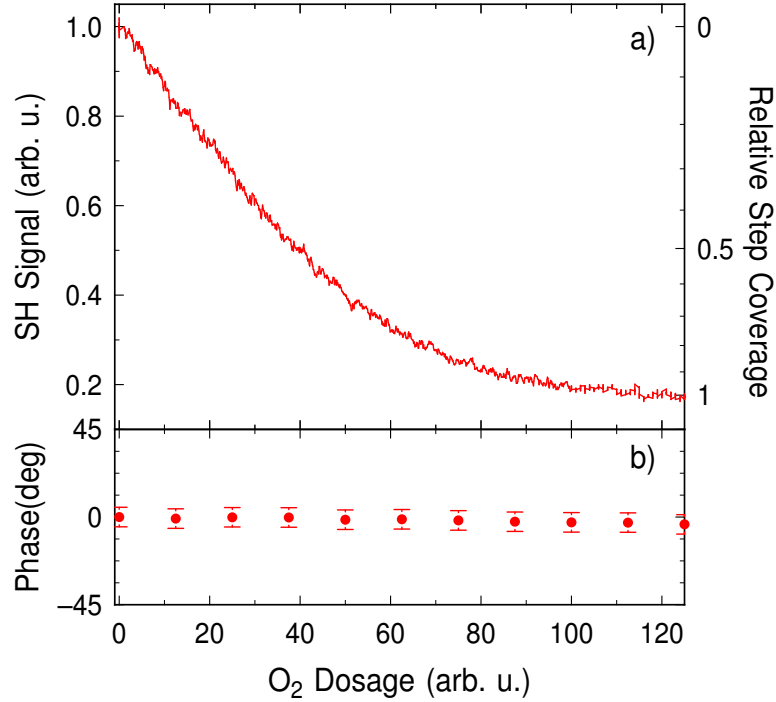


Fig. 4.10: a) SH intensity as a function of oxygen dosage. b) Extracted phase of the total SH field for various oxygen coverages. Since the phase is stable during adsorption, the relative step coverage can be extracted in a straight-forward way (see Eq.4.3).

These phase measurement were done at several oxygen coverages (Fig. 4.10). Part b) shows that there is no phase shift of the SH intensity as a function of oxygen dosage in our case (see Fig. 4.10). Since the nonlinear susceptibility is

$$\chi^{(2)} = |\chi^{(2)}| e^{i\Phi}, \quad (4.9)$$

where Φ is the phase, this allows us to extract the relative step coverage θ_s for the whole coverage range simply by taking the square-root of the measured SH-signal and applying Eq. 4.3 with real quantities $\chi_s^{(2)}$ and $\chi_{bg}^{(2)}$. The right axis of the upper plot on Fig. 4.10 shows these coverages.

Chapter 5

Time-Resolved Detection of Surface Diffusion

This chapter presents the results of our laser-induced diffusion experiments. First, we demonstrate how diffusion can be detected using the SHG technique (section 5.1). The diffusion barrier for hopping from the step sites onto the terraces has been extracted from thermal induced diffusion measurements (see Sect. 5.2). In the case of electronically mediated processes the hopping-rate per laser pulse is independent of the average thermal heating of our system by the laser beam. Applying different repetition rates of the pump laser beam the thermal mediated process can be ruled out (see Sect. 5.3). A modified rate-equation model has been developed for the extraction of step-terrace hopping-rates, which is discussed in Sect. 5.4. The strong nonlinear dependence of the hopping rate on the laser fluence of the pump beam (see Sect. 5.5) makes it possible to perform two-pulse correlation measurements (Sect. 5.6), which carry information about the energy transfer dynamics from the optical excitation to the diffusive motion.

5.1 Observation of Laser-Induced Diffusion

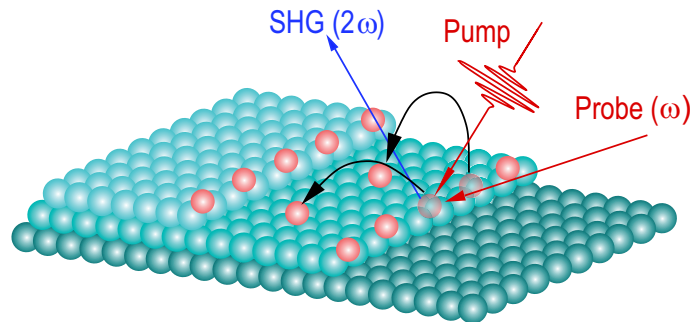


Fig. 5.1: Scheme of the experiment. Step sites are decorated selectively by dissociative adsorption. Intensive ultrashort laser pulses induce diffusion onto the terraces, which is monitored by second-harmonic generation of a probe beam.

The idea of the measurement is depicted in Fig. 5.1. First, the step edges were decorated with atomic oxygen by adsorbing oxygen at 160 K as it was already discussed in Sect. 4.3. This results in a monotonous decrease of the SH signal with the decreasing number of free step sites until all step sites are filled with oxygen (“dosing” regime in Fig. 5.2).

Following the saturation of the steps, the sample has been cooled down to 80 K in order to prevent any influence of thermal diffusion even on the terraces. When the substrate temperature has reached 80 K the pump laser beam was switched on to light on the sample (“induced diffusion” regime in Fig. 5.2). Spatial overlap of pump and probe beams was adjusted under observation of the sample through an UHV-viewport with near IR-sensitive CCD-camera equipped with a large-working-distance macro objective. Applying the pump pulses at a repetition rate of 1 kHz led to a continuous recovery of the SH-signal.

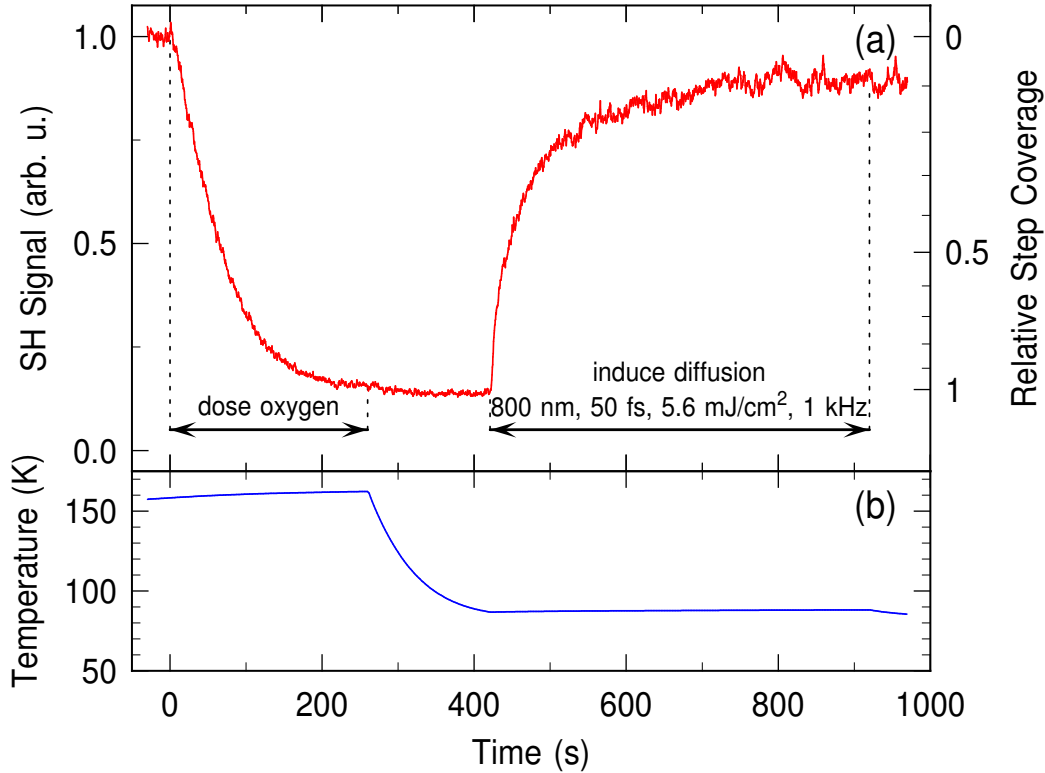


Fig. 5.2: Second harmonic signal (a) and temperature (b) as a function of time. First, oxygen is dosed at a temperature of 160 K. After cooling to 80 K, diffusion is induced by the pump laser with an absorbed fluence of 5.6 mJ/cm^2 at a repetition rate of 1 kHz. This leads to a recovery of the SH signal due to the depopulation of the step edges. The relative step coverage is calculated from Eq. 4.3.

Similar to the case of thermal diffusion [35], we assign the recovery of the SH signal

to the induced diffusion of oxygen from the steps onto the terraces where it sticks after each laser shot at a substrate temperature of 80 K. Due to the high binding energy of atomic oxygen we can exclude that direct laser-induced desorption is responsible for the depopulation of the step edges even for fluences up to the damage threshold of platinum.

Thermally, atomic oxygen desorbs recombinatively in a second-order process, thus not without preceding diffusion. Moreover, since the heat of recombinative desorption is reported to be larger than 2 eV [75, 76, 88, 89], we do not expect laser-induced desorption for fluences in the same order of magnitude that is sufficient for driving diffusion.

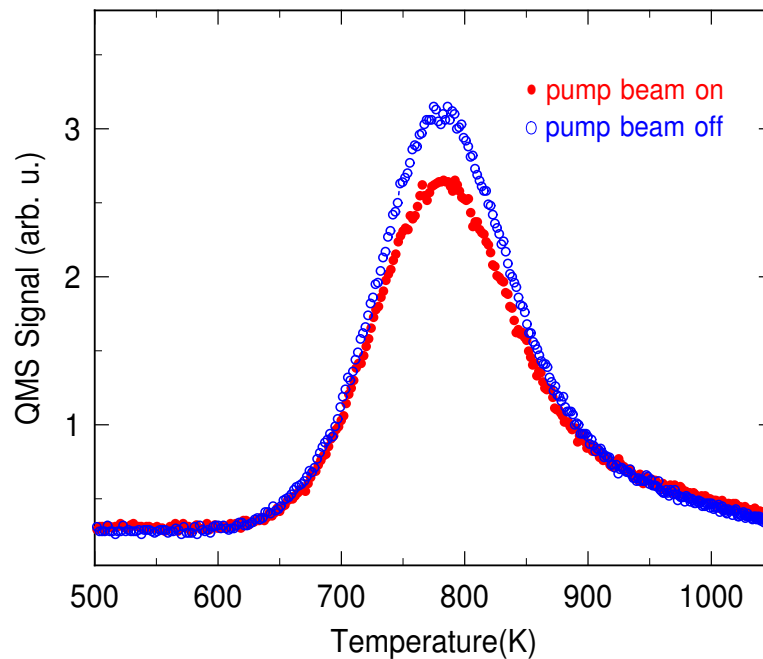


Fig. 5.3: TPD spectra after exposing the sample with oxygen at 160K. In the case of the lower curve the whole sample was scanned over with the pump beam at high fluence. In the case of the upper curve the TPD spectra was done without opening the pump beam but after waiting the exactly same time between dosage and heating.

To exclude desorption we have done two different experiments. First, we have saturated the step edges with oxygen at 160 K. In the first experiment we were slowly scanning the whole surface with the pump beam spot after saturation of the steps at a high pump fluence at 80 K. In the second experiment we simple waited the same time without shining the pump beam on the sample after saturation. In both measurements subsequent TPD spectra were recorded finally (see Fig 5.3). These TPD spectra show that the difference between the oxygen coverages after scanning the surface and without doing so is below 12%. These 12% can originate from oxygen

that is adsorbed molecularly from the remaining oxygen background pressure after dosing during the long waiting time between dosage and TPD during the second experiment (without the pump beam). If oxygen would molecularly adsorb on the surface while the pump beam is scanning the surface, it would desorb directly again.

We have demonstrated thermally induced back-diffusion after electronic diffusion from the terraces onto the step edges to rule out desorption. The initial situation (until 900 s) was the same as in the experiment discussed before (see Fig 5.4). First oxygen was dosed at 160 K and after that the sample was cooled down to 80 K. After this diffusion was induced from the step sites to the terraces with laser pulses (“laser-induced diffusion” regime in Fig. 5.4). During laser-induced diffusion the SH-signal was increasing while step sites became free. At 900 seconds the pump beam was closed and the sample was heated to 200 K (“thermal-induced backdiffusion” regime in Fig. 5.4). At this temperature the oxygen is mobile on the terraces and the diffused oxygen atoms are partly moving back to the step edges. In doing so, the SH-signal is decreasing, because more and more step sites are becoming filled again. To rule out an influence of a temperature-dependence of the SH signal, the sample was cooled down again to 80 K. If the laser beam would have desorbed oxygen from the steps, the signal would not have changed during the heating cycle.

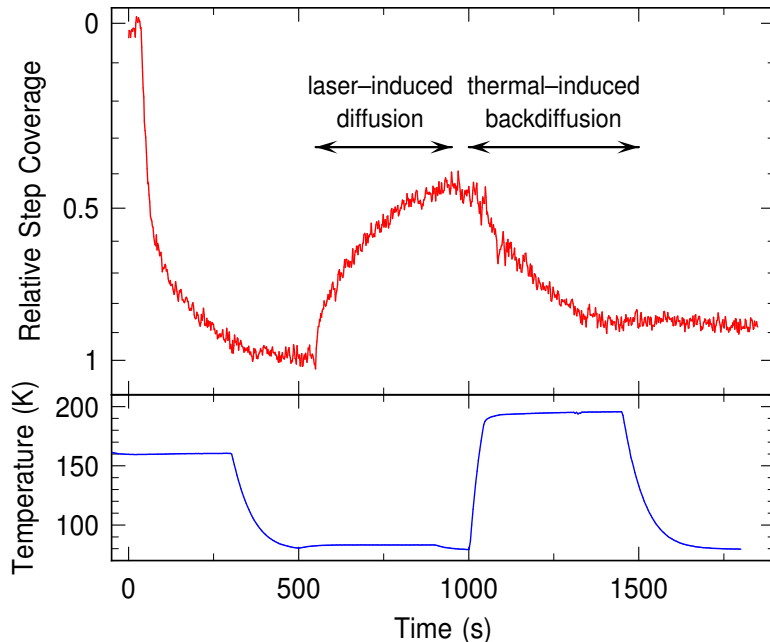


Fig. 5.4: Second harmonic signal (upper box) and temperature (lower box) as a function of time. First, oxygen is dosed at a temperature of 160 K. After cooling to 80 K, diffusion is induced by applying the pump laser. After electronic diffusion the sample is heated to 200 K and back-diffusion is thermally induced from the terraces back to the step edges.

The saturation of the SH-signal for large times below the initial value reflects the equilibrium distribution of oxygen at steps and on terraces under conditions of intense laser excitation. In thermal equilibrium, the ratio between step- and terrace-bound O atoms depends on the temperature and on the difference between the binding energy for step and terrace sites (see Eq. 5.5). At first glance one would expect a rather large energy difference since oxygen binds preferentially at the step edges even at room temperature [71, 77]. However, the decoration of the step edges is primarily due to the enhanced reactivity for dissociative adsorption at the step edges and does not require any difference in the binding energies as long as the establishment of a thermal equilibrium distribution is hindered by a large enough diffusion barrier. The situation here is very similar to N on Ru(0001) where thermal step-depletion of N after dissociative adsorption of NO has been observed around 300 K by STM [60]. The diffusion barrier has been determined to be 0.94 eV while the binding energy difference between step and terrace sites has been calculated for different sites to be in the range of only 0.03-0.25 eV [90]. First-principle calculations [71] for 2×1 super-lattices of O on Pt(211) and Pt(322) yielded a binding energy difference of 0.4-0.6 eV between step- and terrace-bound O depending on step type. This difference is expected to be considerably lower when isolated O atoms on the terraces are considered. At saturation coverage the repulsive interaction between O atoms leads to a reduction of the adsorption energy by about 20% [75, 88]. The presence of a relatively small binding energy difference between step and terrace adsorption under our experimental conditions is supported by the fact that we can populate the terraces by thermal induced diffusion for temperatures around 300 K. The consequence for the laser-induced experiments is that the steps can be depleted to a significant extent with high laser fluences by the repetitive transient excitation. As will be discussed in Sect. 6.4 under this condition the adsorbate temperature rises effectively to more than 1000 K for a couple of picoseconds.

5.2 Thermally Induced Diffusion

The barrier for diffusion on the flat Pt(111) surface has been studied with different techniques. Lewis and Gomer [91] used field emission microscopy and reported an activation energy of 1.2-1.5 eV. Wintterlin *et al.* [92] studied diffusion with scanning tunneling microscopy (STM) around 200 K and deduced a barrier of $E_a \simeq 0.43 \pm 0.04$ eV. Density functional calculations [72] found a slightly larger value of 0.58 eV, supported by a reexamination of the experimental data of Wintterlin *et al.* and other theoretical [71] and experimental [93] results.

Here we have estimated the barrier for diffusion from step sites onto the terraces by thermally-induced diffusion experiments monitored by SHG.

The preparation of the sample was similarly done as in the case of electronically induced diffusion which is described in detail earlier (see Sect. 5.1). The initially clean surface was exposed to oxygen at 160 K to prevent adsorption of oxygen on the terraces. After saturation of the step sites the sample was cooled down to 77 K where the diffusion is frozen. In the next step the surface temperature is increased rapidly within a few seconds to a value high enough to observe diffusion. In different measurements the temperature was elevated from 77 K to 263 K, 274 K, and 305 K respectively, and the diffusion was observed by the change of the SH signal (see Fig. 5.5). The continuous signal increase is due to fluent oxygen transfer from the occupied step sites to the terraces.

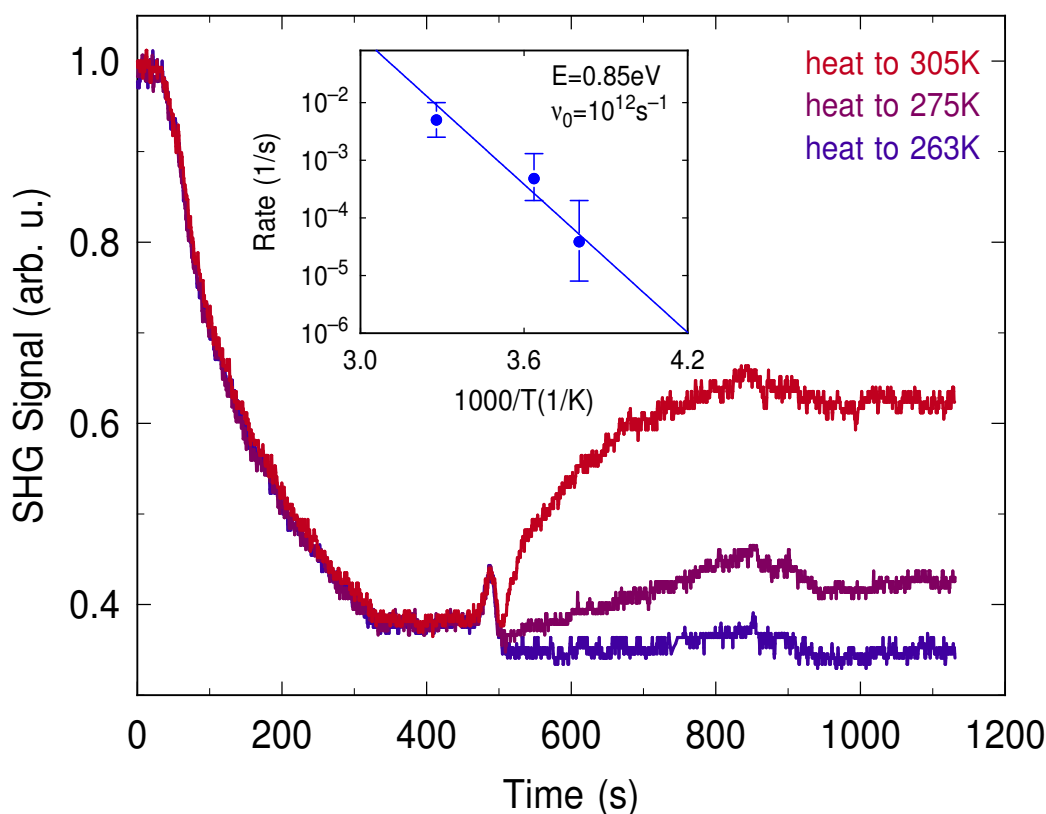


Fig. 5.5: Experimental procedure to determine the thermal diffusion of atomic oxygen from the steps onto the terrace sites of vicinal Pt(111). The plot shows the decrease of the SH signal during oxygen dosage and the recovery of the intensity during heating the sample to three different temperatures. The inset shows the Arrhenius plot which is used to derive the diffusion barrier.

The difficulty in these measurement results from two facts. On the one hand the

second harmonic signal is inherent temperature dependent, and on the other hand the optical path is misaligned due to the thermal extension of the tungsten wires clamping the sample (Fig. 3.2) when we increase the temperature of the sample by approx. 200-300 K.

After each diffusion experiment the sample was flashed to 1100 K in order to get rid of the oxygen on the surface and it was exposed with a high oxygen flux at elevated temperature to clean the surface from incidental carbon contaminations coming from the bulk due to heating it. After this oxidization the sample was once more flashed to 1100 K.

The increase of the SH intensity during the diffusion process can be related to the changes in the step and terrace coverage. To extract a diffusion rate from the measurement we used the same one-dimensional rate equation model as for the description of the electronically induced diffusion later on (Sect. 5.4).

The diffusion barrier has been estimated from these measurements by plotting the diffusion-rate in an Arrhenius plot which is shown in the inset of the Fig. 5.5. With $D = \nu_0 \exp(-E_a/kT)$ we found the activation energy to be $E_a = 0.85$ eV and a prefactor $\nu_0 = 10^{12} \text{ s}^{-1}$. If we use the frequency of the frustrated translation as prefactor $\nu_0 = 1.21 \times 10^{13} \text{ s}^{-1}$ [94] the activation energy increases to $E_a = 0.92$ eV.

5.3 Dependence of the Diffusion-Rate on the Repetition Rate of the Pump Laser

As discussed in Sect. 5.1 and in Sect. 5.2, the diffusion of oxygen from step sites onto terraces can be sensitively monitored by SHG. To distinguish between electronically and thermally induced diffusion caused by the femtosecond laser pulses we have performed measurements with the same pump laser fluences, but with different repetition rates (see Fig. 5.6). This has been realized by using a mechanical shutter which has been periodically opened and closed.

With this shutter we could block half of the laser pulses, and accordingly the thermal heat of the sample has been reduced by a factor of two. If the diffusion is thermally activated by the average heat of the pump laser, the diffusion rate has to be also strongly lowered. In the case of a hot electron mediated process the diffusion rate shall not change, only the timescale will be different.

Plotting the SH intensity as a function of the number of laser pulses (see Fig. 5.6) reveals exactly the same diffusion rate for the full and halved repetition rate. This is a clear sign that the diffusion is mediated by electrons what we will prove further in the next sections.

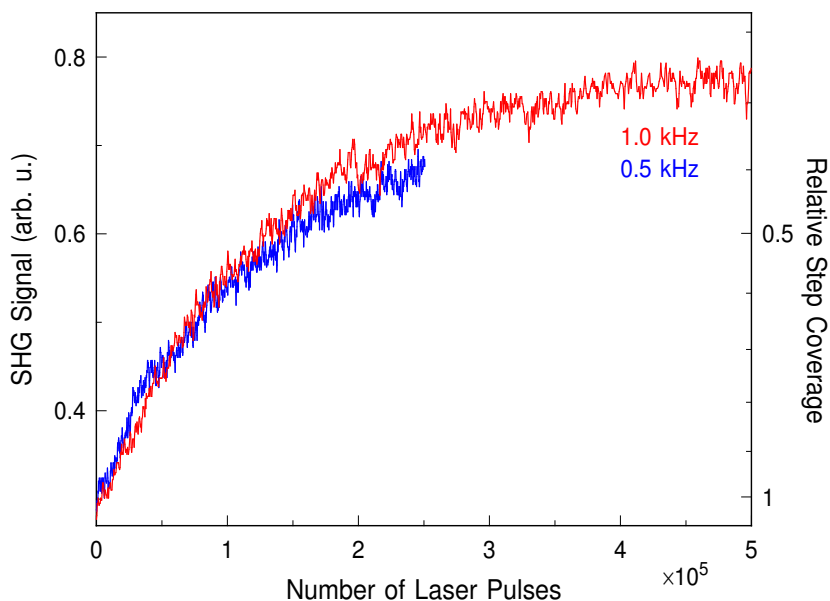


Fig. 5.6: Relative coverage of oxygen at steps which coincides with the intensity of the SH signal as a function of the number of laser shots for the same laser fluences (but with different repetition rate!)

5.4 Kinetics of Step-Terrace Diffusion

In section 4.3 it has been discussed how the change of the SH signal with irradiation by the pump laser can be converted into a change of the step coverage with irradiation time. From the initial slope of this data one can, in principle, directly extract a hopping-rate for the diffusion of oxygen from the initially saturated step sites onto the empty terraces. However, the high quality of the data allows a more detailed study of the diffusion kinetics.

For this purpose we have used a model which was motivated by two thermal induced diffusion studies. Reutt-Robey *et al.* studied a reverse procedure of CO diffusion on vicinal platinum (111). They started a random distribution of CO on the stepped surface and they monitored the thermally activated diffusion of CO from the terrace sites towards the step sites by infrared adsorption spectroscopy (IRAS) [61]. The other study was done by Raschke *et al.*, they monitored the thermally activated diffusion of H on vicinal Si(001) surface, from the step sites towards the terraces with SHG [35, 95].

Due to our initial condition (only the step sites are decorated with atomic oxygen), there is no gradient of the coverage parallel to the step edges. This restricts the macroscopic diffusion to the direction perpendicular to the step edges. Thus, we can describe macroscopic diffusion by a one-dimensional model of statistically hopping

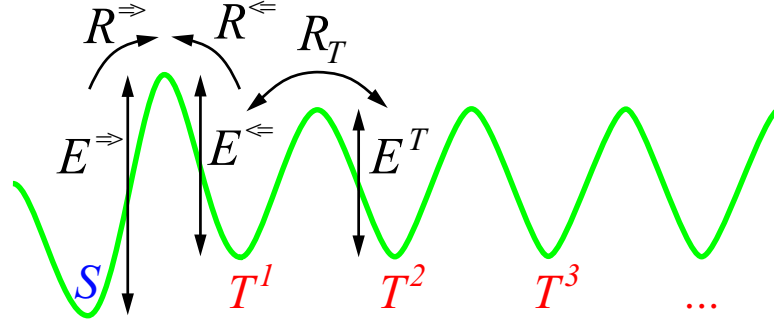


Fig. 5.7: Illustration of the one-dimensional rate-equation model used for the description of the kinetics of step-terrace diffusion. Hopping between the step site S and the first terrace site T^1 is characterized by the hopping-rates R^{\Rightarrow} and R^{\Leftarrow} which depend on the diffusion barriers E^{\Rightarrow} and E^{\Leftarrow} . The diffusion on the terrace is described between equivalent terrace sites with the hopping-rate R^T .

which is illustrated in Fig. 5.7. In the following we neglect the interaction between the adsorbed particles.

To simplify the diffusion process we assume that the diffusion on the terraces is fast compared to the migration from steps, because the oxygen binds stronger on the step sites than on the terrace sites. The deviation of the step coverage from equilibrium

$$\Delta\theta_s(t) = \theta_s(t) - \theta_s(t \rightarrow \infty) \quad (5.1)$$

decreases exponentially with time [35]:

$$\begin{aligned} -\frac{d\Delta\theta_s(t)}{dt} &= R^{\Rightarrow} \Delta\theta_s(t) \\ &= R^{\Rightarrow} \Delta\theta_s(0) \exp(-R^{\Rightarrow}t) \end{aligned} \quad (5.2)$$

Here, R^{\Rightarrow} is the hopping-rate. In the case of a repetitive transient excitation, dt is discrete and corresponds to the period between two laser shots Δt . Therefore, $R^{\Rightarrow} = p_{diff}/\Delta t$. As can be seen in Fig. 5.8, this model describes the experimental data quite well for lower fluences (c, and d). For higher fluences (a, and b,) significant deviations are visible. Here, the differences of the diffusion barriers are less important and a partial site blocking on the terraces slows down the diffusion in direction perpendicular to the steps.

In order to take into account the diffusion kinetics on the terraces, we have used a refined rate-equation model similar to the approach used by Reutt-Robey *et al.* [61]. The change of the relative coverage θ_i of a site i is simply determined by the hopping-rates R_i^{\Rightarrow} , R_i^{\Leftarrow} and the relative coverage of the different sites θ_i :

$$\begin{aligned} \frac{d\theta_i}{dt} &= R_{i-1}^{\Rightarrow} \theta_{i-1} (1 - \theta_i) - R_i^{\Leftarrow} \theta_i (1 - \theta_{i-1}) \\ &\quad + R_{i+1}^{\Leftarrow} \theta_{i+1} (1 - \theta_i) - R_i^{\Rightarrow} \theta_i (1 - \theta_{i+1}) \end{aligned} \quad (5.3)$$

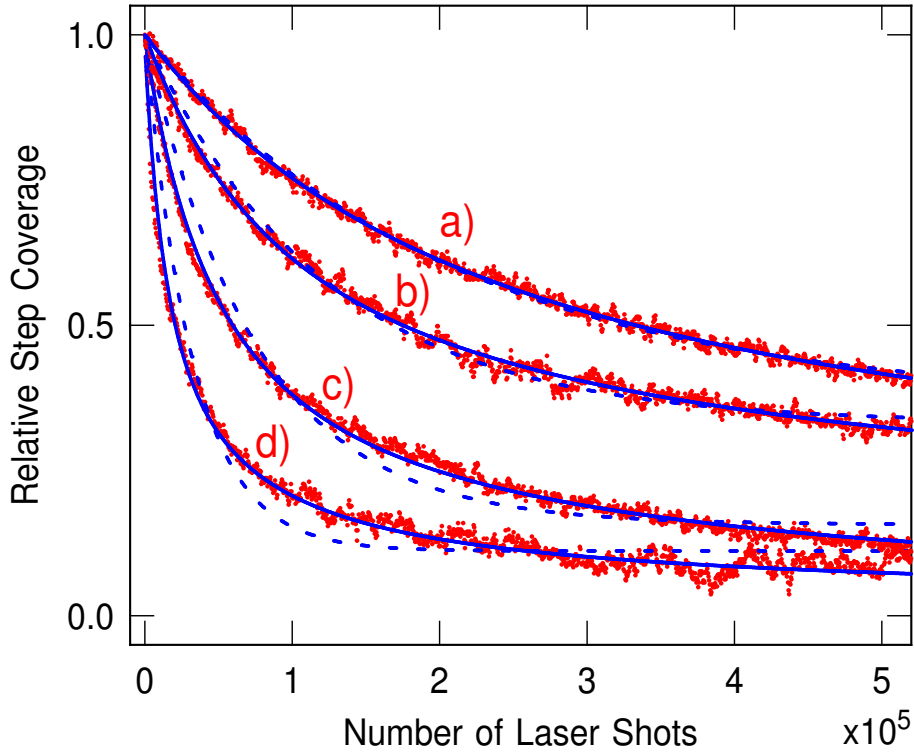


Fig. 5.8: Relative coverage of oxygen at steps θ_s as a function of applied laser shots for absorbed fluences of a) 4.6 mJ/cm², b) 4.8 mJ/cm², c) 5.1 mJ/cm², and d) 5.6 mJ/cm². The data points are obtained from the measured SH signal using Eq. (4.3). Fits using Eq. (5.2) and Eq. (5.3) are drawn as dashed and solid lines respectively.

Here, $i = 0, \dots, N$ with being N the number of terrace sites and $i = 0$ the step site. In thermal equilibrium, the hopping-rate at temperature T is given by Boltzmann factor:

$$R_i = \nu_i \exp(-E_i/kT) \quad (5.4)$$

with E_i being the barrier heights and ν_i the prefactors. For laser-induced diffusion, R_i is the hopping-rate integrated over one laser shot.

We restrict the diffusion from the steps onto the neighboring terrace by setting $R_0^{\leftarrow} = 0$ and $R_N^{\rightarrow} = 0$. With one step site per terrace and by assuming equivalent terrace sites, we can reduce the number of distinct barriers to three, namely the hopping-rate between terraces sites R^T and the hopping-rates from and to the step site R^{\rightarrow} and R^{\leftarrow} . The hopping-rate between terrace sites R^T determines only the curvature of the step coverage as a function of time. A small hopping-rate on the terraces leads to a slowdown of the migration from the steps due to a partial blocking of the neighboring terrace sites. Fits of the numerical solution of Eq. (5.3) are shown as solid lines in Fig. 5.8. Since we are interested primarily in the hopping-rate from

steps onto terraces R^{\Rightarrow} which dominates the initial kinetics and in order to keep the number of free parameters small, we have set $R^{\Leftarrow} = R^T$ here. Nevertheless, this model can describe the experimental data even for high laser fluences within the whole coverage range (see the solid lines in Fig. 5.8).

The equilibrium coverage of the step site is influenced by three factors: (i) the difference of the binding energies between step and terrace sites $\Delta E = E^{\Rightarrow} - E^{\Leftarrow}$; (ii) the number of terrace sites, which is given by the miscut of the crystal and (iii) the excitation density. In the case of thermal diffusion, the relative equilibrium coverages for step and terrace sites θ_S^{eq} and θ_T^{eq} at a temperature T are related by

$$\frac{\theta_S^{eq}(1 - \theta_T^{eq})}{\theta_T^{eq}(1 - \theta_S^{eq})} = \exp(-\Delta E/kT). \quad (5.5)$$

The fact that we observe partial depletion of the steps by thermal diffusion for temperatures of 260 K and higher, restricts ΔE to values around 0.1 eV. The situation is very similar to N on Ru(0001) where a STM-study of thermal step-terrace diffusion around 300 K gives a diffusion barrier of 0.94 eV [60], while the binding energy difference between step and terrace sites has been calculated to be in the range of only 0.03-0.25 eV [90].

5.5 Fluence Dependence

One characteristic feature of experiments in the DIMET-regime is a nonlinear dependence of the yield on laser fluence, which has been attributed to the repetitive electronic excitation [46]. In contrast, a single non-thermal excitation process is characterized by a linear fluence dependence [9]. Figure 5.9 displays several sets of raw SHG data during oxygen dosing and induced diffusion for various absorbed fluences. It demonstrates the high reproducibility of the experiment and the strong dependence of the diffusion rate on laser fluence. Variation of the laser fluence by only 50% covers the whole accessible dynamic range of the diffusion rate.

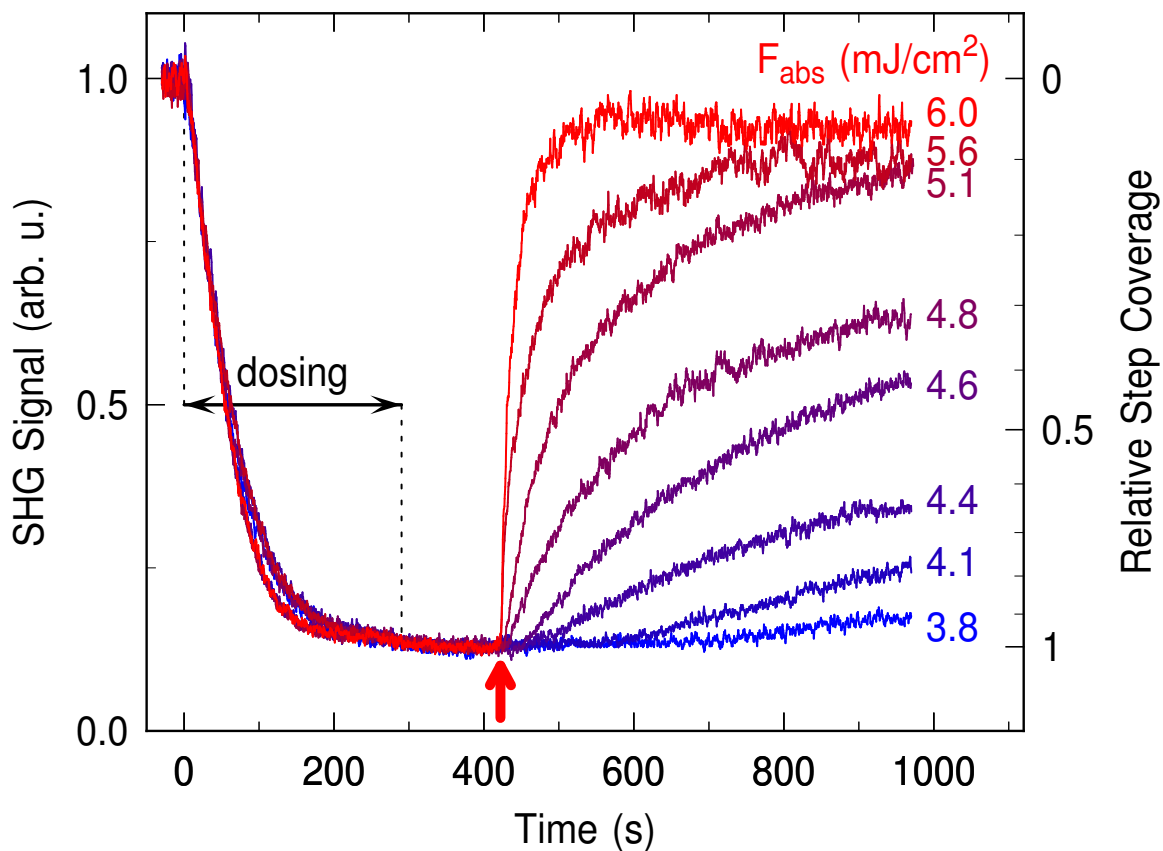


Fig. 5.9: Second-harmonic signal of the probe beam as a function of time. First, oxygen is dosed at a temperature of 160 K followed by cooling the sample to 80 K. From the time which is marked by the vertical arrow on, diffusion is induced by applying pump pulses at a repetition rate of 1 kHz with different fluences as indicated. The right scale is a conversion of the SHG signal into the relative step coverage as described in Sect 4.5.

Experimentally, for each of these measurements the steps of our sample were decorated with oxygen before the diffusion was induced with different pump laser fluences. Between each two measurements the sample was cleaned: first it was flashed to 1100 K,

then oxygen was dosed and finally it was flashed once more to 1100 K.

The intensity of the pump beam was varied with a combination of a half-wave plate and a thin-film polarizer and was measured by a power meter. The absorbed fluence was calculated using the optical constants of platinum [82] and assuming a constant absorption, which has been verified by Her *et al.* [12] for absorbed fluences up to several mJ/cm^2 .

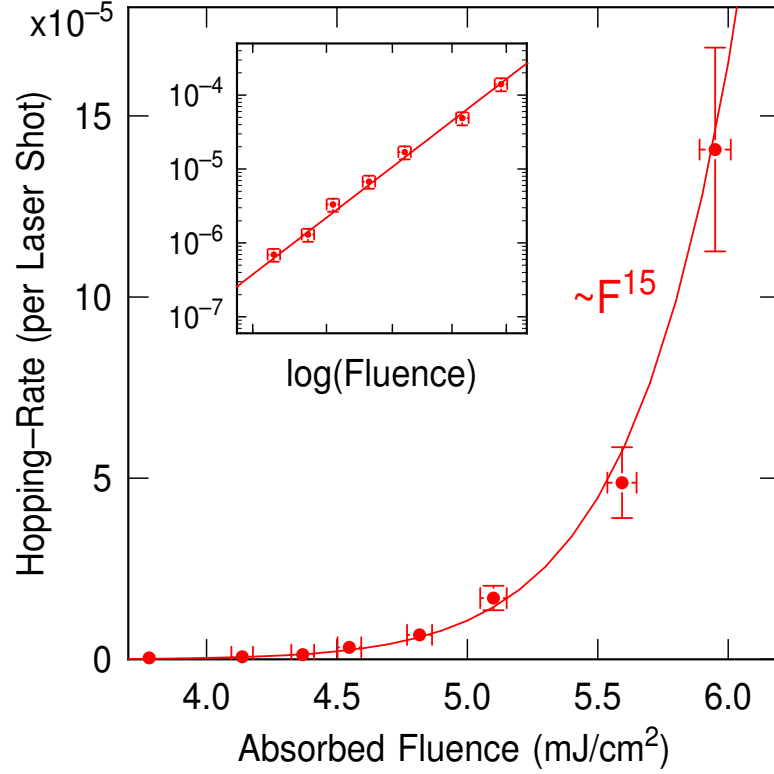


Fig. 5.10: Hopping rate per laser shot for the diffusion of oxygen from the steps onto the terraces as a function of adsorbed laser fluence F . The solid line shows a power law $\propto F^{15}$.

Plotting the initial hopping-probability per laser shot p_{diff} as a function of absorbed fluence reveals an extremely strong nonlinear fluence dependence (Fig. 5.10). In the investigated fluence range it can be described by a power law of the form $p_{\text{diff}} \propto F^x$ as it is the case for the desorption probability in most femtosecond desorption experiments. However, the nonlinearity shown here with $x = 15$ is much stronger than in all laser-induced desorption experiments so far, where an exponent in the range of 3–8 has been typically observed [3,6,8,10]. Even for such a strong nonlinearity, the factor of ten smaller spot size of the probe beam ensures that the yield is spatially uniform over the diameter of the probe beam within 10%. The nonlinear detection further narrows the effective probe diameter by a factor of $\sqrt{2}$, which finally reduces the non-uniformity to 5%. Thus, yield-averaging of the laser fluence [10] is not necessary here.

5.6 Two-Pulse Correlation Measurement

The assignment of an electronically induced diffusion process requires knowledge about the pathway of the energy transfer from the optically excited electrons to the diffusive motion. This has been revealed by the application of a two-pulse correlation scheme (see Fig. 5.11) which was first applied to laser-induced desorption by Budde *et al.* [4]. For this purpose, the pump pulse is split into two pulses with a variable time delay. Only for delays in which the system retains memory of the first excitation the second pulse can generate an enhanced yield compared to independent excitations. As in nonlinear optics, this requires a nonlinear dependence of the reaction yield on the laser fluence.

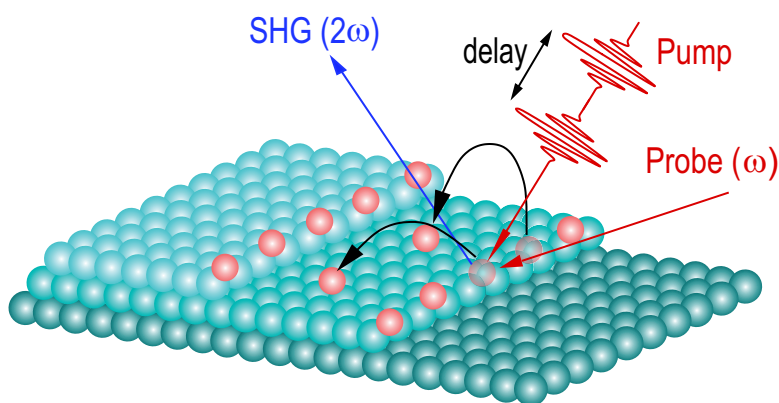


Fig. 5.11: Principle of the two-pulse correlation technique. The diffusion yield is measured as a function of delay between the two excitation pulses.

The width of such a two-pulse correlation provides information about the timescale of the energy transfer from the initial excitation of the electrons to the adsorbate motion and allows the distinction between an electron- and a phonon-mediated process. A transfer time of less than a few picoseconds indicates a direct energy flow from the excited electrons to the adsorbate degree of freedom, whereas a coupling via the phonon system is characterized by a transfer time that is one order of magnitude longer [13].

For two-pulse correlation measurements, the pump beam was split into two beams in a Michelson interferometer. They were orthogonally polarized using a zero order half-wave plate in one arm of the interferometer to minimize interference effects. They were combined colinearly (see Fig. 3.4). The fluence of the two pump beams was chosen in a way (employing a beam splitter with 60% reflectivity for p-polarized light, see Fig. 3.4) that the absorbed fluence of the s and p polarized beams were approximately the same. The delay between these two pulses was controlled

by modifying the optical path with a linear positioning stage (Aerotech Zeta-drive) which was changed by motion controller (Aerotech Unidex 1).

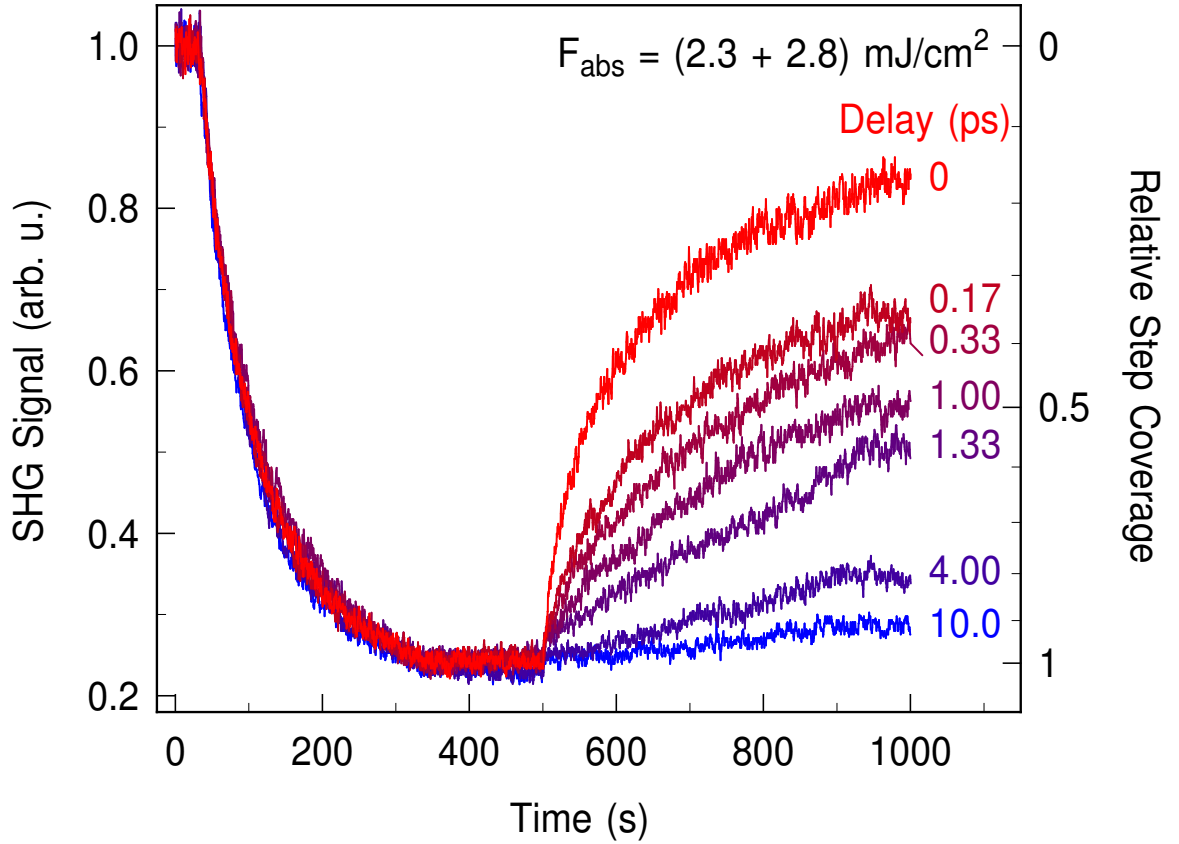


Fig. 5.12: Second-harmonic signal of the probe beam as a function of time delay between the two orthogonally polarized pump beams. First, oxygen is dosed at a temperature of 160 K followed by cooling the sample to 80 K. From time 500 s on diffusion is induced by applying pump pulses at a repetition rate of 1 kHz with different time delays as indicated.

The temporal and spatial overlap of the two pump beams was adjusted with the help of nonlinear interference between the two pump beams. For this adjustment they were both p polarized. In case of perfect overlap interference fringes could be seen and the interference contrast was the strongest when the delay between the two pump pulses was zero.

Choosing the fluences to be 2.3 and 2.8 mJ/cm² we realize an excitation scheme where one of the pump beams cannot raise diffusion. If the pulses are arriving at the same time or with a time-delay shorter than 10 ps there is a visible change in the SH signal (Fig. 5.12) indicating diffusion.

The hopping rate of the oxygen atoms from the step edges onto the terraces is calculated with the same one dimensional rate equation model, that was used for the calculation of the thermal diffusion rate (Sect. 5.4). After repeating the diffusion

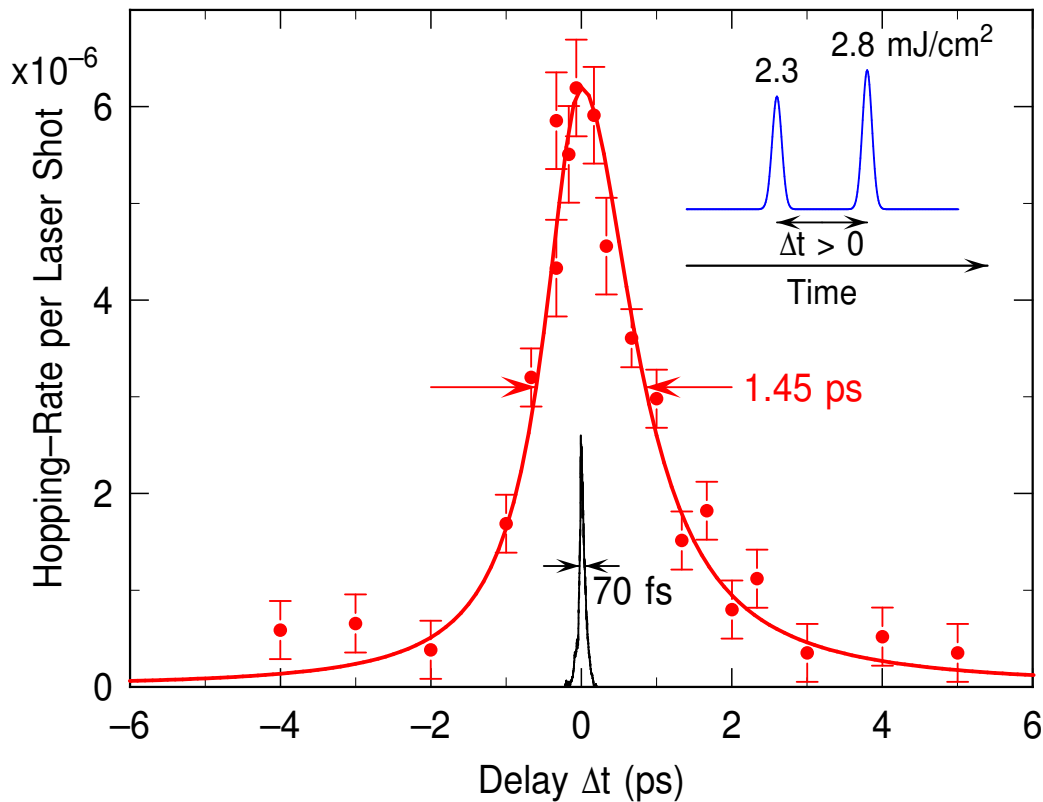


Fig. 5.13: Hopping rate per laser shot as a function of delay between the two cross-polarized pump beams with absorbed fluences of 2.3 and 2.8 mJ/cm², respectively (closed symbols). At positive delays, the weaker excitation precedes the stronger one as illustrated by the inset. The solid line is to guide the eye.

measurements with different delays set between the two pump pulses, we can calculate the hopping rate as function of the time delay between the pump pulses. Fig. 5.13 shows the hopping rate as a function of time delay between the two cross-polarized pump pulses. The two-pulse correlation shows a width of about 1.45 ps (FWHM) and a high contrast between the hopping rate at zero and at large delays which is related to the high nonlinearity of the fluence dependence. This very fast response time indicates electronically induced diffusion process, that will be discussed in detail in the next chapter.

Chapter 6

Modeling of the Diffusion

The two-pulse correlation as well as the fluence dependence of the hopping probability show the typical characteristics of a process which is induced by multiple electronic transitions. Thus, we have modeled fs-laser induced diffusion within the same formalisms used for the description of desorption.

The laser pulses excite electrons within the optical penetration depth of the metal. Within a few hundred femtoseconds [96, 97, 51] thermalization in the electron gas due to electron-electron scattering leads to a hot Fermi-Dirac distribution, while the lattice remains cold. Once thermal equilibrium is established among the excited electrons, one can assign separate temperatures for the electrons T_e , ions T_i , and for the adsorbates T_{ads} (see Fig. 6.1).

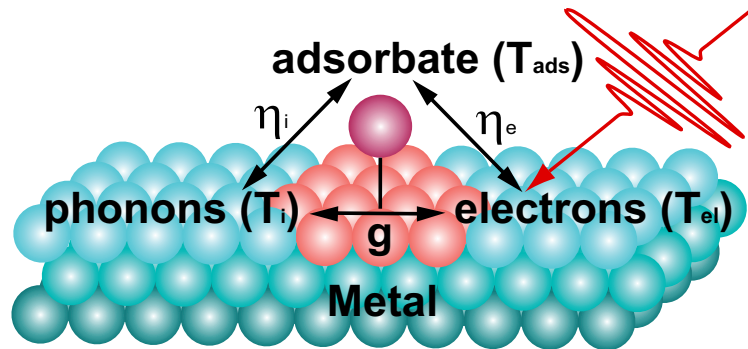


Fig. 6.1: Schematic model of the energy flow at metal surfaces after femtosecond laser excitation. The fs-laser pulses excites the electronic system of the metal substrate, and it equilibrates in a few ps with the lattice phonons.

The adiabatic (through phonons) and the non-adiabatic (through electrons) energy transfer can be described with this "simple" phenomenological model. The coupling between the different "heat-baths" can be described with different coupling constants: g describes the coupling between the electrons and phonons in the substrate, η_e and

η_i the coupling between the adsorbate and the substrate electrons and the surface phonons respectively.

Determination of the activation process which led to the desorption or diffusion is extremely difficult, because of the strong coupling between the electronic and phononic system of the metal substrate. The electron-phonon coupling leads to equilibrium between these two system, the typical time for this is ~ 1 ps (see Sect. 6.1). Discrimination of these two energy transfer processes in the thermal equilibrium, which needs typically few seconds, is not possible, because the electrons and phonons are equilibrated.

Typically, an indirect hot-electron excitation process for fs-laser excited surface reactions on metal surfaces is analyzed in two steps. First, the dynamics of the laser-excited hot-electron distribution is described by applying the well-known two-temperature model (see Sect. 6.1). Two principal models have been employed for the description of the second step, the energy transfer to the nuclear coordinates of the adsorbate (discussed in Sect. 6.2). At the end of this chapter in Sect. 6.3 and Sect. 6.4 we will show how the experimental results can be satisfactorily fitted.

6.1 Two-Temperature Model

In laser induced processes the laser interacts first with the electrons of the substrate, transferring energy to the electron heat bath. The surface electrons relax by heat diffusion into the bulk and by coupling to phonons. The time evolution of the electron and phonon heat bath can be described by the so-called two-temperature model which can be used to determine the electron-phonon coupling.

Due to the small electronic heat capacity, electron temperatures of several thousand Kelvin can be reached (see Fig. 6.2). Subsequent cooling of the electrons proceeds on a timescale of picoseconds by electron-phonon coupling and by diffusive electron transport into the bulk. In spite of the simplicity of this model and the neglect of the initial non-thermal distribution of the electrons, it has been successfully applied not only for the description of electron and phonon dynamics in femtosecond laser-induced surface reactions, but also for the analysis of transient linear reflectivity [98], which can be used for the determination of electron-phonon coupling constants [99], and for the prediction of laser damage thresholds [100].

The interaction between the substrate phonons and electrons can be described in the two-temperature model, for electron and lattice temperatures (T_e , T_i) with

coupled differential heat equations [101]:

$$C_e \frac{\partial}{\partial t} T_e = \frac{\partial}{\partial z} \left(\kappa_e \frac{\partial}{\partial z} T_e \right) - g(T_e - T_i) + S(z, t) \quad (6.1)$$

$$C_i \frac{\partial}{\partial t} T_i = \frac{\partial}{\partial z} \left(\kappa_i \frac{\partial}{\partial z} T_i \right) + g(T_e - T_i). \quad (6.2)$$

C_e and C_i are the heat capacities of electrons and lattice respectively, and κ_e and κ_i are the thermal conductivities of the electrons and the lattice. On the right side of the first equation, the first term describes the thermal diffusion, and the second term the electron-phonon coupling which can be handled as a constant (see in Appendix A.2). The third term $S(z, t)$ is the optical excitation or so-called source term. The calculation of the source term can be found the Appendix A.3.

The specific heat capacity of the electrons C_e is [102]:

$$C_e(T_e) = \gamma T_e \quad (6.3)$$

where γ is the electron heat capacity (see Tab. A.1). The heat conductivity of the electrons can be expressed with the empirical heat conductivity κ_0 ,

$$\kappa_e = \kappa_0 T_e / T_i. \quad (6.4)$$

In metals, in contrast to the electronic heat conductivity, the phononic heat conductivity is not considered [103, 102, 104].

The specific heat capacity of the phonons is described by the Debye model [102]:

$$C_i(T_i) = 9nk_B \left(\frac{T}{\Theta_D} \right)^3 \int_0^{\Theta_D/T_i} \frac{x^4 e^x}{(e^x - 1)^2} dx, \quad (6.5)$$

where n is the density of atoms and Θ_D is the Debye-temperature (see Tab. A.1).

Fig. 6.2 shows the numerical calculation of the two-temperature model applied to our Platinum crystal after laser excitation by 50 fs, 5mJ/cm². The laser pulse (50fs) is much shorter than the typical electron-phonon equilibration time (\approx 2ps), and since the electrons have very low heat capacity, the electrons reach a very high temperature (\approx 2500K) very rapidly. In the relaxation process, the electron temperature T_e is lowered through energy transfer to the phonons, resulting in an increase of the phonon temperature T_i , and heat diffusion into the bulk.

Although it can take up to several hundred femtoseconds until the initial non-equilibrium energy distribution of the excited electrons transforms into a hot Fermi-Dirac distribution by electron-electron scattering (see in Appendix A.1), the assumption of an instantaneous thermalization is reasonable in most cases, since an indirect excitation of an adsorbate by hot electrons typically proceeds on the timescale of one picosecond as indicated by the width of the corresponding two-pulse correlation (see Sect. 5.6).

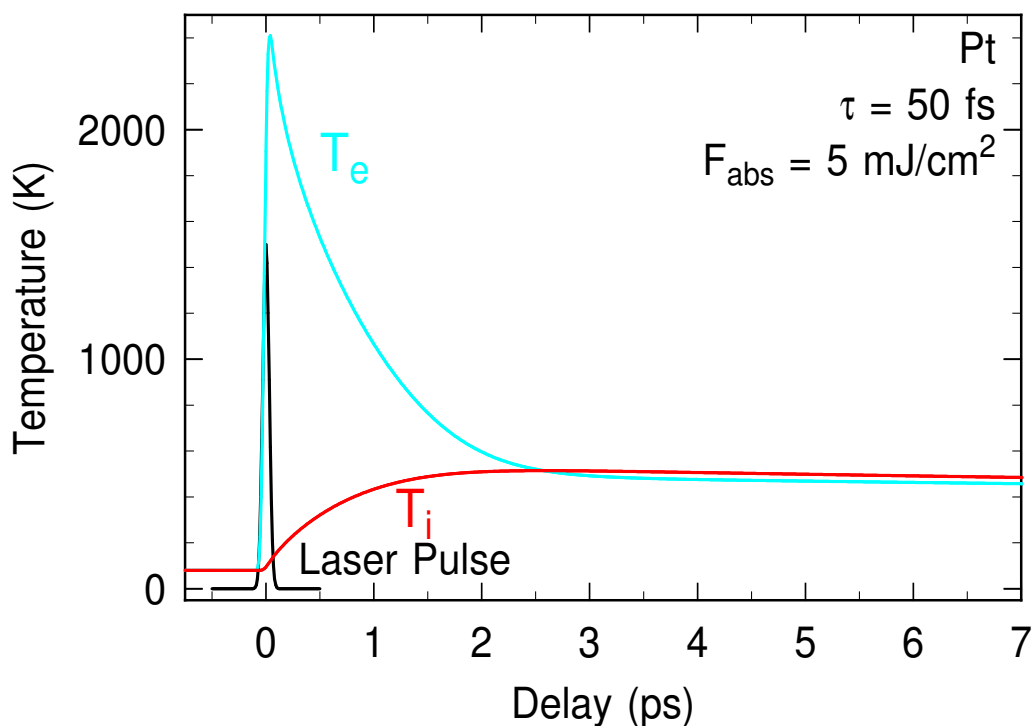


Fig. 6.2: Time dependence of the electronic temperature T_e and lattice temperature T_i after excitation of the substrate with a fs-laser, calculated with Eq. 6.1.

6.2 Electronic Friction Models

Two principal models have been employed for the description of the second step, the energy transfer to the nuclear coordinates of the adsorbate. One is the DIMET-model [46], which describes the excitation of the adsorbate by multiple electronic transitions between potential energy curves with high lying adsorbate levels (see paragraph 2.1). It emphasizes the dynamics of the adsorbate on the excited potential energy surface (PES) from where it rapidly falls into the ground state due to the strong coupling to the surface. It is derived from the MGR-model [1, 2] of the usual DIET process in which desorption occasionally occurs if a molecule remains sufficiently long on an antibonding PES. A description in the DIMET model is most advantageous if the adsorbate dynamics proceed most of the time on one of the PES, and excitations are relatively rare. Despite the rapid progress in theory [105], however, most theoretical descriptions in the DIMET model have no predictive character due to the lack of parameter-free potential energy surfaces.

For an increasing number of excitation and deexcitation cycles by Franck-Condon transitions at a different distance to the surface, the electronic excitations lead to an effective vibrational heating in the ground state, which becomes more and more

important for the desorption process. Within this limit, the DIMET model makes contact to second, the electronic friction model [21,22,23,24] which treats the coupling between the adsorbate and the electrons via an effective electronic friction. It is based on the theory of vibrational damping of adsorbates by the creation of electron-hole pairs [106, 107], which is the inverse process of electronic excitation of adsorbate motion. It emphasizes the dynamics on the ground state PES perturbed by the excited electrons and is most suitable in the presence of low-lying excited states of the adsorbate-substrate system. However, both descriptions are closely related and describe the same physical processes from different points of view.

The DIMET picture is able to take into account the highly excited states as the ionization of the adsorbate, but it cannot describe the electronic friction [23]. The quantitative description of this model is very difficult, because we have to know the appropriate potential energy trajectories.

Empirical Electronic Friction Models

These models are based on the description of the damping of adsorbate vibrations due to electron-hole pair creation [106, 107], which opens a channel for energy dissipation. The electronic energy loss process can be described in terms of the electronic friction, acting in the atomic coordinates of the adsorbate.

In this approach, the adsorbate motion is assumed to occur on a single potential energy surface, and the electron-hole pair excitations are allowed to exchange energy with the adsorbate motion.

The master-equation formalism was introduced to describe the vibrational level population [108, 109] for a harmonic oscillator in contact to baths with the electronic and the lattice temperature, T_e and T_{ads} , respectively. Since only a few of the lowest lying vibrational states are excited, the harmonic oscillator gives a good approximation to characterize the density of states (DOS) of the vibrations of the adsorbate.

From the master equation the temporal evolution of the average vibrational energy can be deduced:

$$\frac{d}{dt}U_{ads} = -\eta_e[U_e - U_{ads}] + \eta_{ph}[U_{ph} - U_{ads}]. \quad (6.6)$$

U_e , U_{ph} , and U_{ads} are the energies of the oscillator in equilibrium with the electron temperature T_e , the lattice temperature T_{ph} , and the adsorbate temperature T_{ads} . The average vibrational energy of the "heat-bathes" is given by the Bose-Einstein distribution as [108]:

$$U_x(t) = h\nu_{ads}(e^{h\nu_{ads}/k_B T_x} - 1)^{-1}, \quad (6.7)$$

where $h\nu_{ads}$ is the frequency of the adsorbate vibration along the reaction coordinates.

The constant friction coefficient η_e describes not only the energy transfer between the hot electrons and the adsorbate oscillation, but it can be grasped also as damping coefficient. As such a parameter, it can also describe the energy relaxation time τ_e between the electrons and adsorbate at a surface as [108]:

$$\eta_e = \frac{1}{\tau_e}. \quad (6.8)$$

Solving Eq. 6.6 with the time dependent electron T_e and lattice temperature T_{ph} derived from the two-temperature model (see Sect. 6.1) and with Eq. 6.7, it gives the time dependent adsorbate temperature T_{ads} . From the adsorbate temperature T_{ads} the reaction rate R (e.g. desorption, diffusion) can be calculated by an Arrhenius-type expression as:

$$R(t) = -\frac{d}{dt}\Theta(t) = \Theta(t)\nu_{ads}e^{-E_a/k_B T_{ads}(t)} \quad (6.9)$$

Here Θ is the coverage. The yield of the reaction is given by the time integration of the reaction rate R, which is for a single laser shot at small change of the coverage ($\Theta \approx 0$) that is simply given as

$$P = \int \nu_{ads} \exp(-E_a/k_B T_{ads}(t)) dt. \quad (6.10)$$

The electronic friction approach is in the adiabatic picture, being based on its original form on low lying excited states of a coupled adsorbate-substrate system. It cannot describe the highly excited electronic states - as i.e. ionized states - of the adsorbate.

Unified Model

Brandbyge *et al.* [23] have shown that both regimes can be covered within a generalization of the electronic friction model, for the low energy regime a friction-like description, and for the high energy regime a DIMET-like description. In this simplified model, the adsorbate is modeled as having a single electronic level ε_a .

The adsorbate level ε_a can tunnel into the continuum represented by the substrate conduction band, giving it a lifetime broadening Δ , and the coupling to the phonons is neglected. The electronic ground state of the adsorbate on the surface is represented by the Fermi-level intersecting the resonance at ε_a at some point.

To find an appropriate electronic friction coefficient η which depends on the position of the adsorbate and the electronic structure of the substrate Brandbyge *et al.* [23] used the Langevin-equation approach. The electronic friction couples Langevin noise from the electronic heat bath into the adsorbate center-of-mass degree of freedom. They adopted an analytic and numerical approach to solve the problem.

The analytic approach is based on the simple truncated harmonic well with a spatially independent friction. The Langevin equation with a local friction can be written in terms of a Fokker-Plank equation. The probability distribution $W(\epsilon, t)$ for the adsorbate to have energy ϵ above the bottom of the well obeys in the Fokker-Plank equation,

$$\frac{\partial W}{\partial t} = \eta(t) \frac{\partial}{\partial \epsilon} \left(\epsilon \left[1 + T_e(t) \frac{\partial}{\partial \epsilon} \right] W \right), \quad (6.11)$$

equivalent for a harmonic well to a Langevin equation with friction η and reservoir temperature T_e [23].

The excitation of the adsorbate is described by a temperature T_a which is coupled to the electron temperature T_e by the electronic friction coefficient η_e as:

$$\frac{\partial}{\partial t} T_a(t) = \eta_e [T_e(t) - T_a(t)]. \quad (6.12)$$

The solution of Eq. 6.12 gives the time-dependent adsorbate temperature, which can be used to calculate the rate $R(t)$ for a process with barrier E_a

$$R(t) = \eta_e \frac{E_a}{kT_a(t)} e^{-E_a/kT_a(t)}. \quad (6.13)$$

Note that here the adsorbate temperature T_a enters to the solution, which suggest a two-step picture. First the energy has to be transferred from the electronic degrees of freedom at temperature T_e through Eq. 6.12 into the adsorbate degree of freedom to reach temperature T_a , and then the desorption occurs as result of Eq. 6.13. The rise of the adsorbate temperature and the desorption process is controlled by the friction coefficient η_e [23].

The numerical solution of the Langevin equation enables to handle the spatially varying and arbitrary well shaped friction [23]. The Langevin equation describes the trajectory of the center-of-mass coordinate of the adsorbate, x :

$$\frac{d^2 x}{dt^2} + \eta(x, t) \frac{dx}{dt} = \frac{F(x)}{M} + \Gamma(t) \quad (6.14)$$

where M is the adsorbate mass and $\eta(t)$ is the friction, which depends on the time through the temporal dependence of the substrate electronic temperature, T_e . $F(x) = -dV(x)/dx$ is the force on the adsorbate from the potential energy surface $V(x)$, and $\Gamma(t)$ is a stochastic force with mean $\langle \Gamma(t) \rangle = 0$, which is described by the white noise spectrum:

$$\langle \Gamma(t) \Gamma(t') \rangle = q \delta(t - t'). \quad (6.15)$$

The white noise term q is determined by the temperature T_e , and the friction η through the fluctuation-dissipation theorem:

$$q = \frac{2\eta kT}{M}. \quad (6.16)$$

The result of these two approaches shows that the parameters fall into two well separated regimes:

If the width Δ of the adsorbate resonance is broad and near the Fermi-level, the electron-hole pairs dominate the friction channel, as the DOS at the Fermi-level is relatively large, so the friction is large at zero temperature and relatively temperature independent (friction-like).

If the width Δ of the adsorbate resonance is narrow and far above the Fermi-level, the dominant contribution of the friction is due to the thermal excitation from the Fermi energy to the resonance, this lead to strongly T-dependent friction. Since the resonance is narrow compared to its excitation energy, the results can be interpreted as repeated excitation between ground state and excited state (DIMET-like) [23].

6.3 Model calculation with Constant Friction

We have performed model calculations within the empirical and the generalized friction model in order to reproduce simultaneously the observed fluence dependence as well as the two-pulse correlation data. From thermal induced diffusion experiments we estimate the diffusion barrier from step sites onto the terraces to be $E_{\text{diff}} \approx 0.8$ eV (see sect. 5.2), substantially higher than the barrier for hopping between terrace sites which is within the range of 0.43-0.58 eV [72, 110]. For the two-temperature model we have used material parameters for Pt reported in reference [51] ($g = 6.76 \times 10^{17} \text{ WK}^{-1} \text{ m}^{-3}$, $\gamma = 748 \text{ JK}^{-2} \text{ m}^{-3}$, $\kappa_0(77 \text{ K}) = 71.6 \text{ WK}^{-1} \text{ m}^{-1}$, Debye temperature $T_D = 240 \text{ K}$).

Compared to the experimental data, however, the calculated hopping-probabilities are too large by 2-3 orders of magnitude, and the strong nonlinearity of the fluence dependence cannot be reproduced for a diffusion barrier of $E_{\text{diff}} \approx 0.8$ eV. (Figure 6.3.a). On the other hand, the normalized two-pulse correlations are only slightly broader than observed in the experiment. This shows that the energy transfer time, which is associated with the friction coefficient, is in the correct range. However, the huge discrepancy between the absolute values cannot be reduced by variation of the friction coefficient. A larger friction narrows the two-pulse correlation, but even further increases p_{diff} , while a smaller friction results in an even broader two-pulse correlation.

The contrast between p_{diff} at zero and large delays is slightly smaller for the unified friction model. This is mainly caused by the fact that the adsorbate temperature enters in the denominator of Eq. 6.13, which leads to a reduced rise of p_{diff} at small delays where the adsorbate temperature is large. Compared to the experimental data, however, the calculated hopping-probabilities are too large and the strong nonlinearity of the fluence dependence cannot be reproduced for a diffusion barrier of $E_{\text{diff}} = 0.8$

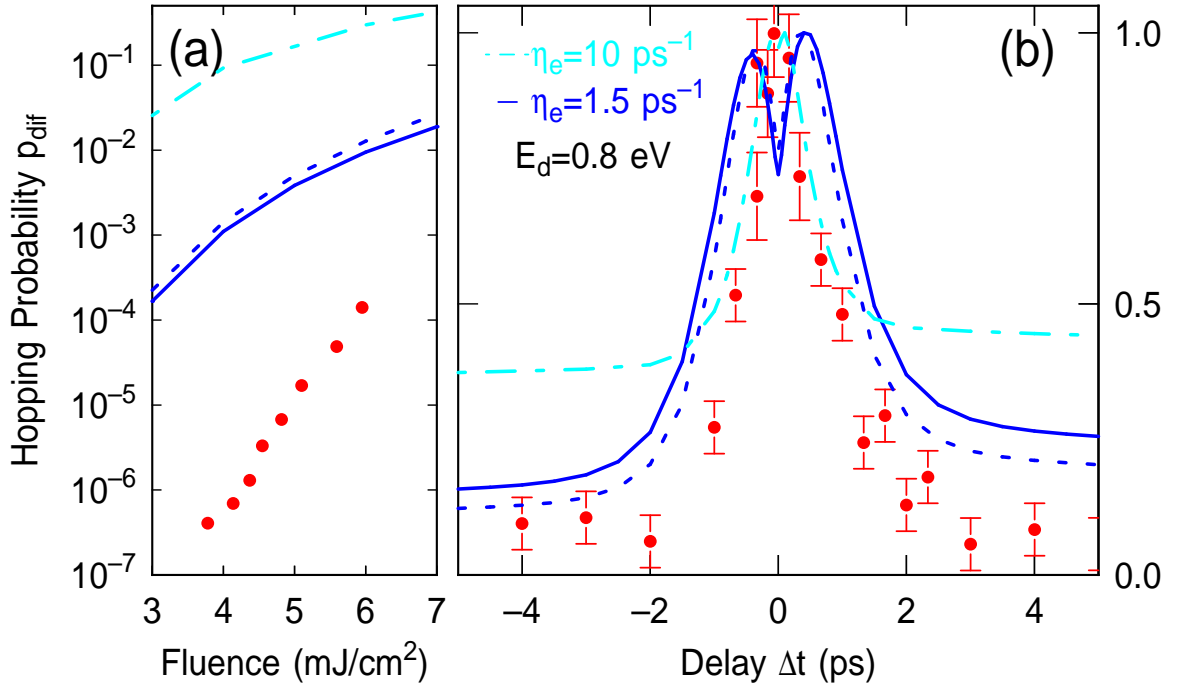


Fig. 6.3: On the left hand side is the calculated hopping probability p_{diff} as a function of absorbed fluence and on the right hand side as a function of time delay between two pump pulses for two constant friction coefficients $\eta_e = 1.5 \text{ ps}^{-1}$ and $\eta_e = 10 \text{ ps}^{-1}$. Experimental values are indicated by symbols. The solid and dashed-dotted line is the calculation from the generalized friction model and the dashed line from the empirical friction model.

eV. (Figure 6.3). On the other hand, the normalized two-pulse correlations are only slightly broader than observed in the experiment. This shows that the energy transfer time, which is associated with the friction coefficient, is in the correct range. A narrow two-pulse correlation can only be modeled with strong friction. However, this results in a hopping probability which is too large by several orders of magnitude, and in a poor contrast between zero and large delays. A strong fluence dependence and a high contrast of the two-pulse correlation can only be obtained with a small η_e . This, however, results in a two-pulse correlation that is much broader than measured. And with the increasing friction coefficient the fluence dependent measurements cannot be described at all [42, 111].

A rather good description of the observed fluence dependence and two-pulse correlation can be achieved if the diffusion barrier is arbitrarily increased. This is shown in Figure 6.4 which display the results of the generalized friction model with fixed friction and varying diffusion barrier E_{diff} . With increasing E_{diff} the width of the two-pulse correlation narrows, and the fluence dependence becomes steeper since the variation of the Boltzmann-factor in equation [4] becomes stronger the larger E_{diff} is

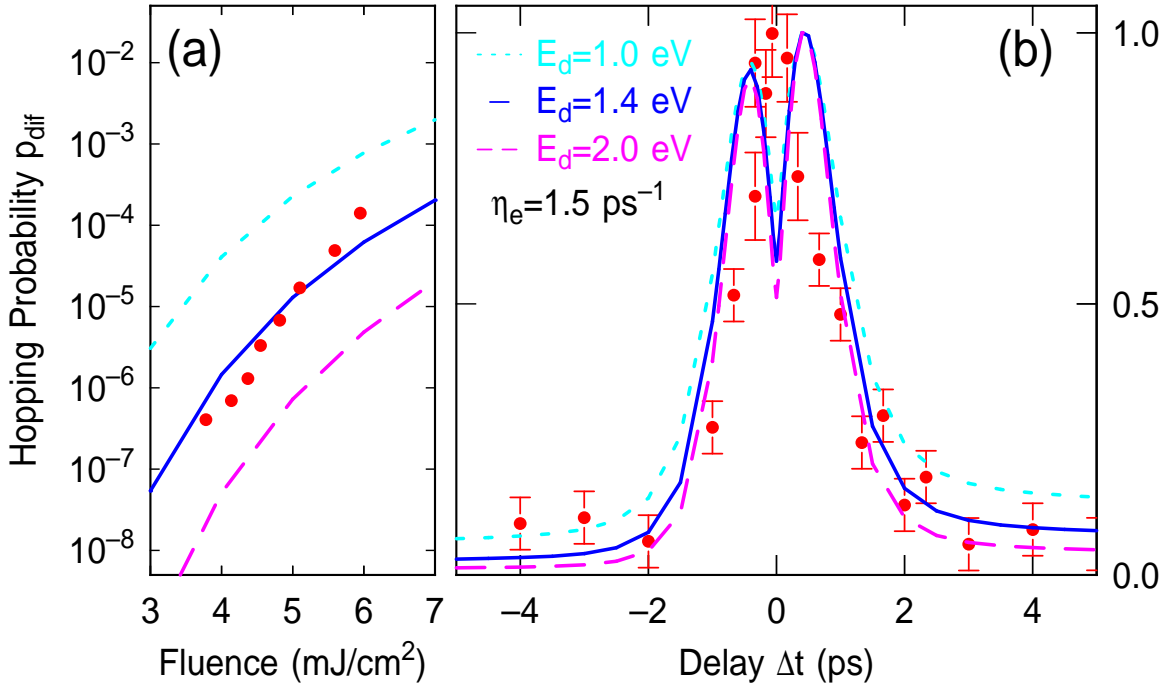


Fig. 6.4: On the left hand side is the calculated hopping probability p_{diff} as a function of absorbed fluence is shown and on the right hand side as a function of time delay between two pump pulses for a constant friction coefficients $\eta_e = 1.5 \text{ ps}^{-1}$, with different diffusion barriers E_d . The experimental values are indicated by symbols.

compared to kT_a . The best agreement is achieved for $E_{\text{diff}} = 1.4 \text{ eV}$ which is, however, much larger than the barrier observed for thermally activated diffusion. It has been argued that the activation energy of the generalized friction model in equation 6.13 has to be regarded as a modified activation energy which exceeds the depth of the well, indicating the population of excited states [112]. However, this argument is not consistent with the assumption of the generalized friction model. In both, the empirical as well as the generalized friction model, the binding of the adsorbate to the surface is approximated by an truncated oscillator potential of depth E_a , and the electronic excitation is represented by the friction coefficient. The main difference between both models is the handling of high-lying electronic states. While these are not covered by the empirical friction model, an electron-temperature-dependent friction is used in the generalized friction model in order to describe an (activated) population of an electronic state which cannot significantly be occupied at low temperatures. Thus, we have introduced an empirical dependence of the electronic friction on electron temperature in order to reproduce our data with a reasonable value for the diffusion barrier.

The dip of the calculated hopping-probability around zero delay in figure 6.3.b.

and 6.4.b. results from the competition between electron-phonon coupling and diffusive hot-electron transport [99]. The first tends to localize the heat at the surface while the latter is responsible for the distribution of the heat into the bulk. For delays which are small compared to the electron-phonon coupling time, the enhanced electron temperature leads to a stronger temperature gradient between surface and bulk. This results in a faster diffusion of the hot electrons into the bulk. Thus, the maximum ion temperature at the surface is reduced for small delays between the pump pulses. The more the dynamics of adsorbate and ion temperature become similar, i.e. for small friction, the more this reduction affects the adsorbate temperature. The hopping-probability should be even more sensitive on this effect since it depends exponentially on the adsorbate temperature. This consequence of the two-temperature model has been experimentally verified for the surface temperature of the substrate in time-resolved reflectivity measurements on various metal surfaces [99], but has not yet been observed in femtosecond surface photochemistry experiments. Even the laser-induced desorption of CO from Ru(0001) [13], which is believed to be mediated almost solely by substrate phonons, does not show this proposed reduction. This indicates that the full reaction dynamics are in fact more complicated than what can be described by a time-dependent adsorbate temperature coupled by a single friction coefficient.

6.4 Model calculation with Temperature Dependent Friction

Figure 6.5 show the results of the generalized friction model using a diffusion barrier of $E_{\text{diff}} = 0.8$ eV and a temperature dependent friction of the form:

$$\eta_e(T_e) = \eta_e^0 T_e^x, \quad (6.17)$$

with $x=3/2$, $x=2$, and $\eta_e^0 = 1.8 \times 10^5 \text{ K}^{-2}\text{ps}^{-1}$. Indeed, this parameterization reproduces particularly well the high nonlinearity of the fluence dependence and results in a narrow two-pulse correlation even for a low barrier.

The temperature-dependent friction results in a different dynamics of the adsorbate temperature. It shows only a fast rise-time and cools down slowly since the coupling strength rapidly decreases with electron temperature. Nevertheless, the hopping-rate R has dynamics on the timescale of one picosecond since $\eta_e(T_e(t))$ enters into its prefactor (Eq. 6.13). The dependence of R on electron temperature via η_e is responsible for the narrow two-pulse correlation shown in figure 6.5.b, which has its maximum at zero delay (see Fig 6.6).

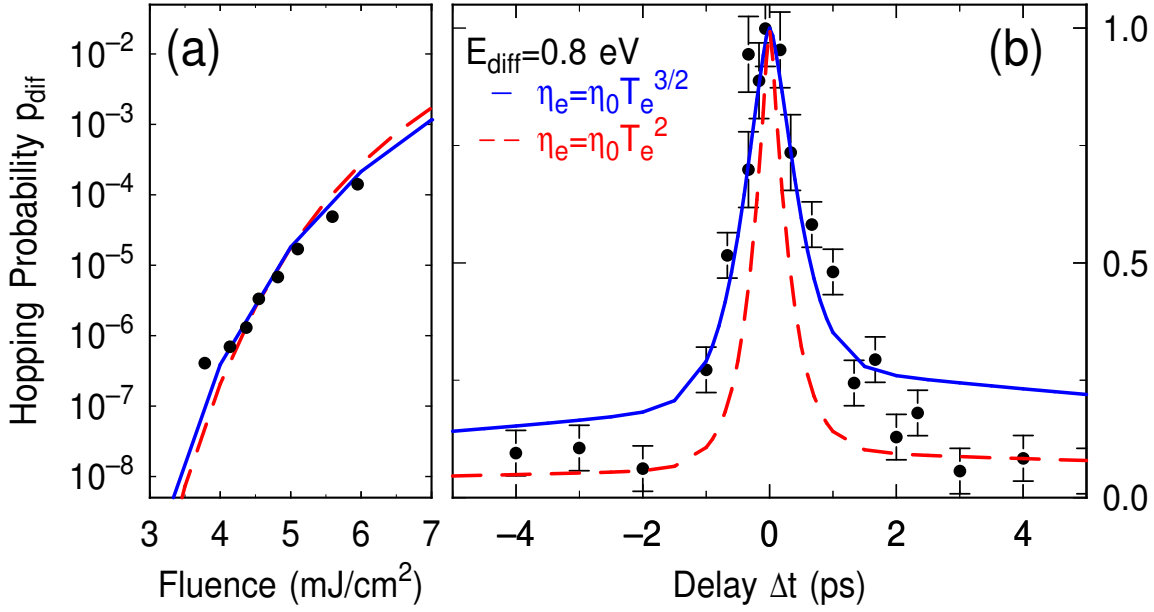


Fig. 6.5: Calculated hopping probability p_{diff} (a) as a function of absorbed fluence and (b) as a function of time delay between two pump pulses for an electron temperature dependent friction coefficient η_e . The experimental values are indicated by symbols.

The exact shape of the two-pulse correlation apparently depends on the analytic form of the assumed temperature dependence. For the chosen cases the two-pulse correlation is either somewhat smaller than the experimental one ($x = 2$) or does not reach the experimentally observed contrast ratio of p_{diff} between zero and large delays ($x = 3/2$). Nevertheless, these calculations demonstrate that a temperature-dependent friction can reproduce the main features of the experimental observations without choosing an unphysical barrier height.

For $x = 2$, the time-dependent temperatures for electrons, ions, and the adsorbate as well as the hopping-rate and the electronic friction coefficient are plotted in Fig 6.6. The friction shows a fast response due to the nonlinear electron temperature dependence, whereas the adsorbate temperature reveals only a fast rise time, but cools down slowly due to the vanishing coupling to the electronic system. Nevertheless, the hopping-rate R shows a dynamics on the timescale of one picosecond, since the electronic frictions enters not only into the electronic coupling (Eq. 6.12), but also into the diffusion rate (Eq. 6.13). The dependence of R on electron temperature via η_e is responsible for the narrow two-pulse correlation shown in figure 6.5., which has its maximum at zero delay.

The observed temperature dependence of the electronic friction coefficient represents a significant difference between the present results of laser-induced diffusion

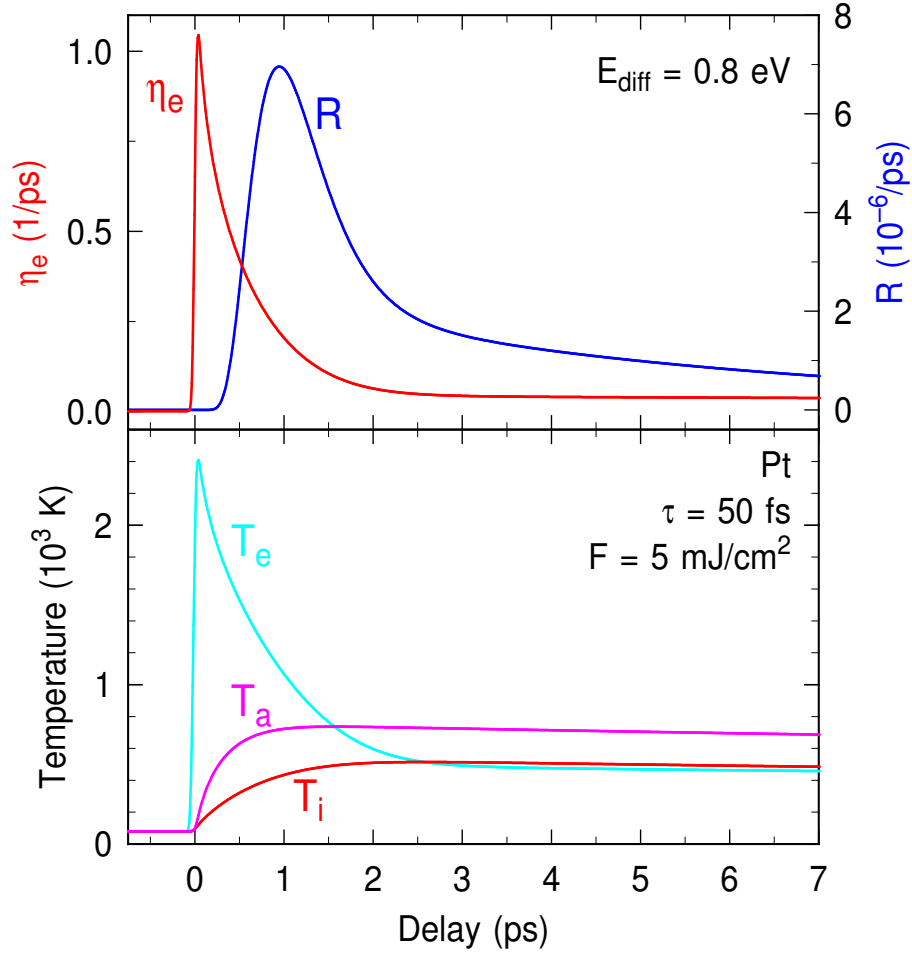


Fig. 6.6: Time-dependence of electron temperature T_e , ion temperature T_i , adsorbate temperature T_a , electronic friction coefficient η_e , and diffusion rate R as derived from the twotemperature and electronic friction model for an electron temperature-dependent friction $\eta_e(T_e) = \eta_e^0 T_e^2$, a laser pulse length of $s = 50$ fs and an absorbed laser fluence of 5 mJ/cm^2 .

and that of previous desorption experiments. Many of these experiments have been modeled very successfully using constant friction coefficients [7, 10, 13, 17]. We will in the following chapter only briefly discuss two possible explanations for the origin of $\eta_e(T_e)$, since a definite explanation would require a microscopic model for the electronic coupling of O/Pt, which is not available at present.

Chapter 7

Discussion and Perspectives

Since diffusion as well as desorption are the results of an excitation of adsorbate degrees of freedom, the mechanism of an electronic excitation should be similar. On the other hand, desorption occurs after excitation of vibrations of the adsorbate relative to the substrate, whereas diffusion needs the excitation of the frustrated translation. This suggests that the detailed excitation pathway for both processes may differ and depend on the degree of electronic versus internal coupling of the different motions.

The model calculations presented in the previous chapter have shown that the experimental data can only be reproduced with a reasonable value for the diffusion barrier if an electron-temperature dependence of the friction is introduced. In the following we will discuss possible reasons for this temperature dependence.

7.1 Position of the Unoccupied Adsorbate Level

One alternative to explain the temperature dependent friction is already contained within the generalized electronic friction model itself [23]. A narrow unoccupied adsorbate level far above the Fermi level naturally results in a temperature dependence of η_e (see Sect. 6.2 and left side of Fig. 7.1) because such a level can only be reached by highly excited electrons, i.e. at high electron temperatures (see right side of Fig. 7.1). It should also be mentioned that, in fact, most systems where desorption has been successfully modeled by a constant η_e have higher lying resonances than O/Pt [7, 10, 13].

X-ray absorption spectroscopy of O/Pt(111) by Puglia *et al.* [113] revealed a broad unoccupied resonance very close to the Fermi level as expected for a strongly bound atomic adsorbate. This resonance has been assigned to an anti-bonding state due to hybridization of the O 2p_z level and the Pt 5d band. A second, weaker and broader resonance centered at 8 eV above has been assigned to the hybridization of the Pt 6sp and the O 2p_{xy} states. Thus, energy transfer to the oxygen atoms, which weakens the O-Pt bond, can be expected even at low electron temperatures and without a strong temperature dependence.

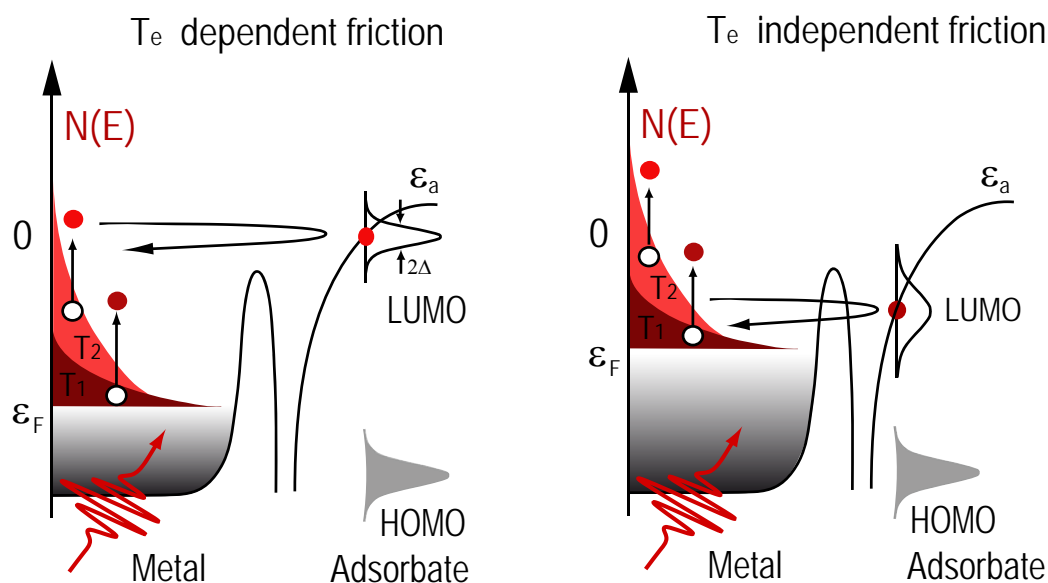


Fig. 7.1: If the unoccupied adsorbate level is lying far above the Fermi-level E_F of the substrate metal, the friction coefficient is depending on the electronic temperature T_e , because with higher and higher T_e more electrons can acquire energy to "jump" on the LUMO (left picture). If the Fermi-level E_F is laying close to the LUMO of the adsorbate, already with low T_e many electron can "jump" to the LUMO, so in that picture the friction is independent of T_e (right picture).

7.2 Indirect Excitation

Since the electronic structure of O on Pt(111) does not support a temperature dependence of the electronic friction coefficient, the question arises if the pathway of the energy transfer to the diffusive motion is more complicated than a direct coupling of the electronic excitation to the frustrated translation mode. For this reason we suggest an indirect excitation mechanism which requires an effective dependence of η_e on electron temperature within in the description of the friction model.

This mechanism is sketched in Fig. 7.2. It assumes a primary electronic excitation of the O-Pt stretch vibration, which indirectly excites the frustrated translation via anharmonic coupling. Since the anharmonicity of vibrations generally increases with amplitude, the corresponding coupling strength increases with the vibrational temperature of the O-Pt stretch. Its energy (60 meV) is only slightly higher than the

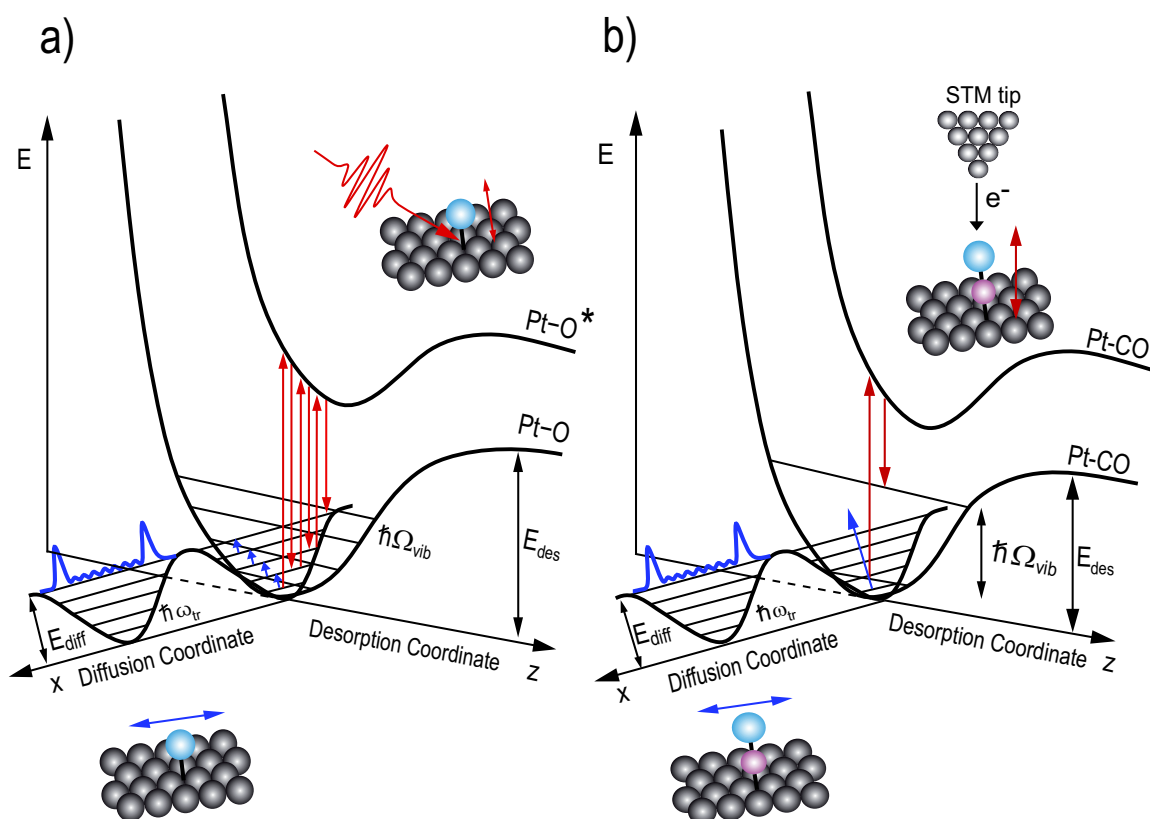


Fig. 7.2: Schematics of the two-dimensional potentials along the desorption coordinate z and along the reaction coordinate x . a) O/Pt(111). Exciting the high-frequency stretching mode by femtosecond laser pulses, many quanta of the stretch vibration mode need to be excited by repetitive electronic excitation cycles before the vibrational motion can overcome the diffusion barrier. b) CO/Pd(110). With exciting the high-frequency (HF) stretching mode by STM electrons, it is possible to overcome the diffusion barrier with indirect excitation of the low-frequency frustrated translation by anharmonic coupling. Here even one quantum of internal vibrational energy exceeds the diffusion barrier.

energy of frustrated O-Pt translations (50 meV) [114]. Therefore, many quanta of the stretch vibration mode need to be excited by repetitive electronic excitation cycles before the vibrational motion can couple efficiently to the lateral mode and before the diffusion barrier of 0.8 eV can be overcome. If such scenario is described by a single coupling strength, it will depend effectively on electron temperature, while the primary electronic excitation of the O-Pt stretch vibrations could still be mediated by a constant electronic friction η_e , as illustrated in Fig. 7.3.

This model is motivated by different simulations and measurements.

The first one is a theoretical calculation of a reverse process, it is a stochastic

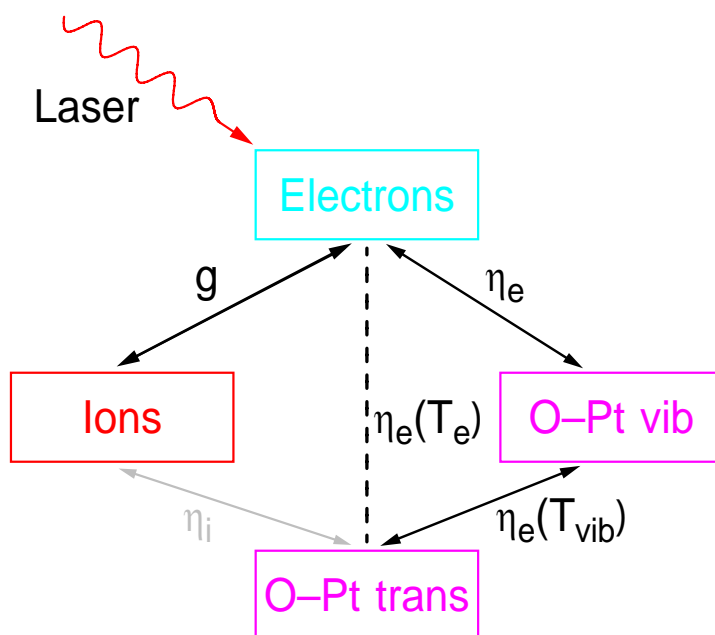


Fig. 7.3: Scheme of the energy transfer from the optical excitation of the electrons to the frustrated translation mode which initiate the diffusive motion of the oxygen atoms. An effective dependence of the electronic friction η_e on electron temperature T_e can result from an indirect excitation by anharmonic coupling between the O-Pt stretch and the O-Pt translation mode.

dynamics simulations of vibrational relaxation rates for CO adsorbed on Cu(110) by Tully *et al.* [115]. At metals, the non-adiabatic excitation or deexcitation of electron-hole (e-h) pairs via adsorbate motion provides an alternative pathway to phonon creation or annihilation. They showed that, at low temperatures, the e-h pair mechanism dominates the relaxation of not only the C-O stretch, but the frustrated rotation as well. With increasing temperature the phonon-induced lifetimes of the three modes (frustrated rotation, frustrated translation, and CO-Cu stretch, see Fig. 7.4) decrease strongly, at room temperature these two mechanism are competitive. Only for the frustrated translation electronic coupling is weak and dominated by the phonon mechanism.

Second, STM experiments of Komeda *et al.* [31] and Pascual *et al.* [33], who showed a threshold energy for inducing diffusion of CO/Pd(110) and NH₃/Cu(100) by inelastic electron tunneling, which coincides with the internal C-O and N-H stretch vibration respectively. The lateral motion is shown to be initiated by anharmonic coupling between the high-frequency internal and the low-frequency frustrated translation mode. For these systems even one quantum of internal vibrational energy exceeds the

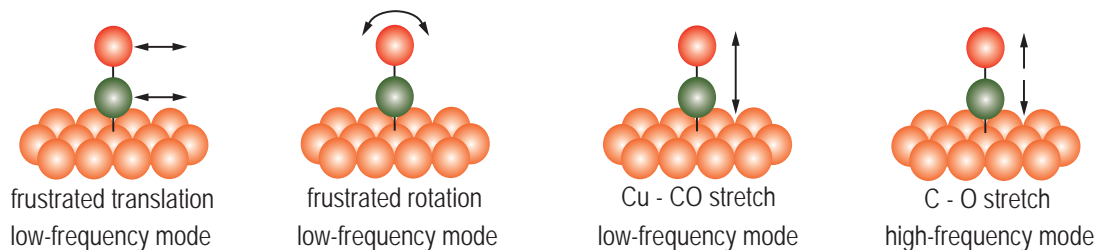


Fig. 7.4: Vibrational modes of the system CO/Ru(100). The three low-frequency modes: frustrated translation, frustrated rotation, and CO-Cu stretch, and the high-frequency C-O stretch mode [115].

diffusion barrier (see Fig. 7.2.b). Thus, an indirect excitation of lateral motion is possible, even if the low current in the STM experiments of $< 0.05 e^-/ps$ inhibits ladder climbing due to the short lifetimes of the vibrational modes on metal surfaces.

The importance of the anharmonic coupling has been demonstrated in the experiments of Komeda *et al.* by comparing CO/Pd(110) and CO/Cu(110) (see Tab. 7.1). Even if the diffusion barrier of the latter is smaller by a factor of two, no lateral hopping by excitation of the internal stretch could be observed. This has been explained by the different strength of the anharmonic coupling [116, 117] which is larger by a factor of more than 20 for CO/Pd(110) (see Tab. 7.1).

	CO/Pd(110)	CO/Cu(100)	O/Pt(111)
$\hbar\Omega$ [meV]	250	240	60
$\hbar\omega_0$ [meV]	25	3.9	50
E_{diff} [meV]	180	97	800
$\hbar\delta\omega$ [meV]	4.3	0.18	2
Diffusion	yes	no	yes

Tab. 7.1: The different energies of the CO/Pd(110), CO/Cu(100), and O/Pt(111) systems. $\hbar\Omega$ is the energy of the high-frequency (HF) mode, $\hbar\omega_0$ is the energy of the low-frequency (LF) frustrated translation mode, E_{diff} is the diffusion barrier, and $\hbar\delta\omega$ is the anharmonic coupling between the HF and LF modes. The values are taken from Ref. [31, 114, 42].

The anharmonic coupling of vibrational modes can be estimated from the temperature dependence of their frequency and linewidth [107]. If applied to the temperature dependent IR data of Engström *et al.* [114], it results in $\hbar\omega \approx 2$ meV for the O-Pt stretch vibration. This is comparable to CO/Pd(110) (see Tab. 7.1), and Engström *et*

al. mentioned in reference [94] that a relevant decay mechanism for the O-Pt stretch vibration is the excitation of a parallel adsorbate mode by anharmonic coupling which increases with temperature as has been shown in a theoretical work for O on Ni(111) [118].

The proposed mechanism suggests a stronger electronic coupling to the O-Pt stretch vibration than to the frustrated translation. Anisotropic electronic friction has been found, for example, for H₂ on Cu(111) and N₂ on Ru(0001) [119], which implies an initially strong adsorbate-substrate vibration perpendicular to the surface. For oxygen on a flat Pt(111) surface, however, the electronic friction calculated for the direction perpendicular to the surface is only 20% larger than for the lateral direction. On the other hand this difference does not need to be very large in order to result in a temperature-dependent coupling strength. In any case, the anharmonic coupling of the stretch vibration provides an additional pathway for the energy transfer, which becomes more efficient with increasing excitation density. Thus, this mechanism should be included in an accurate description of the energy transfer dynamics. The anisotropy of the friction may also be different for oxygen atoms at step sites due to their different coordination, which could enhance the importance of the anharmonic coupling in our case.

7.3 Perspectives

The discussion of electronically induced diffusion presented in the previous section is certainly speculative to some extent. It would be highly desirable to explore whether the proposed mechanism of indirect excitation of frustrated translations can be substantiated by a consistent theoretical description. One possibility to accomplish this would be to derive the electronic friction coefficient for O/Pt from *ab initio* calculations like Persson and co-workers have done this in the context of vibrational relaxation of adsorbates [119, 22, 115] and to combine these calculations with well established models for anharmonic coupling of vibrational modes [120, 31, 116, 121, 122, 117]. The model calculations presented in chapter 6 could easily be extended in order to make a direct comparison with experiment possible. In terms of a comparison with more sophisticated theoretical descriptions, such as a full DIMET calculation [57, 105], it should be emphasized that the temperature dependent friction coefficient $\eta_e(T_e)$ introduced in Sect. 6.4 provides a convenient interface between experiment and theory. A calculation of this coupling parameter allows for a comparison with experiment without theory having, e.g., to simulate a full cross-correlation measurement.

A second direction into which the present work should probably be extended con-

cerns the generality of the mechanism for electronically induced diffusion. A natural next choice for an adsorbate in this context is CO. CO is known to have a considerably higher binding energy at the steps of Pt(111) than on the terraces [61,29]. This makes it also possible to preferentially cover the step sites with CO molecules as described for O/Pt(111) system by adsorbing a well-defined amount of CO at temperature above 430 K and slowly cooling down the sample. Preliminary experiments conducted in our laboratory indicate that fs laser pulses are indeed able to induce diffusion for this system rather efficiently. The required pulse intensities are significantly lower than those necessary to induce the diffusion of atomic oxygen. Moreover, very recently Backus *et al.* [123] reported the results of time-resolved SFG vibrational spectroscopy for laser-induced diffusion of CO. Similar to our experiment, they used a stepped Pt(111) surface, Pt(553), in order to detect diffusion on a microscopic scale with a macroscopic optical probe. Their results suggests that in the case of CO diffusion the frustrated rotations rather than the frustrated translations are primarily driving the diffusive motion. Two-pulse correlation measurements would give information about the dynamics of energy transfer from the electronic excitation to adsorbate motion which are complementary to those obtained from time-resolved SFG. Since it is also easily possible to desorb CO under similar conditions, the comparison of two-pulse correlation experiments between diffusion and desorption would be most interesting. It could directly show whether the energy flow is similar or different for both reactions.

Finally, a third perspectives of the present work is to combine it with STM detection in order to gain more detailed microscopic information about electronically induced surface diffusion processes. A promising plan that will be pursued in our laboratory is to continue using SHG for detecting the average amount of step-depletion during the femtosecond excitation process. Then the sample is transferred in-situ to a scanning tunneling microscope and the distribution of adsorbates is determined with atomic resolution. Because one always starts with the same well-defined initial distribution where all adsorbates are located at the step edges one can investigate many more diffusion events by STM using such a scheme than with the method of Bartels *et al.* [34]. It should thus be possible to perform experiments for a variety of lasers parameters. In particular it should be possible to perform two-pulse-correlation measurements with the STM. This would enable us to perform the first experiment that combines ultrafast temporal with atomic-scale lateral resolution.

Summary

Electronically induced diffusion of atomic oxygen on a stepped Pt(111) surface has been studied using ultrashort pulses of near-infrared light for the generation of a hot electron distribution at the surface. This study represents the first time-resolved investigation of electronically induced diffusion at surfaces and demonstrates the possibility of initiating diffusion of a strongly chemisorbed adsorbate on a metal surface at low substrate temperatures by an electronic excitation.

The dissociative adsorption of molecular oxygen at steps on the Pt(111) surface has been used to generate a non-equilibrium distribution of an adsorbate by decorating the step edges selectively with chemisorbed atomic oxygen. The coverage at the step edges during adsorption and induced diffusion has been monitored by exploiting the sensitivity of optical second-harmonic generation (SHG) on surface symmetry which is macroscopically broken by regular steps. The high sensitivity of this method made it possible to measure rates for hopping from a step site onto an initially empty terrace site down to 10^{-7} per laser shot. A UHV chamber has been builded for the realization of the optical experiments as well as for the preparation and the characterization of the platinum surface.

The diffusion process has been studied as a function of laser fluence and time delay between two pump-pulses, which made it possible to investigate the energy transfer dynamics from the optical excitation to the frustrated translation. These experiments revealed a strong nonlinear dependence of the diffusion-rate on laser fluence ($\propto F^{15}$) and a fast electronic coupling of the initial excitation and the adsorbate motion with a time-constant of 1.5 ps. Both findings suggests that the excitation mechanism of diffusion on metal surfaces is the same as for the well-studied process of desorption induced by femtosecond laser excitation, which is driven by the hot laser-excited electrons of the metallic substrate. Even for complicated reaction pathways, such experiments can be successfully described by models in which the electronic coupling of the adsorbate to the metal surface is represented by a constant electronic friction coefficient. The extreme nonlinear dependence of the hopping-rate on laser fluence, however, indicates that the energy transfer mechanism is more complicated than for the case of desorption. This is reflected by the fact that a consistent description of the

experimental data within a generalized electronic friction model cannot be achieved with a constant electronic friction and a reasonable value for the diffusion barrier, but requires the introduction of a temperature dependent electronic friction coefficient.

It is suggested that this temperature dependence appears due to the neglect of the coupling between different vibrational modes. A mechanism of an indirect excitation by anharmonic coupling to the O-Pt stretch is proposed, that introduces a coupling which depends on excitation density and would therefore explain the observed effective dependence of the electronic friction on electron temperature.

Appendix A

Details of the Two-Temperature Model

After femtosecond laser excitation of metals the excited electron relaxation and the relevant redistribution of the energy of the optical excitation is governed by energy transport through non-equilibrium electrons, by electron-electron and electron-phonon scattering, and finally by diffusion of thermalized electrons. This appendix describes how the excited electrons can thermalize through electron-electron and electron-phonon scattering and how the optical excitation done by the laser can be calculated.

A.1 Thermalization of Hot Electrons

Optical excitation of the metal with fs-laser pulses creates a rectangular distribution of the electron-hole pairs, which is centered around the Fermi-level. The width of this non-Fermi distribution is given by twice the photon energy, and the height by the density of the adsorbed energy (see Fig. A.1, dashed line).

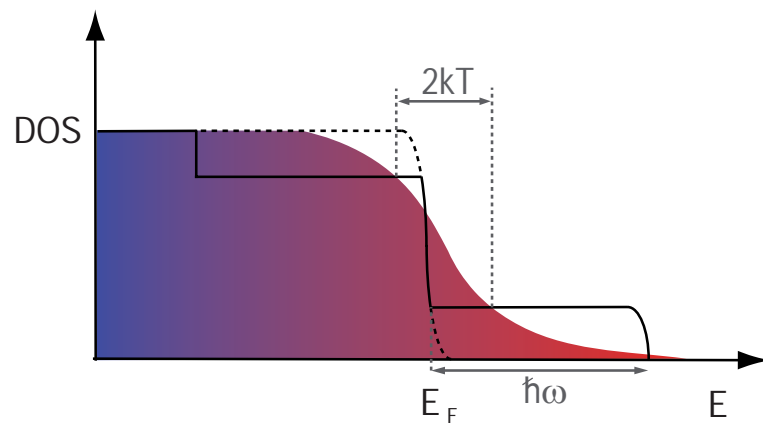


Fig. A.1: The electron distribution in the metal before the optical excitation (dashed line), after optical excitation by fs-laser pulses with photon energy $\hbar\omega$ (solid line), and the resulting Fermi-Distribution after thermalization (shaded).

Immediately after excitation, when the electrons are in a highly non-equilibrium state, two competing processes take place. One is ballistic motion of these excited electrons into deeper parts of the sample with velocities close to the Fermi velocity, i.e., approximately 10^6 m/s [124].

The other more general process is the development of an electron temperature by collisions between excited electrons and electrons around the Fermi level. Once thermal equilibrium among hot electrons is reached, a second time interval starts. This interval can be characterized by the Fermi distribution (Fig. A.1 shaded), and an electron temperature which differs strongly from the lattice temperature at the beginning. Such a hot electron bath is initially localized within the optical absorption depth for d-band metals. Driven by the temperature gradient, these hot electrons diffuse into deeper parts of the bulk with a considerably slower speed than ballistic motion. The diffusion length is governed by electron-phonon coupling which cools the electron bath [98] and it can be well-described in the two-temperature model.

For the transition metal ruthenium, Lisowski *et al.* [125] studied the dynamics of electron thermalization, cooling and transport effects. They could show that apart from the known inability of the two-temperature model to describe the initial carrier dynamics due to their non-thermal character, it yields an energy density (electronic temperature) at the surface which is systematically too high for times >400 fs after excitation. With the additional insertion of a ballistic transport mechanism their simulations agreed with experimental data. Therefore, they proposed that ballistic transport will be important at times where usually the two-temperature model is used to describe carrier dynamics because it can lead to very efficient energy transfer into the bulk.

A.2 Electron-Phonon Scattering

The hot electrons can lose energy not only through electron-electron scattering, but through electron-phonon scattering. Deformation of a crystal lattice modifies also the electronic structure of the crystal, i.e. in the free electron gas model it leads to a periodic charge aggregation through a longitudinal lattice oscillation of the ion cores, which will be screened with the same electron spatial distribution. Consideration of such time dependent potential changes in the Hamiltonian of the system leads to an inelastic coupling between the electrons and the lattice oscillations, the so-called electron-phonon coupling ($g(T_e - T_i)$ in Eq. 6.1).

Using first-order perturbation theory in the Born-Oppenheimer approximation, where the perturbation of the lattice is assumed to be quasi-static with respect to the

electronic motion, the total Hamiltonian can be written as:

$$\hat{H} = \sum_i \frac{p_i^2}{2m} + \sum_{i,\alpha} V(\mathbf{r}_i - \mathbf{R}_\alpha) + \hat{\mathbf{H}}_{ee} + \hat{\mathbf{H}}_{\text{ion-ion}}. \quad (\text{A.1})$$

It includes the kinetic energy of the electrons, the potential energy for electrons at coordinate \mathbf{r}_i and ions at \mathbf{R}_α , the electron-electron interaction, and the ion-ion interaction.

For calculating the electron-phonon interaction from Eq. A.1, it is generally assumed, that the form of the deformation potential does not change, when the ions are slightly displaced by $\delta\mathbf{R}_\alpha$ from their equilibrium position, and it can be included in the second term of the Hamiltonian [126].

In perturbation theory (Fermi's golden rule), the probability of a transition of an electron from state $|1\rangle$, into state $|2\rangle$ by emission or absorption of one photon is given by:

$$P_{12} = \frac{2\pi}{\hbar} |\langle 2|\hat{g}|2\rangle|^2 \delta(E_2 - E_1). \quad (\text{A.2})$$

The energy transfer rate g has been calculated by Kaganov *et al.* [127], it is a sum over all elementary one-phonon absorption and emission processes, weighted with the energy transfer (\pm phonon energy) per collision. The electrons and phonons have Fermi-Dirac and Bose-Einstein distribution, respectively. The acoustic phonon spectrum is described with the Debye model. The total transfer of energy per unit volume and per second from electrons to phonons is:

$$g(T_e, T_i) = f(T_e) - f(T_i) \quad (\text{A.3})$$

where

$$f(T) = 4g_\infty \left(\frac{T}{\Theta_D}\right)^5 \int_0^{\frac{\Theta_D}{T}} \frac{x^4}{e^x - 1} dx. \quad (\text{A.4})$$

In the literature of the fs spectroscopy g_∞ is called the electron-phonon coupling constant [128].

A.3 Optical Excitation and Penetration Depth

For calculating the temporal evolution of the temperature of the electrons and phonons from the two-temperature model, we need to know the optical excitation which is described by the source term. Absorption of incident laser pulses at metal surfaces can be described with electron-hole excitation. The absorbed energy is distributed among the excited electrons at the surface, where the spatial distribution function can be characterized with the optical penetration depth, or "skin-depth" δ .

Material constants	Symbol	Value	[Units]
Electron-phonon coupling	g	6.76	10^{17} W/m ³ K
Electron heat capacity	γ	748	J/m ³ K ²
Heat conductivity (0 K)	κ	71.6	W/mK
Debye temperature	Θ_D	240	K
Density of atoms	n	21450	kg/m ³
Atomic mass	μ	195.08	g/mol
Penetration depth	δ	12.55	10^{-9} m
Refractivity index (800nm)	n	2.92	
Wave number (800nm)	k	5.07	

Tab. A.1: The relevant material constants of Platinum [82, 103]

In term of the classical electrodynamics, deducing from the Maxwell's equation, the simplest solution of the a plane, time-harmonic wave in metals is:

$$\vec{E} = \vec{E}_0 e^{i(\hat{k}\vec{x} - \omega t)} \quad (\text{A.5})$$

with a complex refractive index

$$\hat{n} = n(1 + i\kappa) = \frac{c}{\omega} \hat{k}. \quad (\text{A.6})$$

Here n and κ are real, \hat{k} is the complex wave number and κ is the extinction coefficient. Taken \hat{k} from Eq. A.6 into Eq. A.5 we get

$$\vec{E} = \vec{E}_0 e^{-\frac{\omega}{c} n \kappa \vec{x}} e^{i\omega[\frac{n}{c}\vec{x} - t]}. \quad (\text{A.7})$$

The real part of the Eq. A.7 represents the electric field vector, which is a plane wave with wavelength $\lambda = 2\pi c/\omega n$. The extinction is given by the first exponential term. The intensity of the incident light is exponentially damping in the metal along axis x , and it is proportional to \vec{E}^2 :

$$I \propto |E|^2 \propto e^{2\frac{\omega}{c} n \kappa \vec{x}} = e^{\frac{4\pi}{\lambda_0} n \kappa \vec{x}} = e^{\frac{4\pi}{\lambda} \kappa \vec{x}}. \quad (\text{A.8})$$

λ_0 is the wavelength in vacuum, and λ is the wavelength in the medium. The distance which makes the energy density fall to 1/e of its value is the penetration depth or skin-depth [129]:

$$\delta = \frac{\lambda_0}{4\pi n \kappa} = \frac{\lambda}{4\pi \kappa} \quad (\text{A.9})$$

With the help of the complex refractive index we can calculate the transmitted and reflected part of the incident light, applying the Fresnel-equations for the interface

between two materials for a given polarization (s or p) and for a given angle of incidence.

The excitation of the laser pulses in the two-temperature model decays like:

$$S(x, t) = \frac{(1 - R)I(t)}{\delta} e^{-x/\delta}. \quad (\text{A.10})$$

This is the so-called source term, which describes the absorbed energy density, determined by the optical penetration depth δ and the absorbed fraction of the incident intensity [104].

Bibliography

- [1] D. Menzel and R. Gomer, *J. Chem. Phys.* **41**, 3311 (1964).
- [2] P. A. Redhead, *Can. J. Phys.* **42**, 886 (1964).
- [3] J. A. Prybyla, T. F. Heinz, J. A. Misewich, M. M. T. Loy, and J. H. Glowonia, *Phys. Rev. Lett.* **64**, 1537 (1990).
- [4] F. Budde, T. F. Heinz, M. M. T. Loy, J. A. Misewich, F. Derougemont, and H. Zacharias, *Phys. Rev. Lett.* **66**, 3024 (1991).
- [5] J. A. Prybyla, H. W. K. Tom, and G. D. Aumiller, *Phys. Rev. Lett.* **68**, 503 (1992).
- [6] F. J. Kao, D. G. Busch, D. Cohen, D. G. Dacosta, and W. Ho, *Phys. Rev. Lett.* **71**, 2094 (1993).
- [7] J. A. Misewich, A. Kalamarides, T. F. Heinz, U. Höfer, and M. M. T. Loy, *J. Chem. Phys.* **100**, 736 (1994).
- [8] S. Deliwala, R. J. Finlay, J. R. Goldman, T. H. Her, W. D. Mieher, and E. Mazur, *Chem. Phys. Lett.* **242**, 617 (1995).
- [9] D. G. Busch and W. Ho, *Phys. Rev. Lett.* **77**, 1338 (1996).
- [10] L. M. Struck, L. J. Richter, S. A. Buntin, R. R. Cavanagh, and J. C. Stephenson, *Phys. Rev. Lett.* **77**, 4576 (1996).
- [11] R. J. Finlay, T. H. Her, C. Wu, and E. Mazur, *Chem. Phys. Lett.* **274**, 499 (1997).
- [12] T. H. Her, R. J. Finlay, C. Wu, and E. Mazur, *J. Chem. Phys.* **108**, 8595 (1998).
- [13] M. Bonn, S. Funk, C. Hess, D. N. Denzler, C. Stampfl, M. Scheffler, M. Wolf, and G. Ertl, *Science* **285**, 1042 (1999).

- [14] G. Eichhorn, M. Richter, K. Al-Shamery, and H. Zacharias, *J. Chem. Phys.* **111**, 386 (1999).
- [15] L. Cai, X. D. Xiao, and M. M. T. Loy, *Surf. Sci.* **464**, L727 (2000).
- [16] D. P. Quinn and T. F. Heinz, *J. Vac. Sci. Technol. A* **21**, 1312 (2003).
- [17] D. N. Denzler, C. Frischkorn, C. Hess, M. Wolf, and G. Ertl, *Phys. Rev. Lett.* **91**, 226102 (2003).
- [18] X.-L. Zhou, X.-Y. Zhu, and J. M. White, *Surf. Sci. Rep.* **13**, 73 (1991).
- [19] P. Feulner and D. Menzel, in *Laser Spectroscopy and Photochemistry on Metal Surfaces*, edited by H. L. Dai and W. Ho (World Scientific, Singapore, 1995), p. 627.
- [20] E. Hasselbrink, *Chem. Phys. Lett.* **170**, 329 (1990).
- [21] D. M. Newns, T. F. Heinz, and J. A. Misewich, *Progress in Theoretical Physics Supplement* **106**, 411 (1991).
- [22] M. Head-Gordon and J. C. Tully, *J. Chem. Phys.* **103**, 10137 (1995).
- [23] M. Brandbyge, P. Hedegård, T. F. Heinz, J. A. Misewich, and D. M. Newns, *Phys. Rev. B* **52**, 6042 (1995).
- [24] C. Springer and M. Head-Gordon, *Chem. Phys.* **205**, 73 (1996).
- [25] K. P. Bohnen, M. Kiwi, and H. Suhl, *Phys. Rev. Lett.* **34**, 1512 (1975).
- [26] A. Nourtier, *Journal De Physique* **38**, 479 (1977).
- [27] A. G. Fedorus, E. V. Klimenko, A. G. Naumovets, E. M. Zasimovich, and I. N. Zasimovich, *Nucl. Instrum. Methods Phys. Res. Sect. B-Beam Interact. Mater. Atoms* **101**, 207 (1995).
- [28] T. E. Madey, F. P. Netzer, J. E. Houston, D. M. Hanson, and R. Stockbauer, in *Desorption Induced by Electronic Transitions, DIET-1*, Vol. 24 of *Springer Series in Chemical Physics*, edited by N. H. Tolk (Springer, Heidelberg, 1983), p. 120.
- [29] H. J. Jänsch, J. Z. Xu, and J. T. Yates, *J. Chem. Phys.* **99**, 721 (1993).
- [30] W. Ho, *J. Chem. Phys.* **117**, 11033 (2002).

- [31] T. Komeda, Y. Kim, M. Kawai, B. N. J. Persson, and H. Ueba, *Science* **295**, 2055 (2002).
- [32] K. Morgenstern and K. H. Rieder, *J. Chem. Phys.* **116**, 5746 (2002).
- [33] J. I. Pascual, N. Lorente, Z. Song, H. Conrad, and H. P. Rust, *Nature* **423**, 525 (2003).
- [34] L. Bartels, F. Wang, D. Moller, E. Knoesel, and T. F. Heinz, *Science* **305**, 648 (2004).
- [35] M. B. Raschke and U. Höfer, *Phys. Rev. B* **59**, 2783 (1999).
- [36] Y. R. Shen, *Annu. Rev. Phys. Chem.* **40**, 327 (1989).
- [37] G. A. Reider and T. F. Heinz, in *Photonic Probes of Surfaces*, edited by P. Halevi (North-Holland, Amsterdam, 1995), pp. 3–66.
- [38] *Nonlinear Optics in Metals, International series of monographs on physics*, edited by K.-H. Bennemann (Oxford University Press, Oxford, 1998).
- [39] *Special Issue: Nonlinear Optics at Interfaces (NOPTI)*, edited by J. Hohlfeld and T. Rasing (Springer-Verlag, Online, 2002), Vol. 74, p. 615.
- [40] G. Lüpke, D. J. Bottomley, and H. M. Vandriel, *J. Opt. Soc. Am. B-Opt. Phys.* **11**, 33 (1994).
- [41] P. Kratzer, E. Pehlke, M. Scheffler, M. B. Raschke, and U. Höfer, *Phys. Rev. Lett.* **81**, 5596 (1998).
- [42] K. Stépán, J. Güdde, and U. Höfer, *PRL* **94**, 236103 (2005).
- [43] H. Nienhaus, *Surf. Sci. Rep.* **45**, 1 (2002).
- [44] J. C. Tully, *J. Chem. Phys.* **93**, 1061 (1990).
- [45] J. W. Gadzuk, in *Laser Spectroscopy and Photo-Chemistry on Metal Surfaces Part II*, edited by H. L. Dai and W. Ho (World Scientific, Singapore, 1996), pp. 897–942.
- [46] J. A. Misewich, T. F. Heinz, and D. M. Newns, *Phys. Rev. Lett.* **68**, 3737 (1992).
- [47] J. W. Gadzuk, *Surf. Sci.* **342**, 345 (1995).

- [48] A. Fhlisch, P. Feulner, F. Hennies, A. Fink, D. Menzel, D. Sanchez-Portal, P. M. Echenique, and W. Wurth, *Nature* **436**, 373 (2005).
- [49] W. S. Fann, R. Storz, H. W. K. Tom, and J. Bokor, *Phys. Rev. Lett.* **68**, 2834 (1992).
- [50] W. S. Fann, R. Storz, H. W. K. Tom, and J. Bokor, *Phys. Rev. B* **46**, 13592 (1992).
- [51] C. Lei, M. Bauer, K. Read, R. Tobey, Y. Liu, T. Popmintchev, M. M. Murnane, and H. C. Kapteyn, *Phys. Rev. B* **66**, 245420 (2002).
- [52] H. Petek, H. Nagano, M. J. Weida, and S. Ogawa, *J. Phys. Chem. B* **105**, 6767 (2001).
- [53] M. Bauer, S. Pawlik, R. Burgermeister, and M. Aeschlimann, *Surf. Sci.* **404**, 62 (1998).
- [54] S. Ogawa, H. Nagano, and H. Petek, *Phys. Rev. Lett.* **82**, 1931 (1999).
- [55] M. Wolf, A. Hotzel, E. Knoesel, and D. Velic, *Phys. Rev. B* **59**, 5926 (1999).
- [56] F. J. Kao, D. G. Busch, D. G. Dacosta, and W. Ho, *Phys. Rev. Lett.* **70**, 4098 (1993).
- [57] J. A. Misewich, S. Nakabayashi, P. Weigand, M. Wolf, and T. F. Heinz, *Surf. Sci.* **363**, 204 (1996).
- [58] H. Löser, D. Fick, and H. J. Jänsch, *J. Phys. Chem. B* **108**, 14440 (2004).
- [59] R. Gomer, *Rep. Prog. Phys.* **53**, 917 (1990).
- [60] T. Zambelli, J. Trost, J. Wintterlin, and G. Ertl, *Phys. Rev. Lett.* **76**, 795 (1996).
- [61] J. E. Reutt-Robey, D. J. Doren, Y. J. Chabal, and S. B. Christman, *J. Chem. Phys.* **93**, 9113 (1990).
- [62] S. Janz, D. J. Bottomley, H. M. van Driel, and R. S. Timsit, *Phys. Rev. Lett.* **66**, 1201 (1991).
- [63] J. E. Sipe, D. J. Moss, and H. M. Vandriel, *Phys. Rev. B* **35**, 1129 (1987).
- [64] R. W. Boyd, *Nonlinear Optics*, 1 ed. (Academic Press, Boston, 1992).

- [65] T. F. Heinz, in *Nonlinear Surface Electromagnetic Phenomena*, edited by H.-E. Ponath and G. I. Stegeman (Elsevier, Amsterdam, 1991).
- [66] T. F. Heinz, Dissertation, University of California, Berkeley, CA, 1981.
- [67] H. W. Tom and G. D. Aumiller, *Phys. Rev. B* **33**, 8818 (1986).
- [68] H. Wang, R. G. Tobin, D. K. Lambert, C. L. DiMaggio, and G. B. Fisher, *Surf. Sci.* **372**, 267 (1997).
- [69] A. T. Gee and B. E. Hayden, *J. Chem. Phys.* **113**, 10333 (2000).
- [70] A. C. Luntz, M. D. Williams, and D. S. Bethune, *J. Chem. Phys.* **89**, 4381 (1988).
- [71] P. J. Feibelman, S. Esch, and T. Michely, *Phys. Rev. Lett.* **77**, 2257 (1996).
- [72] A. Bogicevic, J. Strömquist, and B. I. Lundqvist, *Phys. Rev. B* **57**, R4289 (1998).
- [73] Ž. Šljivančanin and B. Hammer, *Surf. Sci.* **515**, 235 (2002).
- [74] H. Steininger, S. Lehwald, and H. Ibach, *Surf. Sci.* **123**, 1 (1982).
- [75] J. L. Gland, B. A. Sexton, and G. B. Fisher, *Surf. Sci.* **95**, 587 (1980).
- [76] A. Winkler, X. Guo, H. R. Siddiqui, P. L. Hagans, and J. T. Yates, *Surf. Sci.* **201**, 419 (1988).
- [77] P. Gambardella, Ž. Šljivančanin, B. Hammer, M. Blanc, K. Kuhnke, and K. Kern, *Phys. Rev. Lett.* **87**, 056103 (2001).
- [78] P. J. Feibelman, *Phys. Rev. B* **52**, 16845 (1995).
- [79] P. Feulner and D. Menzel, *JVST* **17**, 662 (1980).
- [80] H. Schlichting and D. Menzel, *Surf. Sci.* **285**, 209 (1993).
- [81] X. Y. Zhu, S. R. Hatch, A. Champion, and J. M. White, *J. Chem. Phys.* **91**, 5011 (1989).
- [82] *Handbook of Optical Constants of Solids*, edited by E. D. Palik (Academic Press, San Diego, 1998).
- [83] H. W. K. Tom, T. F. Heinz, and Y. R. Shen, *Phys. Rev. Lett.* **51**, 1983 (1983).

- [84] U. Höfer, *Appl. Phys. A* **63**, 533 (1996).
- [85] R. K. Chang, J. Ducuing, and N. Bloembergen, *Phys. Rev. Lett.* **15**, 6 (1965).
- [86] K. J. Veenstra, A. V. Petukhov, A. P. de Boer, and T. Rasing, *Phys. Rev. B* **58**, R16020 (1998).
- [87] P. T. Wilson, Y. Jiang, O. A. Aktsipetrov, E. D. Mishina, and M. C. Downer, *Opt. Lett.* **24**, 496 (1999).
- [88] C. T. Campbell, G. Ertl, H. Kuipers, and J. Segner, *Surf. Sci.* **107**, 220 (1981).
- [89] D. H. Parker, M. E. Bartram, and B. E. Koel, *Surf. Sci.* **217**, 489 (1989).
- [90] B. Hammer, *Surf. Sci.* **459**, 323 (2000).
- [91] R. Lewis and R. Gomer, *Surf. Sci.* **12**, 157 (1968).
- [92] J. Wintterlin, R. Schuster, and G. Ertl, *Phys. Rev. Lett.* **77**, 123 (1996).
- [93] B. C. Stipe, M. A. Rezaei, W. Ho, S. Gao, M. Persson, and B. I. Lundqvist, *Phys. Rev. Lett.* **78**, 4410 (1997).
- [94] U. Engström and R. Ryberg, *J. Chem. Phys.* **112**, 1959 (2000).
- [95] M. B. Raschke, Dissertation, Technische Universität München, 1999.
- [96] W. S. Fann, R. Storz, H. W. K. Tom, and J. Bokor, *Phys. Rev. Lett.* **68**, 2834 (1992).
- [97] W. S. Fann, R. Storz, H. W. K. Tom, and J. Bokor, *Phys. Rev. B* **46**, 13592 (1992).
- [98] J. Hohlfeld, S. S. Wellershoff, J. Güdde, U. Conrad, V. Jahnke, and E. Matthias, *Chem. Phys.* **251**, 237 (2000).
- [99] M. Bonn, D. N. Denzler, S. Funk, M. Wolf, S. S. Wellershoff, and J. Hohlfeld, *Phys. Rev. B* **61**, 1101 (2000).
- [100] S. S. Wellershoff, J. Hohlfeld, J. Güdde, and E. Matthias, *Appl. Phys. A-Mater. Sci. Process.* **69**, S99 (1999).
- [101] S. I. Anisimov, B. L. Kapeliovich, and T. L. Perel'man, *Sov. Phys. JETP* **39**, 375 (1974).

- [102] N. W. Ashcroft and N. D. Mermin, *Solid State Physics* (Holt, Rinehart and Winston, New York, 1976).
- [103] C. Kittel, *Introduction to Solid State Physics*, 7. ed. (John Wiley, New York, 1996).
- [104] D. N. Denzler, Dissertation, Freien Universität Berlin, 2003.
- [105] H. Guo, P. Saalfrank, and T. Seideman, *Prog. Surf. Sci.* **62**, 239 (1999).
- [106] B. N. J. Persson and M. Persson, *Solid State Commun.* **36**, 175 (1980).
- [107] B. N. J. Persson and R. Ryberg, *Phys. Rev. Lett.* **54**, 2119 (1985).
- [108] F. Budde, T. F. Heinz, A. Kalamarides, M. M. T. Loy, and J. A. Misewich, *Surf. Sci.* **283**, 143 (1993).
- [109] J. A. Misewich, T. F. Heinz, P. Weigand, and A. Kalamarides, in *Laser Spectroscopy and Photo-Chemistry on Metal Surfaces Part II*, edited by H. L. Dai and W. Ho (World Scientific, Singapore, 1996), pp. 764–826.
- [110] J. Wintterlin, R. Schuster, and G. Ertl, *Phys. Rev. Lett.* **77**, 123 (1996).
- [111] K. Stépán, M. Dürr, J. Güdde, and U. Höfer, *Surf. Sci.* **593**, 54 (2005).
- [112] D. N. Denzler, C. Frischkorn, M. Wolf, and G. Ertl, *J. Phys. Chem. B* **108**, 14503 (2004).
- [113] C. Puglia, A. Nilsson, B. Hernnas, O. Karis, P. Bennich, and N. Martensson, *Surf. Sci.* **342**, 119 (1995).
- [114] U. Engström and R. Ryberg, *Phys. Rev. Lett.* **82**, 2741 (1999).
- [115] J. C. Tully, M. Gomez, and M. Head-Gordon, *J. Vac. Sci. Technol. A-Vac. Surf. Films* **11**, 1914 (1993).
- [116] B. N. J. Persson and H. Ueba, *Surf. Sci.* **502**, 18 (2002).
- [117] H. Ueba, T. Mii, N. Lorente, and B. N. J. Persson, *J. Chem. Phys.* **123**, 084707 (2005).
- [118] J. C. Ariyasu and D. L. Mills, *Phys. Rev. B* **30**, 507 (1984).
- [119] A. C. Luntz and M. Persson, *J. Chem. Phys.* **123**, 074704 (2005).

- [120] P. Jakob and B. N. J. Persson, Phys. Rev. B **56**, 10644 (1997).
- [121] H. Ueba and B. N. J. Persson, Surf. Sci. **566-568**, 1 (2004).
- [122] H. Ueba, Appl. Surf. Sci. **237**, 565 (2004).
- [123] E. H. G. Backus, A. Eichler, A. W. Kleyn, and M. Bonn, Science **310**, 1790 (2005).
- [124] B. J. Brorson, J. G. Fujimoto, and E. P. Ippen, Phys. Rev. Lett. **59**, 1962 (1987).
- [125] M. Lisowski, P. A. Loukakos, U. Bovensiepen, J. Stähler, C. Gahl, and M. Wolf, Appl. Phys. A-Mater. Sci. Process. **78**, 165 (2004).
- [126] J. Hohlfeld, Dissertation, Freie Universität Berlin, 1998.
- [127] M. I. Kaganov, I. M. Lifshitz, and L. V. Tanatarov, Sov. Phys. JETP **4**, 173 (1957).
- [128] R. H. M. Groeneveld, R. Sprik, and A. Lagendijk, Phys. Rev. B **51**, 11433 (1995).
- [129] *Principles of Optics*, edited by M. Born and E. Wolf (Cambridge University Press, Cambridge, 1999).

List of Publications

Krisztina Stépán, Jens Gudde, and Ulrich Hofer

Time-resolved measurement of diffusion induced by femtosecond laser pulses

Phys. Rev. Lett. **94** 236103 (2005)

Krisztina Stépán, Michael Durr, Jens Gudde, and Ulrich Hofer

Electronically induced diffusion of oxygen on a stepped Pt(111) surface

Surf. Sci. **593** 54-66 (2005)

Kordás K., Nánai L., Bali K., Stépán K., Vajtai R., George T.F., Leppavuori S.

Palladium thin film deposition from liquid precursors on polymers by projected excimer beams.

Appl. Surf. Sci., **168(1-4)**, 67-71 (2000)

Contributions to International Conferences and Workshops

K. Stépán, J. Gudde und U. Hofer

Time-resolved study of femtosecond-laser induced diffusion of O on stepped Pt(111)

Ultrafast dynamics of collective excitation in solids

(2005 September, Vitte, Hiddensee Islands, Germany)

K. Stépán, J. Gudde und U. Hofer

Laser induced electronical diffusion of O/Pt(111)

European Graduate College Seminar "Electron-Electron Interactions in Solids"

(2005 September, Riezlern, Austria)

K. Stépán, J. Gudde und U. Hofer

Time-resolved measurement of femtosecond laser induced diffusion of O on Pt(111)

Ph.D. Student Workshop "Dynamics of Electron Transfer Processes at Interfaces/SPP 1093"

(2004 September, Juist, Germany)

K. Stépán, J. Güdde und U. Höfer

Femtosecond-laser Induced Diffusion of O on Pt(111) Surface

European Graduate College Seminar "Electron-Electron Interactions in Solids"

(2004 September, Ráckeve, Hungary)

K. Stépán, J. Güdde und U. Höfer

Two-pulse correlation of femtosecond laser-induced diffusion of oxygen on Pt(111)

DPG-Spring Meeting of the Division Condensed Matter Physics

(2004 March, Regensburg, Germany)

K. Stépán, J. Güdde und U. Höfer

Electronical Induced Diffusion by fs laser pulses

European Graduate College Seminar "Electron-Electron Interactions in Solids"

(2003 September, Riezlern, Austria)

K. Stépán, J. Güdde und U. Höfer

Electronical Induced Diffusion

European Graduate College Seminar "Electron-Electron Interactions in Solids"

(2002 September, Ráckeve, Hungary)

Curriculum Vitae

- 21.10.1974 Born in Miskolc, Hungary
- 1989-93 Gárdonyi Géza Gymnasium Eger, Hungary
- 1994-2001 József Attila University (JATE) Szeged, Hungary
2001 Diploma in Physics, Diplom thesis: "Nuclear reactor accidents and their enviromental effects"
2003 Diploma in Chemistry, Diplom thesis: "Surface plasmon resonance spectroscopy of self assembly monolayers"
- 03-08.2001 Erasmus Scholarship, Experimental Semiconductor Group, Philipps Universität Marburg, Germany
- Since 09.01 PhD study, Surface Dynamics Group, Philipps-Universität Marburg, Germany
- 05.02-04.05 Scholarship of the International Research Training Group 790 Philipps-Universität Marburg, Germany
- 09.02-09.03 Student representative in the International Research Training Group 790 - Electron-Electron Interactions in Solids (Marburg-Budapest)
- 05.05-04.06 Scholarship of the German-Israeli Foundation (GIF)

Acknowledgments

Herewith I would like to render thanks to all the people who made it possible to come this thesis into being.

First of all, I would like to thank my PhD supervisor Prof. Dr. Ulrich Höfer, who has given me the possibility to become a member of his excellent group and who has offered this fascinating topic for my thesis.

There is a big thank towards Prof. Dr. Peter Thomas who is not only the second referee of my work but who has talked me into doing my PhD study in Germany and who has helped me during these years as a friend.

I thank Dr. habil Wolfgang Stolz and Prof. Dr. Karl-Michael Weitzel for their interest in the present work.

I owe a special thanks for my tutor Dr. Jens Güdde who was more than patient with me as he supervised me during my everyday work, as he taught me to handle the laser-systems and the vacuum apparatuses, as he helped me to understand many aspects of physics better and as he proofread my thesis. And here I would also like to thank for the tolerance of his family (Antonia, Vincent, Clara, Niki and Elinor) who had to miss him for several long measuring evenings.

I am thankful to the PhD students Marco Lawrenz, Marcus Rohleder, Chris Schwalb, and Matthias Koch and the ex-colleagues Dr. Catrinel Stanciu, Dr. Eckhard Finger, Joost Gielis, and Dr. Erwin Kessels for the various help they supplied to me and also for the non-scientific activities that we did together (trying to teach me to play "Doppelkopf", memorable hiking in the Alps and in the Pfalz, and so on).

I am grateful to Manfred Preis for helping me to fix every mechanical problem with my chamber and motivating me to learn German.

Continuous support by the workshops (especially from Dr. Matthias Born and Carsten Schindler) is greatly acknowledged.

Financial support from the International Research Training Group 790 "Electron-Electron Interactions in Solids" and the German-Israeli Foundation (GIF) is acknowledged here as well as their support to participate in workshops and conferences and broaden my knowledge.

A special thanks goes to my ex-supervisors and friends Dr. Katalin Bali and Dr. László Nánai from Hungary, who believed in my knowledge and encouraged me

to make this study.

Last, but most of all I would like to thank Kai Schubert who not only supported me all these years and helped me arrange all the formalities in bureaus (which was of great help since the lack of German language) but helped me with his knowledge in technical and physical questions.